UCLouvain

epl

École polytechnique de Louvain

Quantifying brain anomalies in children with bilateral lesions leading to cerebral palsy via diffusion Magnetic Resonance Imaging

Author: **Ysaline LEMAN**
Supervisors: **Laurence DRICOT, Benoit MACQ**
Readers: **Rodrigo ARANEDA, Ron KUPERS, Gaëtan RENSONNET**
Academic year 2019–2020
Master [120] in Biomedical Engineering

Abstract

Context Cerebral Palsy (CP) is caused by non-progressive disturbances of the brain that arise during fetal or infant development [1]. The lesions created by these disturbances modify the cerebral structure, including major fiber tracts of the white matter. To predict CP with certainty based on conventional structural Magnetic Resonance Imaging (MRI) is difficult. Moreover, the extent to which the integrity of the fiber tracts is restorable with motor training is unknown [2]. This is the reason why some other techniques were investigated to improve diagnoses and therapies.

Objective Diffusion Weighted Imaging (DWI) is sensitive to water molecule diffusion. Applying adequate mathematical models to DWI allows the microstructural analysis of white matter tracts. This thesis investigates these models to measure and to quantify the damages caused by bilateral lesions on the Corticospinal Tract (CST), the most important tract for fine motor skill [3].

Experiment This work is composed of two parts: the CST extraction and the quantification of the brain modifications due to CP. To extract the CST was a major challenge of this thesis: due to the small brain size of the subjects and completely changed brain structure of children with CP, the reference atlas cannot be used to isolate the CST. By consequence, this thesis evaluated the efficiency of the tracking method for CST extraction. The second step of this work was to quantify the CST modifications due to CP, by analysing the metrics of the microstructural models: Diffusion Tensor Imaging (DTI) and Neurite Orientation and Dispersion Density Imaging (NODDI).

Results The statistical analysis showed that the diffusion metrics (Mean Diffusivity (MD) and Radial Diffusivity (RD)) reflect an increased freedom of diffusion in the white matter and may reflect a degree of demyelination in children with CP. Moreover, an increase of Fractional Anisotropy (FA) highlights the lower fiber density in these children. This result was confirmed by the ICVF metric.

Conclusion The microstructure models based on DWI provide relevant metrics to measure and quantify the modification of brain structure in children with bilateral lesions.

Acknowledgements

This master thesis is the result of numerous hours of personal work but also moments of collaboration. This work would have been impossible without others helping me to carry out this work. This is why i would like to begin with the expression of my gratitude for the support and the help I received.

First of all, I would like to thank my mother, my family and my friends that supported me not only for this work but throughout all my studies.

In particular, I would like to thank my two direct supervisors: Prof. Benoit Macq who has allowed me to work on this fascinating subject and has monitored my work during this year; Laurence Dricot for her thorough supervision, trust and encouragements.

Beside my supervisors, I would like to acknowledge Rodrigo Araneda for his useful advice, knowledge and thoughtfulness. I also would like to thank Gaëtan Ronsonnet for his insightful comments and his time.

Finally, I acknowledge Prof. Alexander Leemans for his technical support, which helped me several times using his program ExploreDTI.

Contents

List of Figures

List of Tables

List of Abbreviations

AD	Axial Diffusivity.
ADC	Apparent Diffusion Coefficient.
AKC	Apparent Kurtosis Coefficient.
BV	BrainVoyager.
CP	Cerebral Palsy.
CSD	Constrained Spherical Deconvolution.
CSF	Cerebrospinal Fluid.
CST	Corticospinal Tract.
D	Dominant.
DIAMOND	DIstribution of Anisotropic MicrOstructural eNvironments with DTI.
DKI	Diffusion Kurtosis Imaging.
DKT	Diffusion Kurtosis Tensors.
DQ	Developmental Quotient.
DTI	Diffusion Tensor Imaging.
DW	Diffusion Weighted.
DWI	Diffusion Weighted Imaging.
FA	Fractional Anisotropy.
FD	Free Water Diffusivity.
fMRI	functional Magnetic Resonance Imaging.
Frac(Pi)	Fraction of Population i.
GMI	Gray Mater Injury.
HC	Healthy Control subject.

Hei	Heterogeneity.
HIE	Hypoxic-Ischemic Encephalopathy.
ICVF	Intracellular Volume Fraction.
ISOVF	Isotropic Volume Fraction.
M	Magnetization.
MD	Mean Diffusivity.
MR	Magnetic Resonance.
MRI	Magnetic Resonance Imaging.
ND	Non-Dominant.
NODDI	Neurite Orientation and Dispersion Density Imaging.
ODI	Orientation Dispersion Index.
PEDI-CAT	Pediatric Evaluation of Disability Inventory-Computer AdaptiveTest.
PGSE	Pulsed-Gradient Spin Echo.
PLIC	Posterior Limb of the Internal Capsule.
PVL	Periventricular Lesion.
QIT	Quantitative Imaging Toolkit.
RD	Radial Diffusivity.
RF	RadioFrequency.
ROI	Region Of Interest.
SD	Standard Deviation.
SMS	Simultaneous Multi-Slices.
TE	Echo Time.
TMS	Transcranial Magnetic Stimulation.
wFA	weighted Fractional Anisotropy.
WMI	White Mater Injury.

Introduction

Cerebral Palsy (CP) is caused by non-progressive disturbances of the brain that arise during fetal or infant development [1]. The lesion created by these disturbances modifies the cerebral structure, including major fiber tracts of the white matter. The aim of this thesis is to gain insights into these modifications.

Recent research has shown that early intervention in infants at risk of CP leads to improved motor outcomes [5]. Moreover, in children with CP, intensive motor skill training can improve the integrity of the Corticospinal Tract (CST), the most important tract for fine motor skills [3]. This improvement is correlated with higher motor performance [2]. However, it is difficult to predict CP with certainty based on conventional structural Magnetic Resonance Imaging (MRI). This leads to a lack of early treatments for children who could benefit of it and to an unnecessary general early intervention service for children who have normal motor outcome [5]. Moreover, it is unknown to which extent the integrity of the CST fibers emerging from the lesioned hemisphere is restorable with training [2].

Diagnoses and therapies could be improved through a better understanding of the CST structural changes in children with CP.

To investigate the brain structure the Diffusion Weighted Imaging (DWI) technique is used in this thesis. DWI is sensitive to water molecule diffusion and by combining this technique with adequate mathematical models, it allows microstructural analysis of white matter tissues.
The simplest mathematical model is Diffusion Tensor Imaging (DTI) which converts the DWI signal to morphological characteristics of the axons and glial cells of the white matter. Unfortunately, the metrics variation of this model can be associated to different causes, leading to a lack of biological interpretation.
This is the reason why more complex models need to be investigated, such as Neurite Orientation and Dispersion Density Imaging (NODDI). This model estimates more physically interpretable microstructural parameters.

This thesis investigates these models to measure and quantify the damages caused by bilateral lesions on CST fibers.

To extract the CST is a major challenge of this thesis, because the isolation of the CST cannot be achieved by using reference atlas, due to the small brain of subjects and the completely changed brain structure of children with CP. By consequence,

the tracking method is used. This thesis defines a semi-automated pipeline to isolate the CST in severely-deformed infant brains.

The next objective of this work is to characterize the CST modifications due to CP, by using the different models. In the literature, only few information has been found on CST structure of children with bilateral lesion. The unilateral pathology is much more investigated. The DTI model is therefore applied to validate the results found in the literature for unilateral lesion, on subjects with bilateral lesions. This lack of literature is reinforced for the NODDI model for which only one scientific article has been found for children with unilateral lesion. The application of this model is by consequence even more challenging than DTI.
This thesis define a framework to extract the metrics of these different models and to compare the control subjects with the children with CP in an objective and quantitative way. This comparison allows to understand the CST modifications in children with bilateral lesions.

This work is composed as following. The first part is a general explanation of MRI and DWI. The second part describes of the different microstructure models. The third part explains the cerebral palsy pathology and the results found in the literature for the microstructure models applied on subjects with CP. The fourth part applies these models on data of children with lesions in both hemispheres of the brain. In this part, the first step is to describe the pipeline of CST extraction. The second step is to calculate the different microstructure metrics on this zone of interest. Finally, the last part of this work is the statistical analysis to compare the control and CP populations.

Chapter 1

Theoretical background

The first part of this work is a general MRI overview with an explanation of physic principles on which MRI is based, a description of a typical sequence acquisition and an explanation of image construction. The classical MRI allows to create anatomical images but this information is not sufficient to understand how the brain works. This is the reason why some other techniques were investigated to measure and quantify more information. Diffusion Weighed Imaging is one of these techniques and is described at the end of this chapter.

1.1 MRI: Magnetic Resonance Imaging

MRI allows the creation of anatomical and functional images. This technique is widely used because it is a non-invasive technology: MRI is based on magnetic fields and radio waves. This section will explain how the images are created: first, by explaining the physical principles in the magnetic resonance section. Afterwards, a Spin-echo sequence, typical sequence, will be described. And finally, the image formation will be analyzed.
This section was written based on three papers: [6] [7] [8].

1.1.1 Magnetic resonance

The hydrogen nuclei have an intrinsic angular rotation called spin. Because these nuclei are positively charged, their rotation creates a magnetic field. Each nucleus corresponds to a dipole with a magnetic moment μ_i and their sum is the net magnetization (M):

$$M = \sum_i \mu_i$$

By adding a large external magnetic field B_0, the dipoles will be reoriented from their random position (M=0) to be aligned with the field: in parallel or anti-parallel direction. Considering B_0 in the direction of the z-axis, spin is either up, parallel with a low energy state or down, anti-parallel with a high energy state.
The occupation ratio of these two states follows a Boltzmann distribution:

$$\frac{N_\uparrow}{N_\downarrow} = exp(\frac{\Delta E}{kT})$$

with:

- k, the Boltzmann's constant;
- T, Temperature;
- $\Delta E = \gamma h B_0$, Energy Difference between spin up and spin down (h= Plank's constant).

The spins rotate with a small angle around the axis of the B_0 field, as to describe a cone. This is called the precession (Fig. 1.1). The frequency of this rotation is the Larmor frequency ω_0 and is proportional to the main magnetic field strength:

$$\omega_0 = \gamma B_0$$

The gyromagnetic factor, γ, is a constant defined for each sensitive atomic nucleus, e.g. for hydrogen nucleus: $\frac{\gamma}{2\pi} = 42.574$ [MHz] in a magnetic field strength of 1 Tesla.

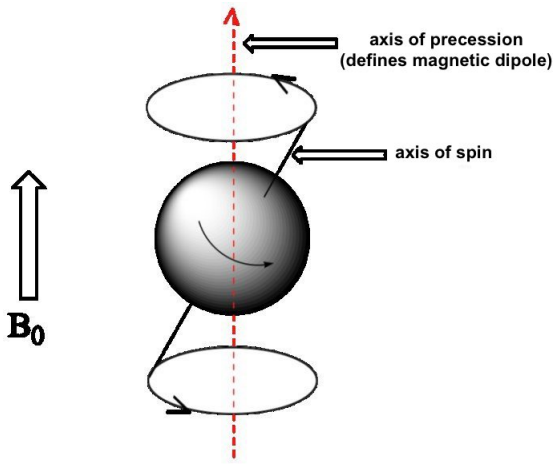

Fig. 1.1 – Spin motion in an external magnetic field B_0 [9].

The net magnetization is composed of two components. The first one is the **longitudinal** magnetization, aligned with the z-axis. The number of parallel spins being greater than the anti-parallel ones within the B_0, this leads to $\Delta E \neq 0$ and $M_z \mathbf{e_z} = M_0 \mathbf{e_z}$. The second component of the net magnetization is the **transverse magnetization**. Since the spins do not rotate in phase, their sum is a null total transverse magnetization: $M_{xy} \mathbf{e_{xy}} = 0$.

$$M = M_z \mathbf{e_z} + M_{xy} \mathbf{e_{xy}} = M_0 \mathbf{e_z}$$

A RadioFrequency (RF) pulse is applied by a coil leading to a much smaller second magnetic field (B_1) in the xy-plane.
The sum of these two magnetic fields leads to a spiral movement of the spins, which is due to two precession angular frequencies, one around B_0 and the other around B_1 (Fig. 1.2).

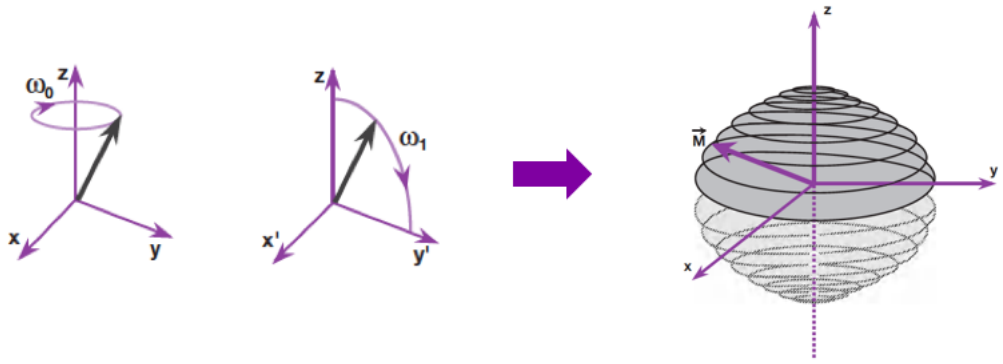

Fig. 1.2 – Two precession movements, due to the two magnetic fields (B_0 and B_1), compose the spiral movement of the spins [7].

The magnetic resonance is the result of the interaction between spins and RF. The RF will enter in resonance with the nuclei only if its frequency is the same than the precession frequency of the spins.
Therefore, the spins which have a frequency corresponding to RF, will move from the equilibrium by absorbing the electromagnetic energy. This step corresponds to the **excitation**. Due to this excitation, the initial magnetization, M_{z0}, changes and can be decomposed by a $M_z\mathbf{e_z}$ component and a $M_{xy}\mathbf{e_{xy}}$ component (Fig. 1.3).

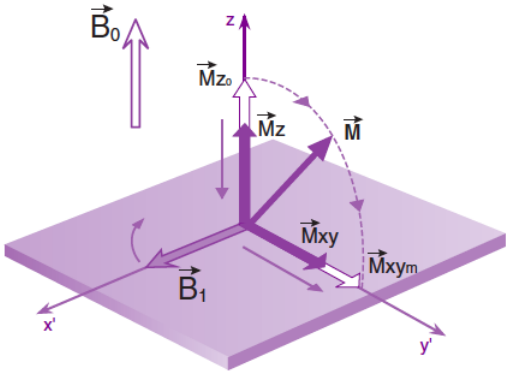

Fig. 1.3 – Description of the magnetization in the 3D plan [7].

At the end of the pulse, the longitudinal component disappears (the number of parallel and anti-parallel spins is equal) and the transverse component is maximal. After this pulse, the system tends to go back to its stable state: this step is called the **relaxation**.

This relaxation is composed of two parts, the longitudinal and transverse relaxations (Fig. 1.4):

- The longitudinal relaxation is due to the interaction between the spins and the lattice. When the spins go from a high energy state to a lower one, they release their energy into the surrounding lattice.

This relaxation is characterized by an exponential curve with a T_1 constant. At T_1, the longitudinal magnetization has reached 63% of its final value.

- The transverse relaxation is created by the spins getting out of phase. Since the spins interact together temporary and randomly, a cumulative loss of phase is created, resulting in a decrease in the transverse magnetization. This is characterized by a T_2 constant. At T_2, the transverse magnetization felt to 37% of its initial value.
  This relaxation is due to the intrinsic interaction between neighboring nuclei but also due to the inhomogeneity of the applied field. The addition of this second element modifies the T_2 constant to T_2^*.

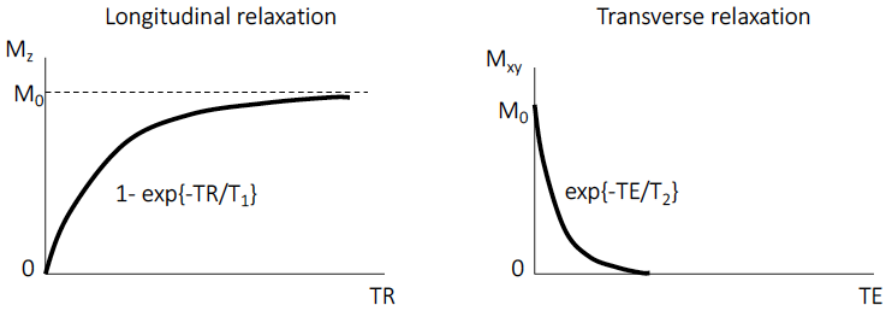

Fig. 1.4 – The relaxation phase of the spins is composed by a longitudinal and a transverse relaxation. The two relaxations are defined by an exponential function (positive or negative) [10].

1.1.2 Spin echo sequence

To measure the real interaction between the spins and to consequently measure the T_2 constant, a technique was developed: the spin echo. Since the inhomogeneity of the applied field is constant, the spin echo allows to eliminate the dephasing induced by these inhomogeneities. To realized that, a RF pulse of 180° is added in the sequence. A spin echo sequence (Fig. 1.5) starts with an exciting 90° RF pulse at time t=0. Just after this pulse, the spins start dephasing. After a TE/2 time, the 180° RF pulse is applied. It creates a mirror flip that reverses the spin's rotation direction and the spins are rephasing. After an echo time (TE), the spin will again be in phase. This sequence allows to characterise the transverse magnetization thanks to the T_2-constant (Fig. 1.6).

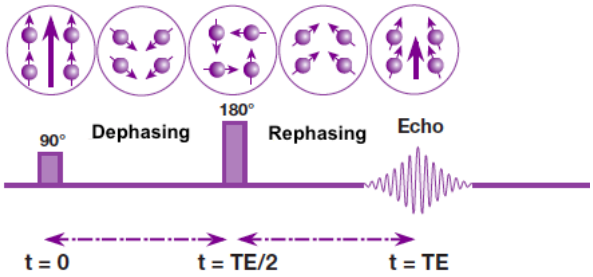

Fig. 1.5 – Spin-echo sequence [7].

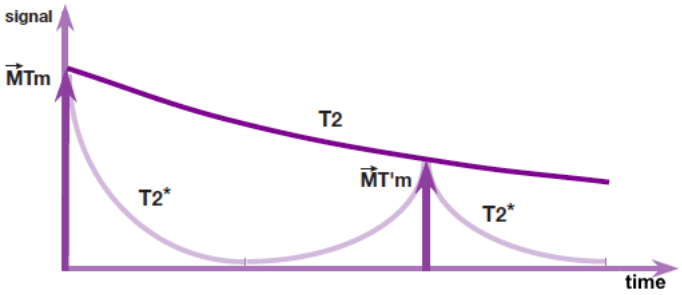

Fig. 1.6 – The transverse magnetisation that is normally described by a $T_2{}^*$ constant due to inhomogeneities in the field, can be expressed with a T_2 constant thanks to the spin-echo sequence [7].

1.1.3 Imaging

To create an image, the patient's area of interest needs to be selected and the MR-signal to be localized. Magnetic field gradients are used to excite the zone. A gradient field is a magnetic field oriented in $\mathbf{e_z}$, and varies with its position along a spatial direction $\mathbf{e_x}$. $G_x\mathbf{e_x}$ is a linear gradient field, with a slope $G_x = \delta B_z/\delta x$, defined as the magnetic gradient (Fig. 1.7). G_y and G_z are defined similarly.

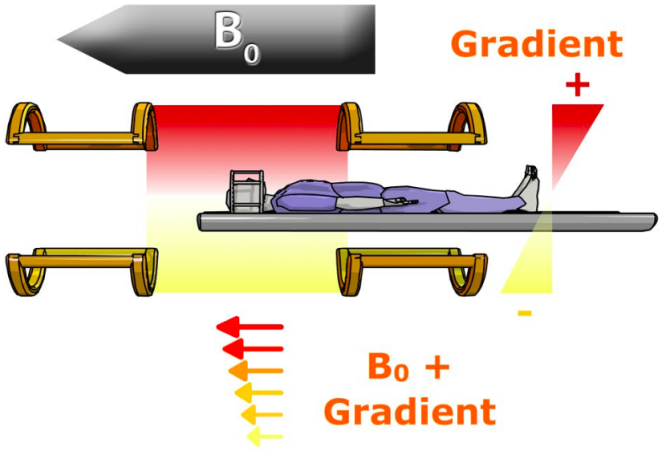

Fig. 1.7 – To select the slice of the body that needs to be scanned, a linear gradient is applied by coils [11].

Due to the addition of this gradient field (much smaller than the external magnetic field B_0), the total field becomes:

$$\mathbf{B}(\mathbf{r}) = (B0 + \mathbf{G}\cdot\mathbf{r})\mathbf{e_z} = B(r)\mathbf{e_z}$$

with $\mathbf{G} = (G_x, G_y, G_z)$, the magnetic field gradient and $\mathbf{r} = (x, y, z)$, the position. A slice with a thickness of Δz is excited by a band of RF-pulses:

$$\Delta f = \frac{\gamma}{2\pi} G_z \Delta_z$$

This spatial information is encoded by a phase- and a frequency-encoding.
In the selected slice, the contrast is created by the differences in intensity due to the different T2 times of the different tissues (Fig. 1.8).

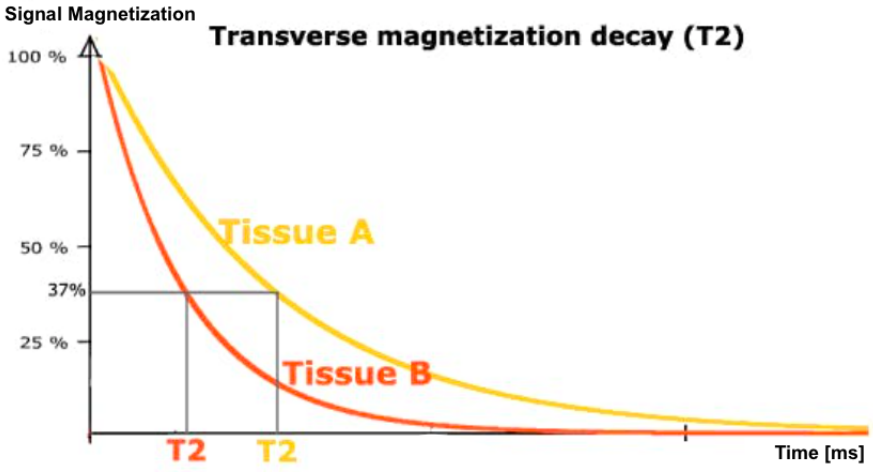

Fig. 1.8 – Due to their compositional differences, two different tissues have different transverse magnetizations and so different T2 constants [11].

The signal intensity is measured in the temporal domain and encoded in the frequency domain (Fig. 1.9). To reconstruct the image, the information needs to be transformed from the frequency domain to the spatial domain (Fig. 1.9). To go from one domain to the other, the (inverse) Fourier Transform is used.

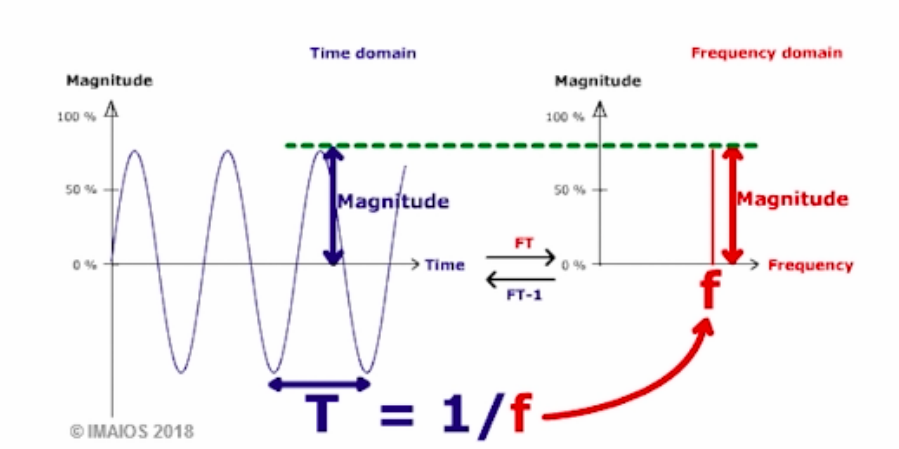

Fig. 1.9 – To go from the time domain in which the signal is measured to the frequency domain in which the information is encoded, the Fourier Transformation is applied [11].

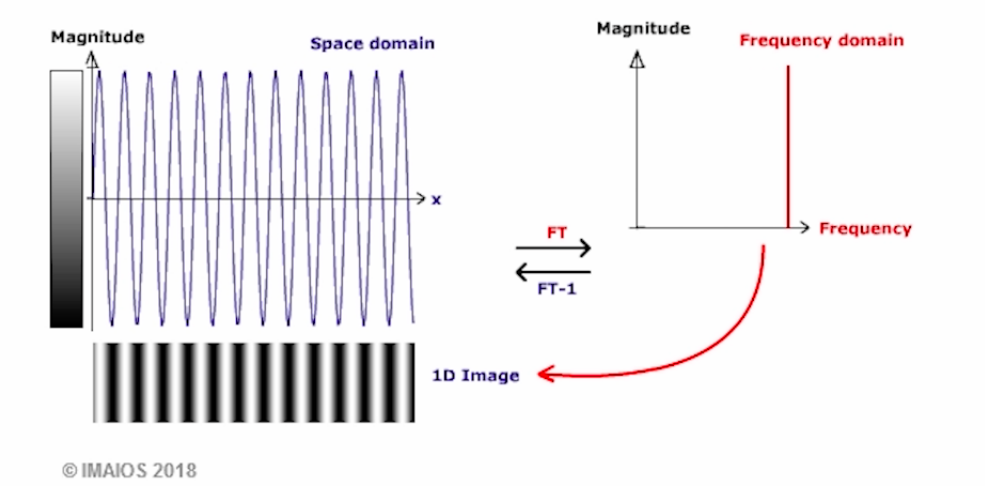

Fig. 1.10 – To go from the frequency domain in which the information is encoded to the spatial domain in which the image is created, the inverse Fourier Transformation is applied [11].

1.2 DWI: Diffusion Weighted Imaging

Based on MRI, different techniques allow to obtain complementary information. Diffusion Weighted Imaging (DWI), characterizing the brain structures according to their diffusion properties, is one of them.
Diffusion is the random movement of molecules, often described via Brownian motion. This diffusion can be free or restricted (Fig. 1.13), e.g. in the cerebrospinal fluid or in the intra- and inter-cellular space, respectively [12].

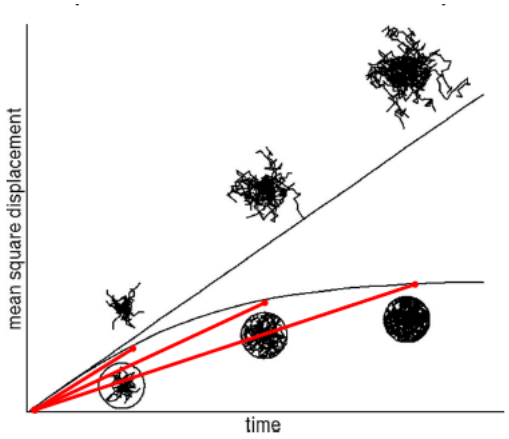

Fig. 1.11 – The molecules diffusion can be free and linear, or restricted and reaches a saturation [10].

The DWI contrast is based on this difference in diffusion rate. It generates a quantitative map that represents the spatial distribution of the diffusion rate. To obtain this information, a Pulsed-Gradient Spin Echo (PGSE) sequence is used (Fig. 1.12). This sequence is a spin echo sequence with two linear magnetic fields $B_1(r) = G \cdot r$.

The sequence is characterized by G, the amplitude of the gradient, δ, their durations, and Δ, the interval between the first and second gradients [12].

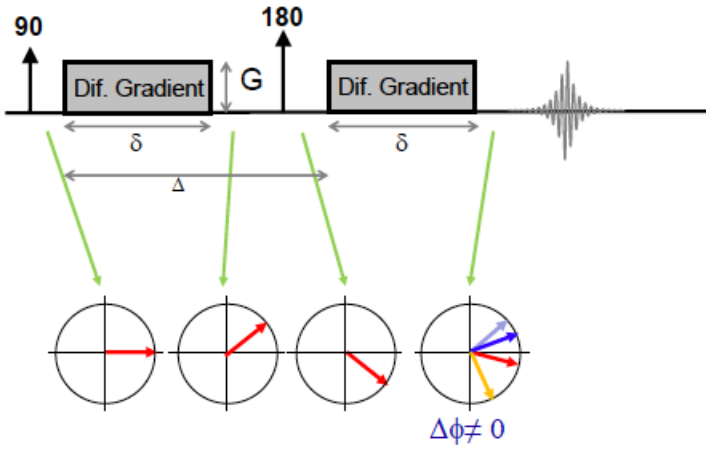

Fig. 1.12 – Pulsed-Gradient Spin Echo sequence. On the bottom, the effect of each element on the spins. On the last circle, different arrows are presented, which shown the different positions of the spins due to the difference in diffusivity [10].

The PGSE sequence (Fig. 1.12) starts with a 90°-pulse to excites the spins. Then, a first gradient, which dephases the spins, is applied during a time δ. When the 180°-pulse is applied, it flips all the magnetic moments into the opposite direction and reverses the rotation direction. After this pulse, the second gradient is applied with the same duration, direction and intensity as the first one. Its effect is to refocus the spins [12]. After this second gradient, two cases are possible [10]:

1. The molecules did not move and their phases are by consequence perfectly refocused.

2. Diffusion occurs, the molecules did move and the refocusing is imperfect. The signal attenuation is not completely compensated, corresponding to the different colored arrows in Fig. 1.12. The degree of signal loss represents the degree of diffusion: more signal is lost if the degree of randomness is high, while less signal is lost if the degree of randomness is low.

The diffusion gradients of a PSGE sequence are characterized by a b-value. This value is defined by the Stejskal-Tanner equation [12]:

$$b = \gamma^2 G^2 \delta^2 \left(\Delta - \delta/3\right)$$

with γ, the gyromagnetic ratio.

The images provide by DWI represent the signal intensity resulting from this kind of sequences. The images acquired with a $b0$ (b-value=0) correspond to pure T2-weighted images while the images acquired with an other b-value are partially T2- and diffusion- weighted.

Diffusion maps can be calculated based on the difference in the images acquired with a *b0* and a b-value.

$$S(b) = S(0) \cdot e^{-b \cdot ADC}$$

The diffusion rate is determined by the apparent diffusion coefficient (ADC); the term *apparent* is used due to the fact that different factors influence the diffusion (micro-architecture, energy-dependent transportation mechanisms). This value can be plotted on an ADC map, a high ADC value corresponding to a high rate of diffusion (e.g. cerebrospinal fluid (CSF)) [13].

This ADC technique avoids the T2-effect that may mimic or obscure lesions. The value does not depend on the field strength [10].

Diffusion characterisation

The diffusion is a 3D phenomenon with different directions and shapes, depending on the different structures of the brain. The diffusion in white matter is represented by an ellipsoid (Fig. 1.13a), with a diffusion along a principal axis and limited in the perpendicular direction. This type of diffusion is an anisotropic diffusion. The diffusion in the CSF is associated with a sphere (Fig. 1.13b), which means that the diffusion goes in all directions, and is characterized as an isotropic diffusion.

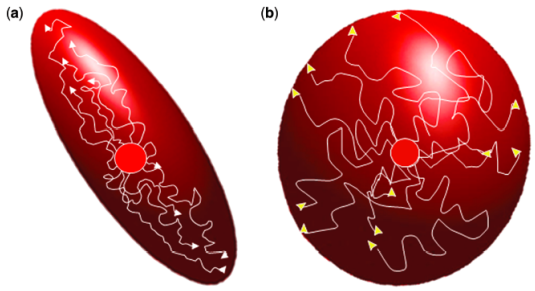

Fig. 1.13 – The diffusion can be anisotropic, with a principal diffusion axis and can be described by a ellipse (a), or it can be isotropic with no preferred diffusion axis and be modeled by a sphere (b) [12].

Chapter 2

Models

Different microstructure models were created to interpret the DWI measurements. Four of these models are investigated in this section: Diffusion Tensor Imaging (DTI), Diffusion Kurtosis Imaging (DKI), Constrained Spherical Deconvolution (CSD) and Neurite Orientation and Dispersion Density Imaging (NODDI). For each of these models, a general description of the model is done, followed by its advantages and limitations.

2.1 DTI: Diffusion Tensor Imaging

DTI is based on DWI measurements. The gradients of the PGSE sequence can be applied in different directions, to capture the diffusion direction. For example, if a white matter tract is present along the gradient direction, the signal will be suppressed (Fig. 2.1). The DTI model is based on this technique.

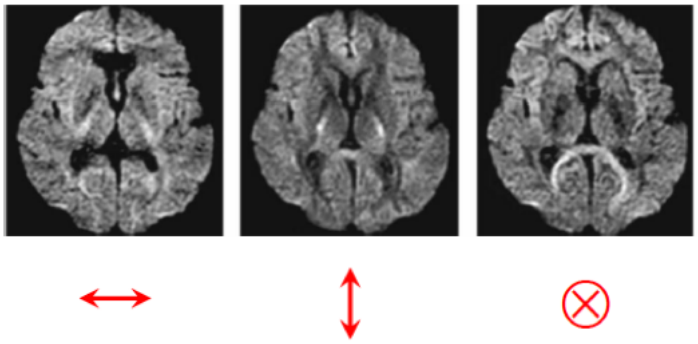

Fig. 2.1 – Application of gradient in different directions (represented in red)[10].

By applying the gradient in different directions, the value of a diffusion tensor can be calculated. Since a 3D information is needed, this tensor (**D**) is a second order tensor (see matrix 2.1) with three principal diffusivities along three mutually perpendicular directions (respectively: eigenvalues and eigenvectors) [12].

$$\begin{pmatrix} D_{xx} & D_{xy} & D_{xz} \\ D_{yx} & D_{yy} & D_{yz} \\ D_{zx} & D_{zy} & D_{zz} \end{pmatrix} \tag{2.1}$$

In this matrix, $D_{xy} = D_{yx}$, $D_{xz} = D_{zx}$ and $D_{yz} = D_{zy}$, therefore, only six non-collinear directions are needed in the diffusion-weighted sequence to estimate the diffusion tensor.
The signal obtained after DTI is defined by the Stejskal-Tanner equation [14]:

$$S_k(b) = S(0) \cdot e^{-b\mathbf{g_k}^T D \mathbf{g_k}} \tag{2.2}$$

This equation links the measured diffusion-weighted signal S_k along a gradient direction $\mathbf{g_k}$ to the non-attenuated signal *S(0)*.

2.1.1 DTI metrics

Based on this data, different parameters are estimated with the DTI model:

- The axial diffusivity (AD) corresponds to the diffusion along the principal axis:

$$AD = \lambda_1$$

- The radial diffusivity (RD) is the average diffusion along the two others axes:

$$RD = \frac{\lambda_2 + \lambda_3}{2}$$

- The mean diffusivity (MD) is the diffusion averaged in the three directions:

$$MD = \frac{1}{3} tr(D) = \frac{\lambda_1 + \lambda_2 + \lambda_3}{3}$$

- The fractional anisotropy (FA) represents the fraction of the diffusion that is anisotropic:

$$FA = \sqrt{\frac{3}{2}} \frac{\sqrt{(\lambda_1 - MD)^2 + (\lambda_2 - MD)^2 + (\lambda_3 - MD)^2}}{\sqrt{\lambda_1^2 + \lambda_2^2 + \lambda_3^2}}$$

  FA is the difference between the tensor with an ellipsoid shape and a perfect sphere. It takes values between 0 and 1, zero if the diffusion is completely isotropic (perfect sphere) and one if the diffusion is highly anisotropic (ellipsoid) (Fig. 2.2).

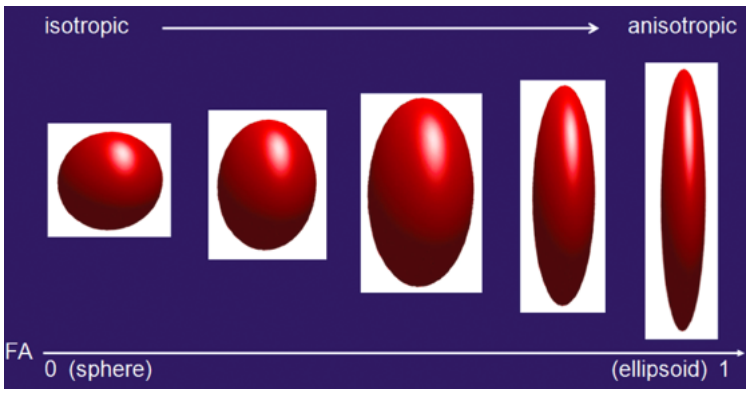

Fig. 2.2 – FA takes value between 0 and 1, between this interval, the model evolves form a sphere/isotropic configuration to an ellipse/anisotropic configuration [12].

All these metrics can be calculated for an entire map, as shown in Fig. 2.3.

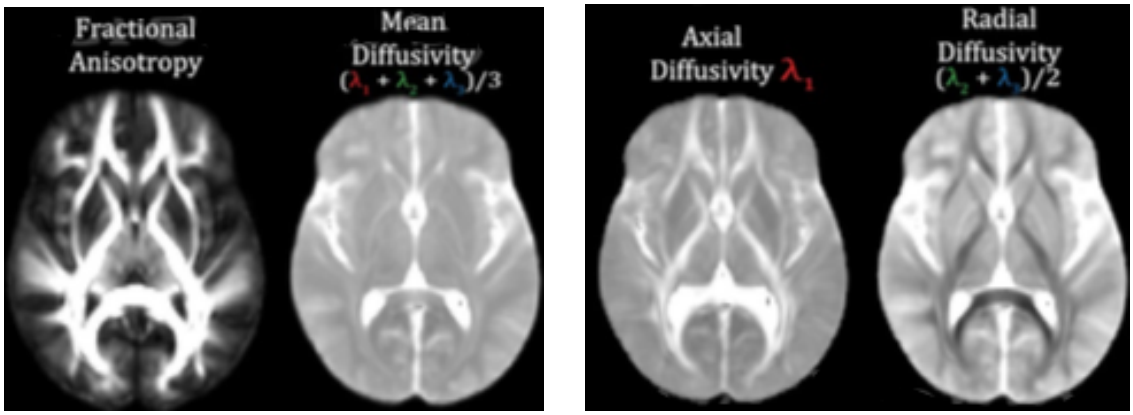

Fig. 2.3 – Metrics calculated with DTI [15].

Colors derived from DTI

Colored images are another type of images that can be created, with each principal direction in a different color: blue for superior–inferior, red for left–right, and green for anterior–posterior. The major eigenvector field of each pixel is therefore represented by the corresponding color.
To have a better visualization of the white matter, the brightness of the color is usually controlled by tensor anisotropy (FA)[14]. An example of this map is shown in Fig. 2.4.

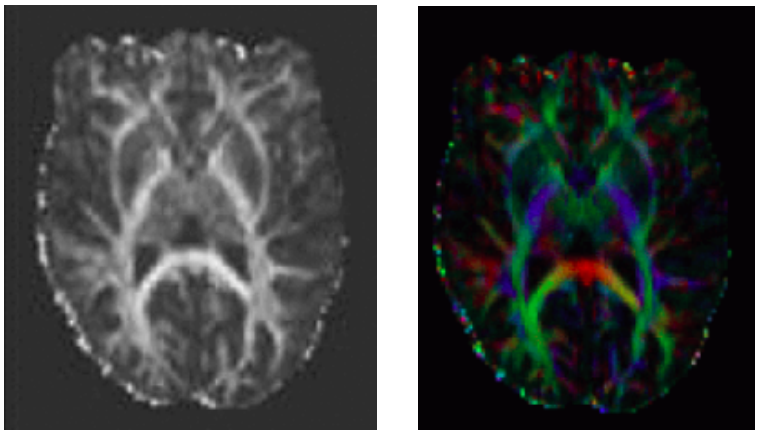

Fig. 2.4 – Classical FA image on the left and colored eigenvector modulated by the FA image on the right [16].

DTI tractography

The tractography's aim is to estimate the trajectories of the neuronal fibers. DTI tracking is based on stepping (typically a 1mm step) in the direction of the principal eigenvector, corresponding to the fastest diffusion direction.

A first method is the Euler's algorithm. It follows the eigenvector during a determined number of steps. The second-order Runge-Kutta algorithm is a second method that can be used. It follows the tangent of the eigenvector for half of the step, then a new tangent is calculated at the midpoint of the interval and used to take the full step [14].
After this first step, the anatomical tract of interest is selected through virtual dissection, in which inclusion/exclusion regions are defined. A more automatized method to select it is atlas-based and uses prior knowledge to select trajectories [14].

2.1.2 DTI advantages

DTI is the simplest model of diffusion signal, this is why it is widely used. The simplicity of the model is due to the low number of parameters (i.e.six), and consequently, it does not require a huge calculation time.

2.1.3 DTI limitations

The simplicity of the model is also its disadvantage. It only considers two cases: no preferential direction for isotropic diffusion or one preferential direction for anisotropic diffusion. This model is correct when only one fascicle orientation is present in the voxel, but the model is not able to predict different orientations in the same voxel. A significant fraction of white matter voxels in the brain contains fibers oriented in different directions [14]. In these voxels, the diffusion tensor model is not reliable. As shown in Fig. 2.5, when two fibers populations are crossing within a voxel, the diffusion in this voxel is modeled by a sphere, corresponding to an isotropic diffusion instead of two ellipsoids, corresponding to two anisotropic diffusion directions.

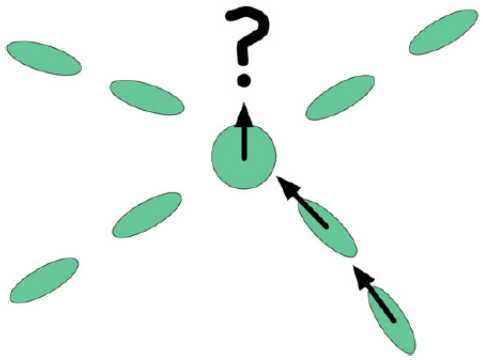

Fig. 2.5 – In a voxel with a crossing of two populations, the FA will be averaged and associated to a sphere. Therefore, a non-matching in the tract appears [14].

Another limitation of DTI is the biological interpretation. It is complicated due to the different causes that can be associated with an increase or decrease in metrics. For example, an increase of FA can be due to cells death, change in myelination, increase in extracellular or intracellular water [17].

2.2 DKI: Diffusion Kurtosis Imaging

Diffusion kurtosis imaging (DKI) is a higher order diffusion model than DTI. In order to quantify the degree of non-gaussianity in the signal attenuation, a quadratic term is added in the b-value of DTI. The DKI is by consequence an extension of the DTI model. Like in DTI, the apparent kurtosis coefficient (AKC) can be defined. It corresponds to the coefficient of the additional term related to the apparent excess kurtosis, that quantifies the non-gaussianity. To calculate the fourth-order diffusion kurtosis tensors (DKT), at least 15 different gradient directions need to be applied [18].

DTI equation 2.2 is rewritten in the following form :

$$S(b, \mathbf{g}) = S(0)exp\left(-b \sum_{i,j=1}^{3} g_i g_j D_{ij}\right)$$

The second-order term is added to this first equation to obtain the DKI equation :

$$S(b, \mathbf{g}) = S(0)exp\left(-b \sum_{i,j=1}^{3} g_i g_j D_{ij} + \frac{b^2}{6}\left(\sum_{i=1}^{3} \frac{D_{ii}}{3}\right)^2 \sum_{i,j,k,l=1}^{3} g_i g_j g_k g_l W_{ijkl} \right)$$

with $\mathbf{W}$, the apparent kurtosis tensor.

2.2.1 DKI advantages

The diffusion tensor properties are better estimated with the DKI model than with the DTI model. The non-Gaussian diffusion added element can be a sensitive marker for tissue characterization [19].

2.2.2 DKI limitations

DKI is more susceptible to data artifacts than DTI, due to its increased model complexity, higher acquisition demands, and longer scanning times [19].

2.3 CSD: Constrained Spherical Deconvolution

The Constrained Spherical Deconvolution (CSD) technique is also based on diffusion weighted imaging. In comparison with the DTI model, the advantage of this technique is to address the crossing fibers problem. The CSD model uses a HARDI (High Angular Resolution Diffusion Imaging) protocol. It is typically based on a larger number of directions and by consequence, captures higher angular frequencies than with DTI [20]. Since the CSD model is more complex, it can be reliably fitted on a larger number of data. In contrast, due to the DTI's intrinsic limitations, the angular resolution is limited, no matter the number of directions acquired [17]. As result, DTI analysis will be typically applied to small data sets, where CSD could over-fit the noise in the data and indicate spurious peaks in every voxel [21]. Therefore, if CSD is applied, more time should be dedicated to acquire a high direction number.

The CSD model provides estimation of the full fiber orientation distribution function (fODF) in each voxel whatever the number of fiber orientations [20]. In DWI, the total signal within a voxel is due to the addition of the signal for all the fiber populations present in this voxel (Fig. 2.6) [21]. This Diffusion Weighted (DW) signal is given by the convolution of the fODF and the response function of a fiber. The fODF can therefore be calculated by inverting the equation and by calculating the spherical deconvolution between the fiber response and the measured DW signal.

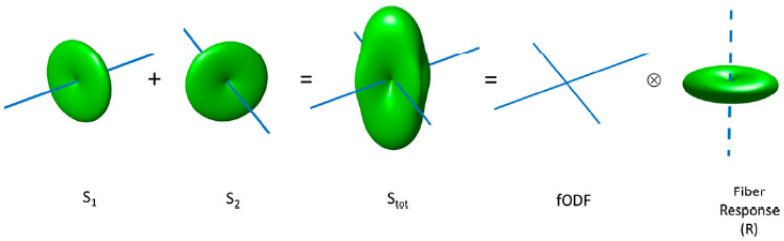

Fig. 2.6 – The measured signal (S_{tot}) is composed of two different fiber orientations (S_1 and S_2), and can be obtained by the convolution of the fiber orientation distribution function (fODF) and a typical fiber response [21].

The CSD algorithm solves the equation [21] :

$$\widehat{f} = \min_{f} \quad \|Hf - m\|^2 + \lambda \|Af\|^2$$

with:

- f, the unknown vectors of coefficients of the fODF, estimated as those that minimize the least-squares fit of the predicted signal to the data m at the voxel of interest;
- m, DW signal intensities measured on a single shell in q-space;
- H, the predicted DW signal and $H = MR$, where M maps Spherical Harmonic () coefficients to amplitudes along the DW directions sampled, and R is a diagonal matrix of response function coefficients performing the spherical convolution in the spherical harmonic domain;
- the coefficients f also minimize the sum of squares of the negative amplitudes in the fODF, with the matrix A mapping the SH coefficients to a dense set of uniformly distributed directions.

This last element only penalizes the negative values. The solution is therefore not guaranteed to be non-negative, even if this possibility is physically impossible. This solution that may seem sub-optimal allows different advantages: computational efficiency, noise sensitivity reduction and SH basis utilization. The constraint of non-negativity can be reinforced by increasing the λ parameter, resulting in a decrease of the angular resolution [21].

2.3.1 CSD advantages

The main advantage of this technique is to take into account different fiber orientations with a reasonable calculation time.

2.3.2 CSD limitations

One limitation of the spherical deconvolution is that the estimation of the response function is based on empirical measures. This function is estimated in the same way all over the brain. But from a biological point of view, it is clear that this value is not constant: the diameter of axons varies along the white matter tract.

2.4 NODDI: Neurite Orientation and Dispersion Density Imaging

The NODDI model [22] is divided in three parts: the cerebrospinal fluid (CSF), and the tissue model composed of the intra-cellular model and the extra-cellular model. The intra-cellular compartment is the space bounded by the membrane of neurites (dendrites and axons) and the extra-cellular one is the space around the neurites, occupied by glial cells and somas in the gray matter.
These three microstructural environments have different water diffusion properties, and hence, different normalized MR signals and different models (Fig. 2.8).

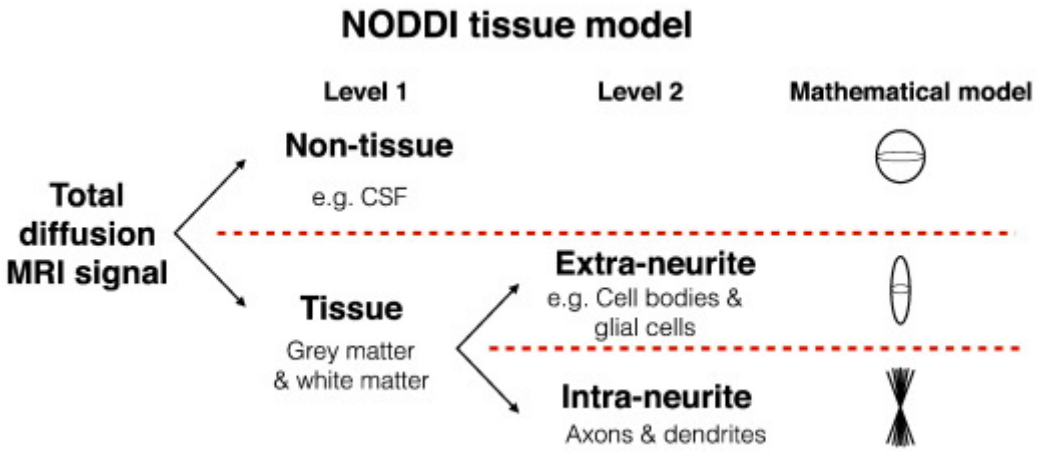

Fig. 2.7 – The NODDI model is a two levels model. The first level separates the tissue and the non tissue, the second, the intra- and the extra-cellular compartment. Each one of the three defined categories can be associated with a mathematical model: a sphere, an ellipsoid or a set of sticks [23].

The full normalized NODDI model A is defined as:

$$A = (1 - \nu_{iso})(\nu_{ic}A_{ic} + (1 - \nu_{ic})A_{ec}) + \nu_{iso}A_{iso}$$

with:

- A_{ic}, A_{ec} and A_{iso}, the normalized signals of the intra-cellular space, extracellular space and CSF respectively;
- ν_{ic}, ν_{ec} and ν_{iso}, the fractions occupied by the intra-cellular space, the extra-cellular space and the CSF respectively;
- $\nu_{ic} + \nu_{ec} = 1$.

The description of the three sub-models is explained below.

2.4.1 Intra-cellular model

In the intra-cellular compartment, the diffusion is restricted perpendicularly to the neurite membranes and unhindered along them. This space is modeled as a set of sticks (cylinders of zero radius). The normalized signal, A_{ic}, is:

$$A_{ic} = \int f(\mathbf{n})\, e^{-bd_{\parallel}(\mathbf{q}\cdot\mathbf{n})^2} d\mathbf{n}$$

with:

- $\mathbf{q}$, the gradient orientation;
- b, the b-value;
- $f(\mathbf{n})$, the orientation distribution function, modeled by a Watson distribution that captures the dispersion in orientation and provides a good representation for high orientation dispersion like in gray matter and for low orientation dispersion in the most coherent white matter:

  $$f(\mathbf{n}) = M\left(\frac{1}{2}, \frac{3}{2}, \kappa\right)^{-1} e^{\kappa(\boldsymbol{\mu}\cdot\mathbf{n})^2}$$

  where M is a confluent hypergeometric function, $\boldsymbol{\mu}$ is the mean orientation, and κ is the concentration parameter that measures the extent of orientation dispersion about $\boldsymbol{\mu}$;
- $f(\mathbf{n})\, d\mathbf{n}$, the probability of finding sticks along orientation n;
- $e^{-bd_{\parallel}(\mathbf{q}\cdot\mathbf{n})^2}$, the attenuation due to unhindered diffusion along a cylinder with intrinsic diffusivity $d_{\parallel}$ and orientation $\mathbf{n}$.

2.4.2 Extra-cellular model

In the extra-cellular part, the diffusion is hindered by the presence of neurites but not restricted. The compartment is modeled by a simple anisotropic Gaussian diffusion and represents orientation-dispersed cylinders. The normalized signal, A_{ec} is:

$$\log A_{ec} = -b\mathbf{q}^T \left(\int f(\mathbf{n}) D(\mathbf{n}) d\mathbf{n} \right) \mathbf{q}$$

with:

- b, the b-value;
- $\mathbf{q}$, the gradient orientation;
- $\int f(\mathbf{n})D(\mathbf{n})d\mathbf{n}$, the apparent diffusion tensor of the compartment;
- f, the distribution of axon orientation;
- $D(\mathbf{n})$, the diffusion tensor for axons with principal direction of diffusion n.

2.4.3 CSF model

The space occupied by cerebrospinal fluid is modeled as isotropic Gaussian diffusion with diffusivity d_{iso} (the diffusion coefficient for free water at 37 °C). The normalized signal for this compartment is:

$$A_{iso} = e^{-bd_{iso}}$$

2.4.4 NODDI metrics

The metrics calculated by NODDI quantify the volume fraction within neurites and overall neurite coherence in each voxel. Different markers try to represent the microarchitecture of the brain tissues: isotropic volume fraction (ISOVF), intracellular volume fraction (ICVF) and orientation dispersion index (ODI).
ISOVF corresponds to the volume fraction of unhindered water (cerebrospinal fluid) and ICVF corresponds to the space within axons [24]. ODI is the main metric. It represents the fiber coherence and is defined as:

$$ODI = \frac{2}{\pi}\arctan\left(\frac{1}{\kappa}\right)$$

This index takes values between 0 and 1: if ODI is close to 1, the orientation dispersion is high like in gray matter, while if the value tends to zero, the orientation dispersion is low, like in CSF [24].

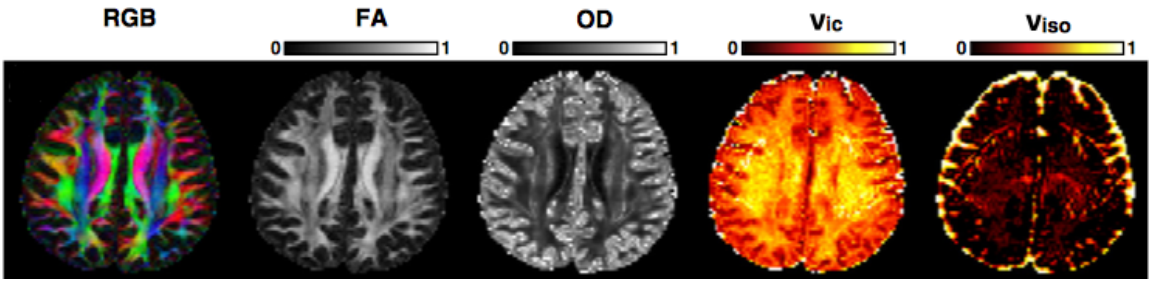

Fig. 2.8 – Map of the different metrics calculated by NODDI model. RGB: red, green, blue corresponding to the direction of the principal direction; FA: fractional anisotropy (DTI metric); ODI: orientation dispersion index; ν_{ic}: intracellular volume fraction; ν_{iso}: isotropic volume fraction [22].

2.4.5 NODDI advantages

The multi-compartments of the NODDI model estimate more directly the brain microstructures compared to the MD and FA with DTI model. Moreover, it focuses on neurites which are key markers of brain development and aging [22].

2.4.6 NODDI limitations

First, the model ignores the intra-axonal radial diffusivity. Moreover, it also considers only one single fascicle compartment per voxel, while in reality fascicle crossings occur a lot in the human brain. In this case, the voxel will be characterized by an increase in dispersion, but NODDI is not able to characterize each fascicle separately [4].
Finally, the computational time is increased in comparison with the DTI due to the mathematical complexity.

Chapter 3

Cerebral palsy

The aim of this thesis is to apply the models described in the previous chapter on children with CP. In this objective, a general comprehension of the pathology is needed. The first section is hence dedicated to give an explanation of the CP pathology. This description highlights different white matter tracts involved in CP. A way of isolating these tracts is explained in the second part. Finally, a section reviews the studies using DTI and NODDI in this specific pathology.

3.1 Pathology explanation

Non-progressive disturbances of the brain can arise during the fetal or infant development. It creates permanent disorders in the development of movement and posture. These groups of disorders correspond to CP [1].

The causes of CP are congenital, genetic, inflammatory, infectious or metabolic. They are different in function of the development state. Even if the lesion is static, its pattern can evolve due to the growth, the development plasticity and maturation of the central nervous system. In addition to the movement and posture disorders, some associated deficits are present in most cases: mental retardation, visual impairments and disorders of ocular motility, hearing impairment, epilepsy, speech and language disorders.

CP can be classified depending on the number of involved limbs: monoplegia, hemiplegia, diplegia, triplegia and quadriplegia. Monoplegia and triplegia are relatively uncommon [25]. This thesis focuses on subjects having lesions in both hemispheres of the brain. As the early diagnostics of CP are difficult to make, diplegia (both sides are involved, with lower-limbs more affected) and quadriplegia (the four limbs are affected, with in general one side more affected than the other) cases are considered in this work.

The motor system is composed of pyramidal and extrapyramidal systems in the brain, spinal cord and peripheral nervous system. In order to have a working motor system, all of these elements need to be intact. In the CP case, different elements can be impacted in function of the injury period.

In term infants (last part of third trimester and after birth), the disturbances are usually caused by hypoxic-ischemic encephalopathy (HIE), i.e. injury to the deep gray matter in the basal ganglia or thalamus (Fig. 3.1), or stroke, i.e. injury in to the motor cortex (Fig. 3.2).

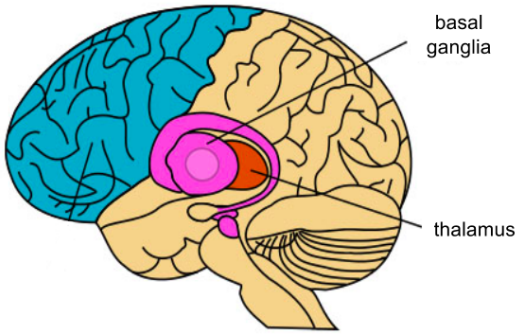

Fig. 3.1 – Basal ganglia and thalamus localization [26].

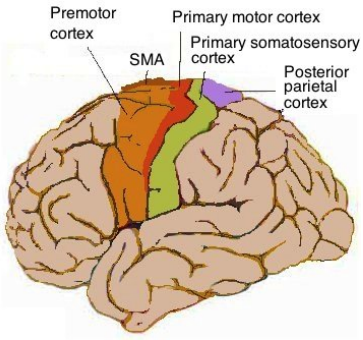

Fig. 3.2 – Motor cortex localization [27].

In preterm infants (first part of third trimester), the disturbance is caused by white matter injury in the corticospinal tracts or thalamocortical radiations from periventricular leukomalacia (most common ischemic brain injury in premature infants) or periventricular hemorrhagic infarction [5].
If the lesion occurs before the third semester, malformations arise.

These different lesions affect the maturation process and impair the structural integrity of the CST (Fig. 3.3), which is the most important tract for fine motor skills, and is among the first tracts to mature [3]. That is why this tract was principally analyzed in the application section.
It was shown that the development of the CST, through its maturation process (myelination, synaptic pruning and development, changes in axonal diameter and length and organization of pyramidal neuron firing patterns), can be measured by DTI [3].

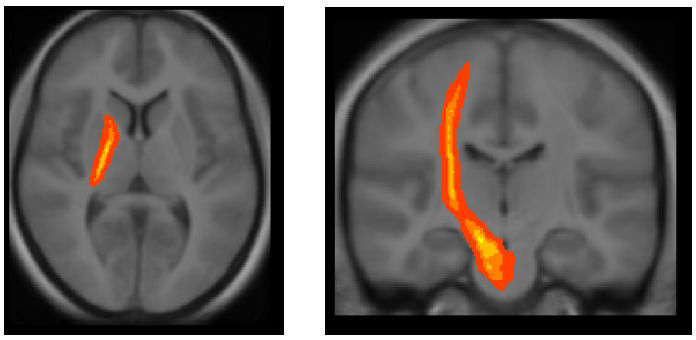

Fig. 3.3 – Projection Network : Cortico Spinal tract [28]. Axial and coronal views on the left and right respectively.

In addition, the somatosensory function is also impaired in children with CP. There is a correlation between the magnitude of somatosensory and movement impairments. The close interaction between the motor and the sensory system made it difficult to determine the contribution of each system to the functional impairments [29].

The adaptation of the two systems are different in the development of brain injury. During normal development, the CST descends from motor cortex to establish bilateral connections to the spinal cord. These bilateral projections are pruned through the third trimester and early childhood, leading to a predominantly controlateral system (Fig. 3.4 left in blue). In case of injury in the early development, early bilateral CST projections from the uninjured hemisphere persist, and the impaired hand is controlled via connections from the ipsilateral (uninjured) hemisphere (Fig. 3.4 middle and right in light blue). The axonal connections in the somatosensory system project almost entirely to one hemisphere and this property is kept even after injury in early development (Fig. 3.4 left and middle in red). The somatosensory axons can navigate around brain lesions that occur before the early third trimester to the reach primary somatosensory cortex in the controlateral cortex. In case of term injury, the thalamocortical projections and primary somatosensory cortex may be disrupted (Fig. 3.4 right in red). The somatosensory adaptations are therefore less robust than the motor one [29].

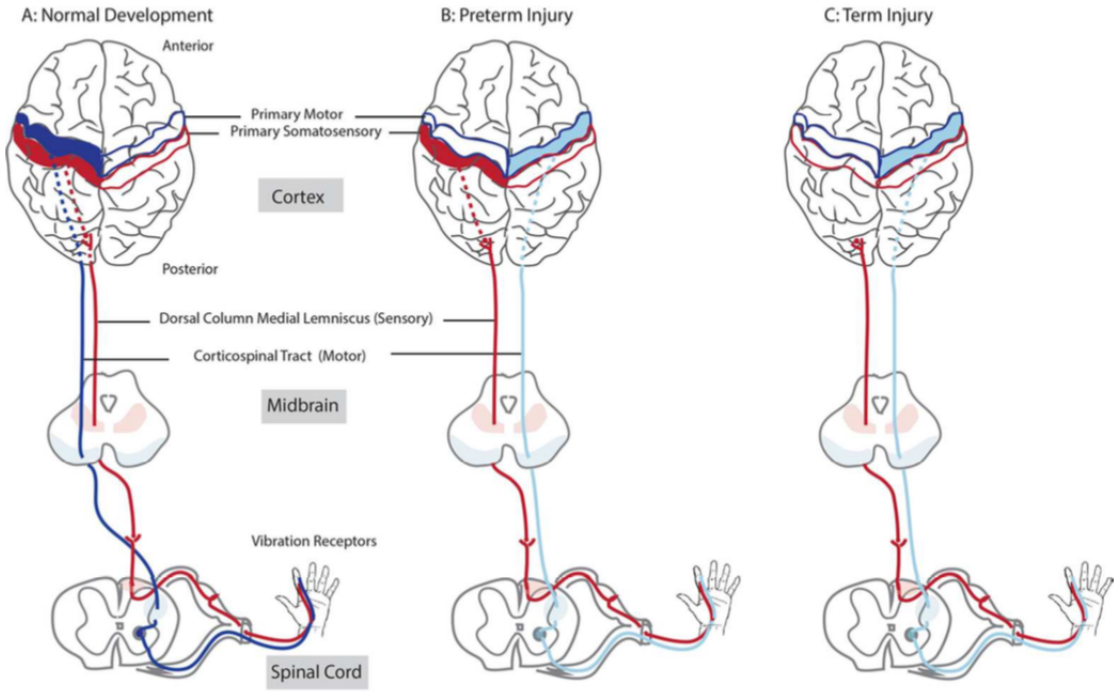

Fig. 3.4 – Motor and somatosensory tracts: in normal development (on the left), in case of preterm injury (in the middle) and in case of term injury (on the right) [29].

But what happen if lesions occur in both hemispheres? This thesis attempts to initiate an answer by analyzing the impact of bilateral lesions on white mater tracts.

3.2 Fibers tracking

A big challenge with the children with CP is that the normalization cannot be done, and therefore the reference atlas cannot be used. Another way to isolate the CST is with tracking methods. This step is therefore crucial for the following analysis.
Two techniques are considered: the DTI and the CSD (probabilistic) tracking.
Diffusion tensor tractography is limited. Indeed, the tensor model shows a high uncertainty in the estimated fiber direction in some areas due to complex fiber architecture or pathological changes.
This issue was addressed by CSD (see Section 2.3) which produces the complete fiber ODF in every voxel. That local fODF is then used by probabilistic fiber tracking algorithms which are more robust to complex white matter architecture such as fiber crossings [21]. Probabilistic fiber tracking is able to resolve complex fiber structure and could provide additional information about the pathology of altered fiber pathway [30].
To identify tracts, Region Of Interest (ROI) needs to be defined. The CST can be tracked using a seed in the primary cortex (Fig. 3.2) and by using the cerebral peduncles (Fig. 3.5) and the posterior limb of the internal capsule (PLIC) (Fig. 3.6) [30]. In order to have a more global view the two ROI are highlight in Fig. 3.7. A concrete example of CST tracking will be shown in Section 4.3.

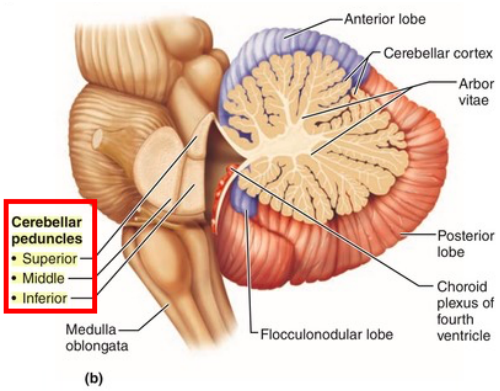

Fig. 3.5 – Position of the middle cerebellar peduncle [31].

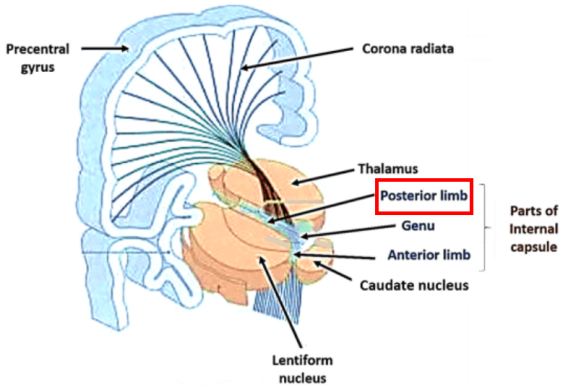

Fig. 3.6 – Position of the posterior limb of the internal capsule [32].

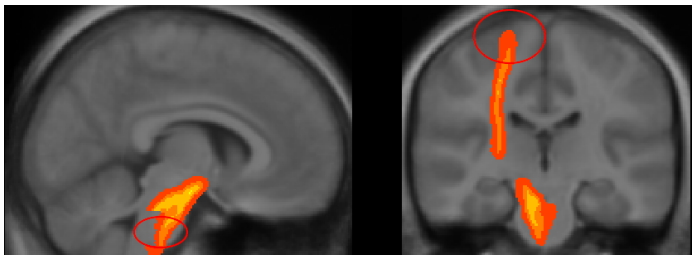

Fig. 3.7 – The position of the two ROI for CST tracking are circled in red on the projections of the corticospinal tract [28].

The thalamic projections to the somatosensory cortex (TRS1s) can be tracked by seeding in the thalamus (Fig. 3.1) and by using the somatosensory cortex (Fig. 3.4) as ROI [30].

Four distinct spatial characteristics can be seen on fiber tracts comparing subjects with CP to control subjects: dislocation of the major branch of the tract; local, continuous splitting of the tract into two separate branches; compaction of a nonsplit tract; or failure to delineate the fiber tract [30]. An example of their visual representations is shown in Fig. 3.8.

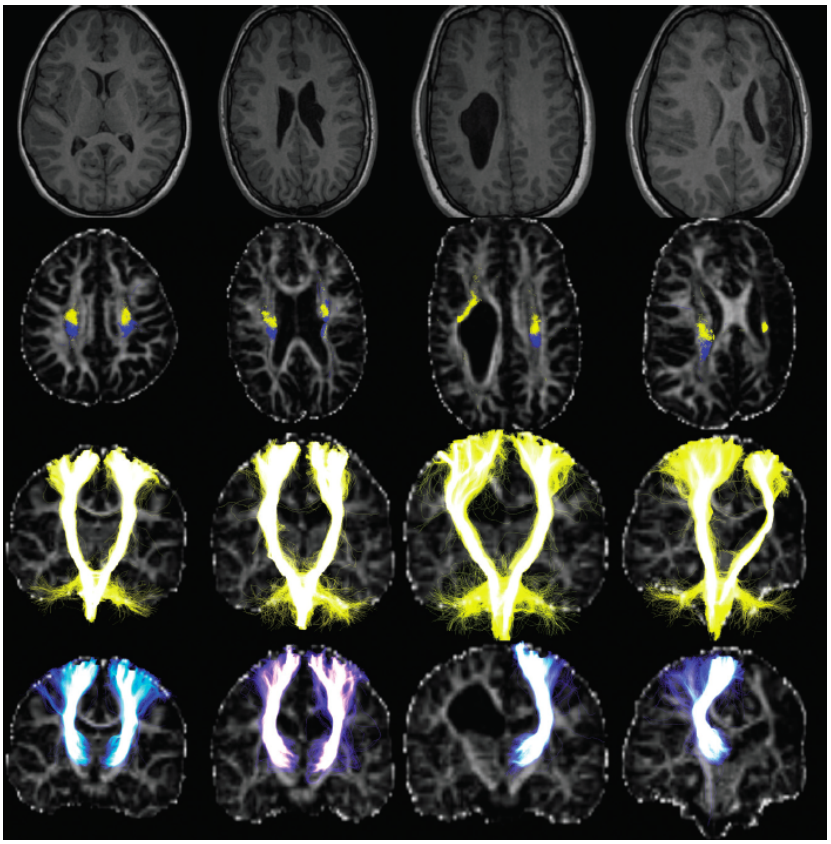

Fig. 3.8 – Tracking results of the CSTs (yellow) and the TRS (thalamic projections to the somatosensory cortex) (blue) in a healthy control (column 1) and 3 subjects with unilateral CP (columns 2– 4). Images, shown in radiologic orientation, include T1-weighted images (row 1) and tracts superimposed on FA maps in the axial section at the level of the upper corona radiata (row 2) and entire coronal projections (rows 3– 4). Subject on column 2 has a periventricular pseudocyst at the level of corona radiata, which causes local splits to the left TRS and left CST, which are seen to partly share locations, and dislocate the major branch of the left CST. Subject on column 3 has a large right WM lesion obstructing the anticipated courses of the TRS and the CST, making tracking of the TRS impossible and dislocating the right CST. Subject on column 4 had a left focal infarct with extensive damage to the entire left hemicranium and severe WM damage above the PLIC, which confined the left CST to a thin sliver of WM at the level of the corona radiata and made the left TRS nontrackable [30].

3.3 DTI studies of cerebral palsy

Different metrics are calculated by the DTI model (FA, RD, AD and MD). These metrics try to represent the fibers characteristics. First, the legitimacy of these metrics for children with CP is proven by the correlation with different motor evaluation tests. Afterwards, the metrics modifications due to this pathology are explained.

A significant correlation exists between FA in corticospinal tracts and Bayley motor score with HIE. The Bayley motor score is calculated by a series of developmental play tasks and allows to determine a developmental quotient (DQ) [33].
The gross motor scores (gross motor functions require whole body movement) are associated with FA and RD in the white matter [5].

The FA is lower in infants with white matter abnormalities who developed CP compared to those who have white matter abnormalities but who did not developed CP. The FA has lower value in different tracts including corpus callosum and CST [5].
In healthy children, an increase in the fiber volume, an increase in FA and a decrease in MD with the age is normally observed but this is absent in children with CP. The CST maturation is disrupted in these children, due to the perinatal injury that arrests normal CST development [3].
The RD is the diffusion perpendicular to the axonal direction and could be influenced by changes related to myelination and cellular proliferation in the axonal space [24].

The change in AD is less obvious, and varies between the authors:

- MD, AD and RD all showed significantly greater diffusivity in the lesioned CST. A greater AD in the lesioned CST reflects the increased diffusion parallel [24].
- Decrease in AD and diffusion corresponds to increased age [3]. As this normal development does not occur in children with CP, their AD is therefore higher than in control subjects.
- In a more general article, analyzing the axonal and myelin damage, it has been shown that axial diffusivity values were diminished in the beginning of the demyelination process and AD was not reduced during prolonged demyelination, in which axonal atrophy was evident [34].

The modification of the parameters is unclear and conclusions must therefore be interpreted with caution.

3.4 NODDI studies of cerebral palsy

As in the previous section, in this part, the NODDI metrics modifications due to CP are explained. Unfortunately, only one scientific paper was found in the literature, therefore the results must be interpreted with caution.

DTI is widely used to quantify white matter organization. The metrics given by DTI prove that microstructural properties of CST are relevant to understand movement impairment in children with CP. A reduction of the metrics is associated with structural integrity in the lesioned CST, but no specific differences in white matter microarchitecture have been established. There is a lack of biological specificity.
Therefore, NODDI can be used to provide more information on the CST microstructure. Intracellular volume fraction (ICVF) and orientation dispersion index (ODI) are two NODDI metrics that allow to reveal distinct properties of CST microstructure that are linked to motor function [24].

ICVF is better to distinguish white matter regions of interest between lesioned and non-lesioned hemispheres, compared to FA [24]. Indeed, studies on adults with stroke shown that FA is not as strong compared to NODDI model. The NODDI metrics could therefore complement FA as markers of white matter integrity [35].
Mean ICVF is significantly lower in lesioned CST corresponding to lower density fiber tracts.
No real difference in the mean of isotropic volume fraction (ISOVF) is observed. Therefore, the fiber density decrease is due to a decreased volume fraction of the axons and not due to a difference in CSF because there is no difference in the ISOVF [24].
Mean ODI is lower in lesioned CST, corresponding to a more coherent orientation. This suggests a more parallel fiber structure for the lesioned CST [24].

In the found article, an increase in AD is observed in lesioned CST but as explained in the previous section, the AD is contested. By combining the metrics of the two models, it is found that CP consequences include fewer barriers to diffusion along the axonal direction in lesioned CST, with more parallel (higher AD, lower ODI) but lower density (lower ICVF) fiber tracts [24].
The NODDI model completes the general metrics from the tensor model and allows to have more biological relevant information.

Chapter 4

Application

Now that all the necessary concepts have been defined, the application of the microstructural models on children with bilateral lesions can be analyzed. In the first part, the characteristics of the data are described. In the second part, the different pre-processing steps that were applied to improve the data quality are explained. In the third part, the pipeline that was used to isolate the CST on this pre-processed data is defined. In the fourth part, the framework to calculate the DTI and NODDI metrics on the CST is explained. Finally, the statistical tests used to analyze the microstructural metric changes are described.

4.1 Data

In this section, the subject characteristics are reported for the control and CP populations. Afterwards, the acquisition parameters are detailed. Finally, questions of behavioural surveys were asked to the children's parents to evaluate their mobility competences. A description of these behavioural questionnaire is included in the last part of this section.

4.1.1 Subjects

Two populations were scanned, 7 children with CP and 4 control subjects. The characteristics of these two populations are presented in this section. It has to be noticed that only 4 control subjects were taken into account in this work because 3 subjects with CP were rejected due to their images being too noisy. This decision is explained in more details in the pre-processing section.

Subjects with cerebral palsy

The subjects with CP have lesions on both hemispheres. The information about their type of lesions and their most affected hand are given in Table 4.1.
As explained before, early diagnostics of CP are difficult to make, by consequence, both diplegia and quadriplegia cases were considered in this work. The current diagnostic is reported in Table 4.1 with WMI corresponding to diplegia and GMI to quadriplegia, but it could evolve with age.

Table 4.1 – Information about CP subjects: Age at time of MRI acquisition, lesion type (WMI=White mater injury, GMI=Gray mater injury and PVL= periventricular lesion) and the most affected hand.

Subject	**Age [year]**	**Lesion Type**	**More Affected Hand**
1	3	WMI/PVL	RIGHT
2	2	WMI/PVL	LEFT
3	3	WMI/PVL	RIGHT
4	3	GMI	LEFT
5	4	GMI	LEFT
6	1	WMI/PVL	LEFT
7	4	GMI	RIGHT

Control subjects

The age and the handedness of the control subjects are described on Table 4.2

Table 4.2 – Information about control subjects: Age at time of MRI acquisition and handedness.

Subject	**Age[year]**	**Handedness**
8	9	RIGHT
9	9	RIGHT
10	10	RIGHT
11	8	RIGHT

4.1.2 Acquisition

The MRI scanner used is a $SIGNA^{TM}$ Premier 3 Tesla (GE Healthcare, Chicago, USA) and the slices were acquired with simultaneous multi-slices (SMS) sequences.

A typical acquisition is described by three parameters: δ, Δ and G.
The parameters for the sequence used for children with CP are $\delta = 19644[\mu s]$ and $\Delta = 31492[\mu s]$, and for the control sequence are $\delta = 23824[\mu s]$ and $\Delta = 35660[\mu s]$. More details about the sub-timing is shown in Appendix B. The sequences used for children with CP are multishell sequences with three different shells (b-values(G)=1000, 2000, 3000) composed of 128 directions (respectively, 64, 32 and 32) and five images with a b-value of 0. For the control subjects, a supplementary shell with a b-value of 5000 with 32 directions was added to the sequence. This second sequence is composed of 160 directions and seven images with b0. The sequence details are shown in Appendix I.1.

To limit the movement, all the children with CP were scanned while sleeping except subjects 5 and 7 that were in front of a cartoon. The control subjects were scanned with their eyes closed.

4.1.3 Behavioural analysis

Two behavioural surveys were submitted to the parents of children with CP. These surveys try to represent the children's motor capacity in their daily life.

The first one is Pediatric Evaluation of Disability Inventory-Computer Adaptive Test (PEDI-CAT). It is realized for two categories: the mobility domain, based on basic motor skills, and the daily activities domain, composed of self-care activities and specific test items. For each of them it is asked to the parents if the activity is easy, difficult or impossible to realize for their child. Scores for the daily life and the mobility are obtained in percentages. This questionnaire is valid for children from birth until the age of 20 years [36].

The second survey is ACTIVLIM-CP and is composed of questions on more complex movements of daily life, involving both superior and inferior limbs. It gives a measure of the global activity performance in everyday life of children with CP. The Rasch model is used for this survey analysis, allowing more non-replied questions. The initial score is in logit. Since this unit of measurement is not really intuitive, it is transformed in percentages. This questionnaire is valid for children with CP from 2 to 18 years old [37].

The test results are shown in Table 4.3.

Table 4.3 – Results of the behavioural analyse for the children with CP.

Subject	**PEDI DA** [%]	**PEDI Mob** [%]	**ACTIVLIM** [**Logit**]	**ACTIVLIM** [%]
1	50	56	0.047	50
2	52	52	0.172	51
3	49	41	0.933	43
5	51	60	0.475	46

4.2 Pre-processing

Before applying the different models, the data needed to be pre-processed. The first step was the motion correction. Because of some problems with the MD results in DTI, a more robust technique was used: DKI. Unfortunately, this model was not sufficient for the children with CP. To solve this issue, the DTI was reduced to one-shell data.

4.2.1 Motion correction

Before analyzing the images, a pre-processing step of movement correction needed to be applied. This step was crucial, because the subjects are children who move considerably.

All the different steps, from the initial data to the extraction of the different metrics in the different software applications, are explained in Appendix A.

The correction was done with **FSL** [16] with the following commands:

- `eddy_correct` *DTI_init.nii* *DTI_after_correct.nii* *reference_num*

  This first command line aligns all the volume of the initial 4D-DTI to give a DTI corrected for the movement. The reference number corresponds to a volume without diffusion (b0), in our case: 0.

- `fdt_rotate_bvecs` *init.bvec* *rotated.bvec* *eddy_correct_output.ecclog*

  The second command line adjusts the b-vector to be correlated with the DTI corrected for the movement. This is done based on the output file ecclog (transformation matrix of aligned volumes) given by the first command line. The b-value does not change for the motion correction and therefore it is not needed for the FSL correction.

The result of this motion correction is shown in Fig. 4.1 for a control subject and in Fig. 4.2 for a children with CP. The choice of FSL to correct the movement is explained in Appendix C.

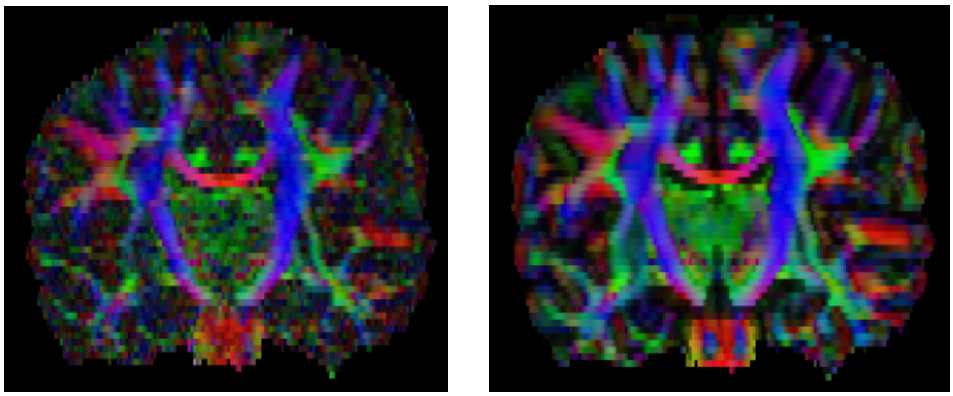

Fig. 4.1 – Comparison of DTI before (on the left) and after (on the right) FSL motion correction for subject 8 (control subject).

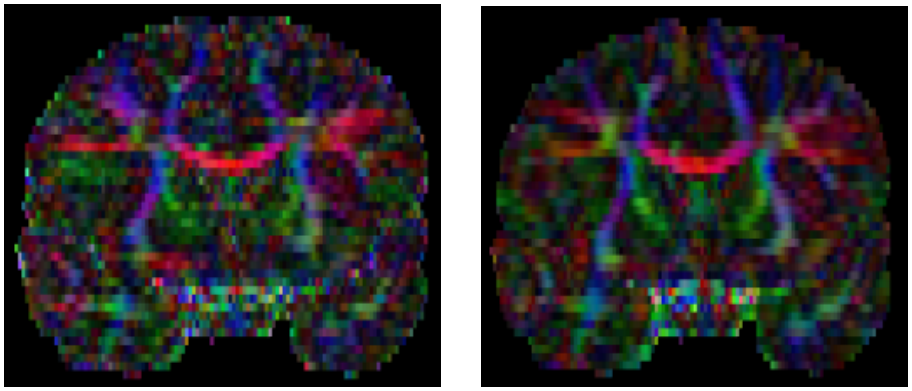

Fig. 4.2 – Comparison of DTI before (on the left) and after (on the right) FSL motion correction for subject 2 (subject with CP).

Subject rejection

Three of the seven subjects with CP were rejected because even after motion correction, the DTI data was too noisy.

Subject 7 is chosen as example in Fig. D.3 and the two other subjects are shown in the Appendix D. The images are display with **ExploreDTI** [38].

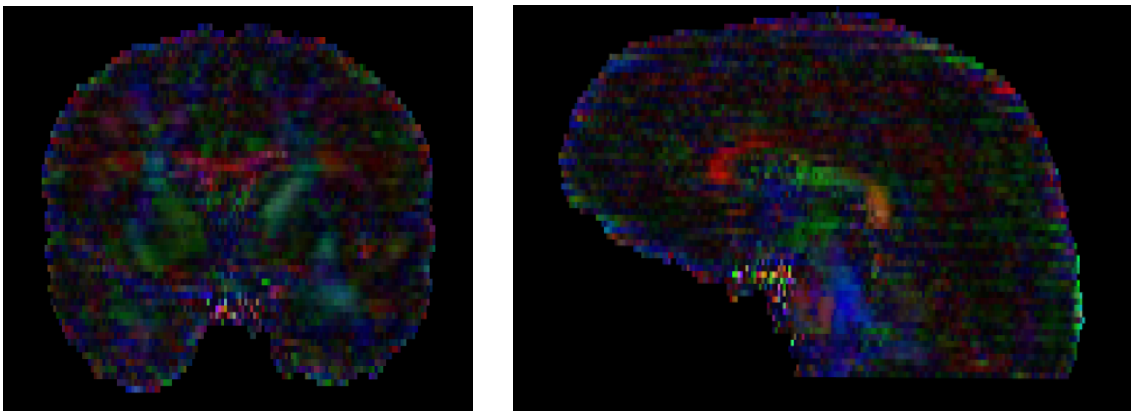

Fig. 4.3 – DTI of subject 7 after motion correction.

For the rest of this work, only 4 children with CP were considered.

4.2.2 Mean diffusivity issue

A non-correct MD was detected when it was calculated with a DTI model. Without a correct MD, CSD tracking is not working in ExploreDTI. For this reason, different modifications were done: the DKI model was used and the DTI was reduced to only one shell.

Diffusion Kurtosis Imaging

The MD calculated by DTI on ExploreDTI did not match expectation (the same problem was observed with FSL as shown in Fig. E.6): the CSF had a low MD. The CSF is supposed to have a high MD because it has an MD similar to water.

To solve this problem, a more robust model was used: DKI in ExploreDTI. The MD calculated by DKI corresponds to an expected MD: low in white matter and high in CSF (Fig. 4.4).

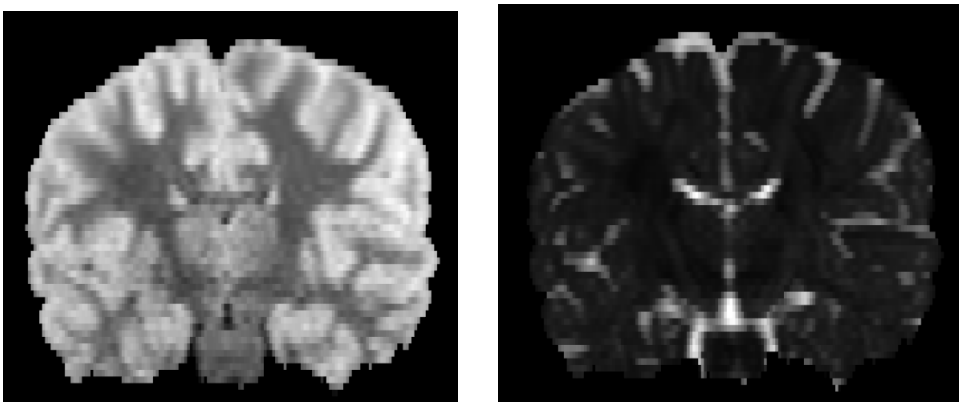

Fig. 4.4 – MD calculated by DTI on the left and by DKI on the right on subject 8 (control).

One-shell DTI reduction

The DKI was also applied on the subjects with CP but the tracking algorithm was not working. The comparison between the MD with DTI and DKI for children with CP is shown in Fig. 4.5 and reflects an improvement in the MD estimation for the DKI. But the comparison between the MD calculated by DKI of children with CP (Fig. 4.5 right) and one of control subjects (Fig. 4.4 right) reveals that MD is higher in the white matter of children with CP. This could explained the tracking issue. Another reason could be the poor quality of images.

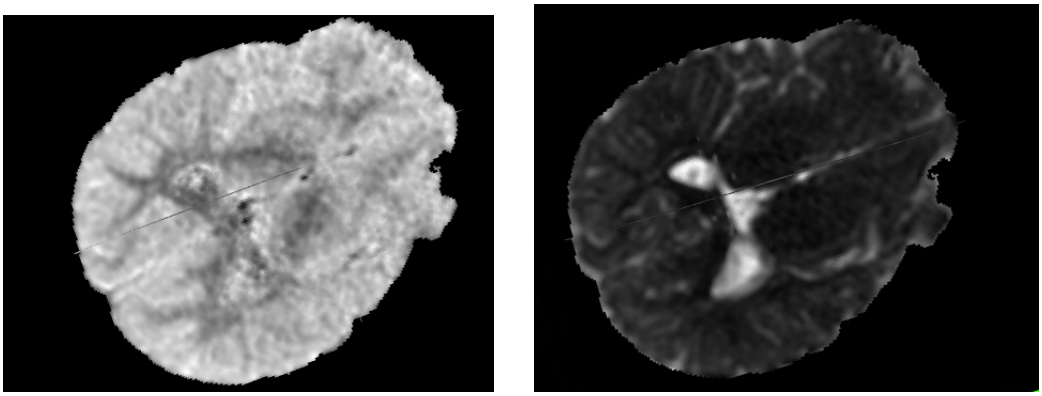

Fig. 4.5 – MD calculated by DTI on the left and by DKI on the right for subject 1 (CP).

To solve this issue, another technique needed to be applied for the subjects with CP. The DTI was reduced to only one shell. To achieve this, the following command line of FSL was used:

`fslroi` *dti_init.nii* *dti_split.nii* 0 65

0 and 65 correspond to the first and last volumes of the reduced DTI.

4.3 Tracking

After the pre-processing, the images were analyzed. The first step was to identify the motor CST. It was on this specific region that all the metrics (DTI and NODDI) were calculated.
This study focuses on the motor CST to only analyze the impact of CP on the motor system. Indeed, it was explained in Section 3.2 that the somatosensory function also affects the motor function, but this tract was not analyzed. The optical projections are also impacted by the CP but their tracts are more complicated to be identified, therefore a better knowledge of the neuroanatomy is needed.

The CST isolation was crucial and was a major challenge of this thesis. It needed to be precise to only keep the CST and not reduce the selected fibers too much. By consequence, finding a software able to help in this task was fundamental. The brain structure of children with CP being modified, a visual software was needed. The structure of the brain being so different from one subject to another, only a manual drawing of the ROI was possible. This difficulty is represented in Fig. 4.6. Indeed in this Figure, the structure of the control brain is clear, the sulcus appear clearly, in opposition to the brain with CP where the brain structure is difficult to identify.
This section describe the pipeline used to isolate the CST in severely-deformed infant brain. Drawing the ROI was the first step of the tracking. Afterwards, deterministic and probabilistic methods were compared. Finally, once the tract was identified, it was co-registered with the anatomical image to validate its position.

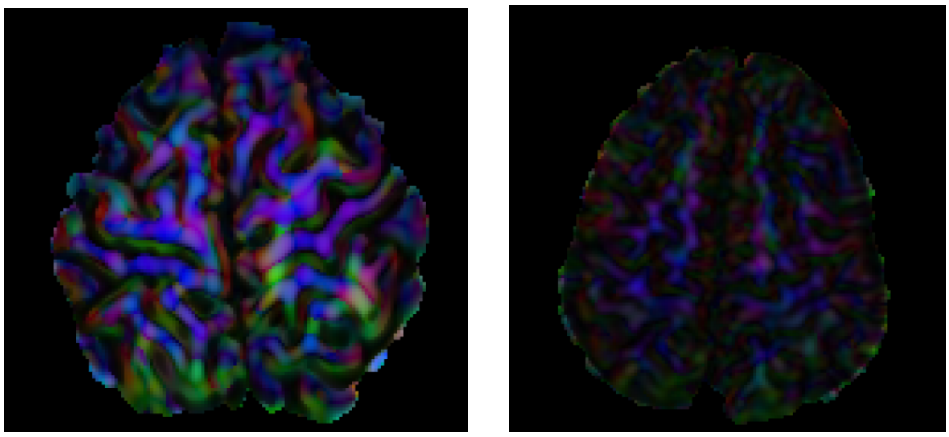

Fig. 4.6 – Comparison of brain structure between a control subject (subject 8 on the left) and a child with CP (subject 2 on the right).

4.3.1 Region of interest

To create a CST, different ROI needed to be defined. Two ROI were defined in Section 3.2 to be able to isolate the CST: one at the level of the posterior limb of the internal capsule (PLIC) (Fig. 3.6) and the cerebral peduncles; and a second one in the primary cortex.

To draw the first ROI, different steps were needed. Firstly, the position of a transverse plane was determined by a plane passing through the emergence of the middle cerebellar peduncle. Its anatomical position is shown in Fig. 3.5 and the position of the plane on ExploreDTI for the subject 2 in Fig. 4.7.

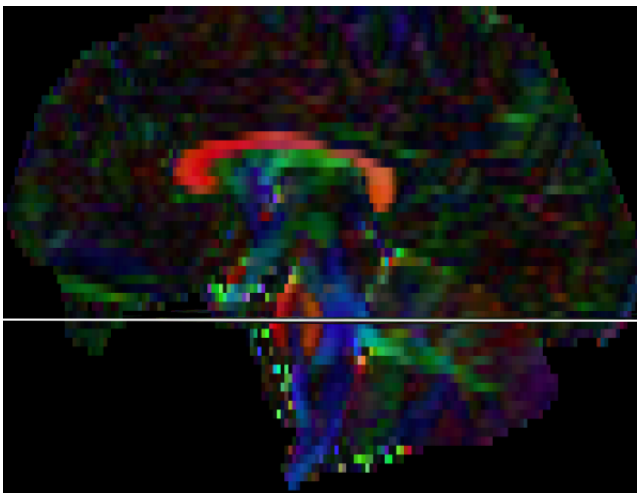

Fig. 4.7 – Position of the z-plane at the level of the middle cerebellar peduncle (shown on y-plane) for the subject 2.

Secondly, on this transverse plane, in the brainstem, four blue zones were highlighted: the two (left and right) posterior ones corresponding to the lemniscus medialis and the two anterior ones corresponding to the CST (Fig. 4.8).

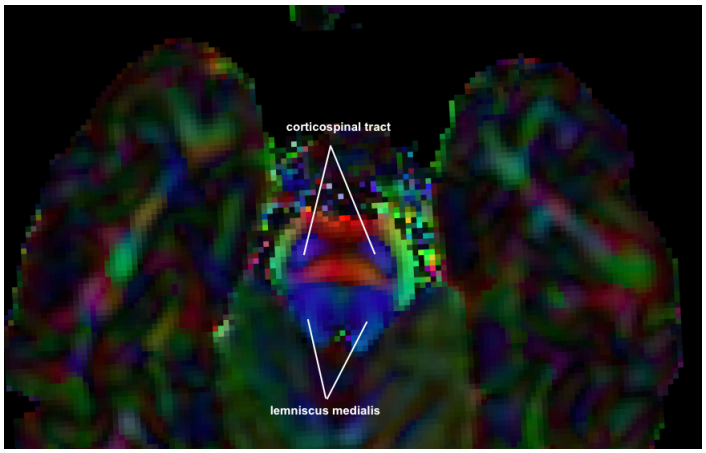

Fig. 4.8 – Highlight of the CST on the axial plan of the subject 2.

The left or right blue zones corresponding to the CST were circled and defined as SEED-ROI.

The second seed was drawn in the motor cortex (anatomical description in Fig. 3.2 and drawing on a subject in Fig. 4.9) in the same hemisphere as the first ROI, to be sure to only keep the motor part of the CST.

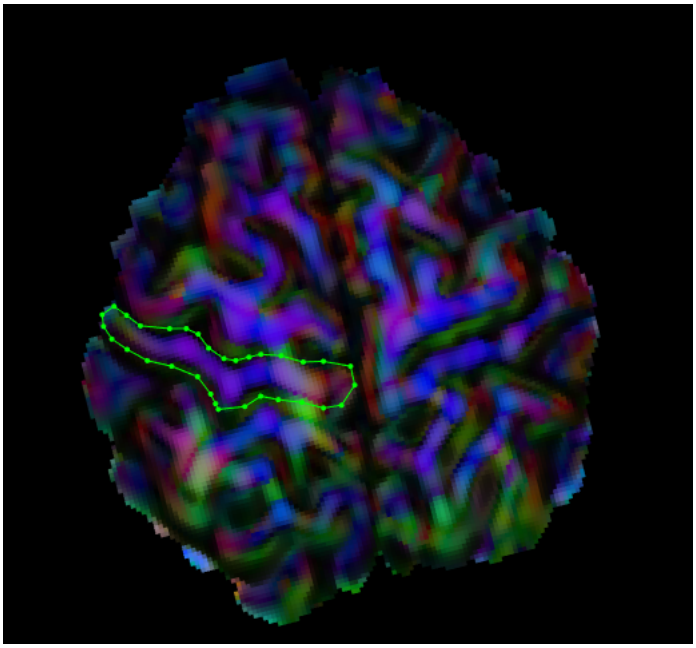

Fig. 4.9 – Drawing of a ROI in the motor cortex of subject 8.

4.3.2 Tracking methods

The tracking can be done using two techniques: DTI or CSD tracking. The parameters used for those two methods are given, respectively, in Table 4.4 and Table 4.5.

Table 4.4 – Parameters of DTI tracking.

Fiber length [mm]	[50 1000]
Angle threshold [°]	30
Step size [mm]	1

Table 4.5 – Parameters of CSD tracking.

Seed FA threshold	0.2
Fiber length [mm]	[50 1000]
Angle threshold [°]	30
Step size	1
Interpolation method	Linear

The major differences between these two methods are the tensors. In DTI, only one tensor is defined by voxel compared to CSD were multiple tensors are allowed. The glyph objects of the tensor are shown in Fig. 4.10 and Fig. 4.11.

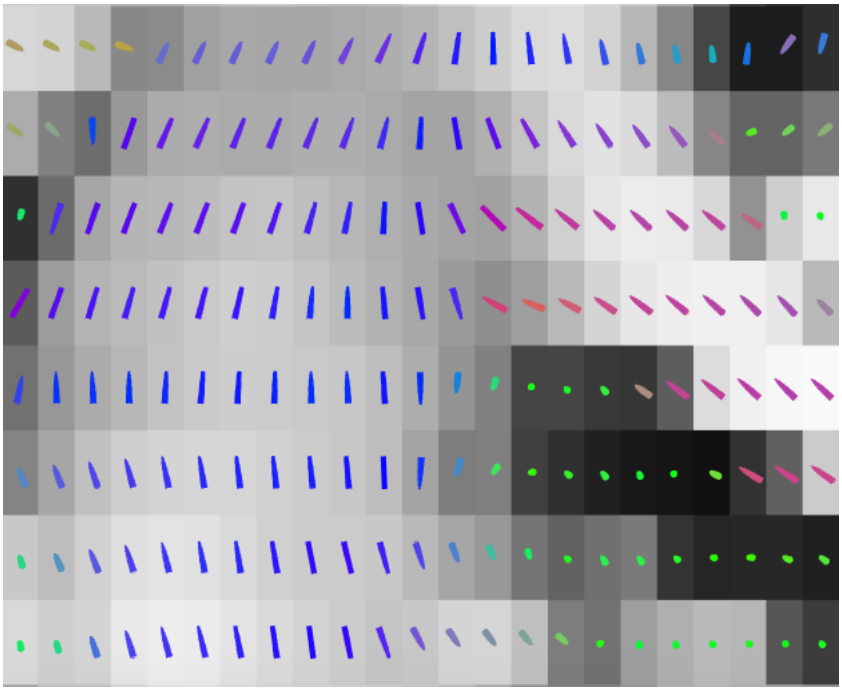

Fig. 4.10 – The glyph objects of the tensor DTI on subject 8.

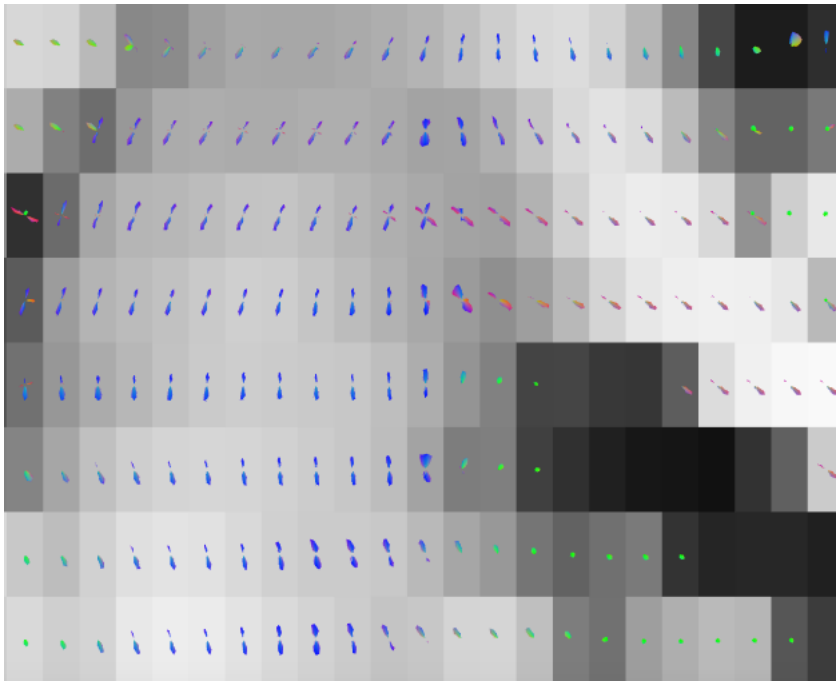

Fig. 4.11 – The glyph objects of the tensor CSD on subject 8.

The comparison of tracking results is shown in Fig. 4.12. These tracks were done only with a seed in the brain stem to have a global vision for the comparison. In these Figures, it is clear that the CSD tracking method gives better results. This method was chosen to track and defined CST in the following analyzes.

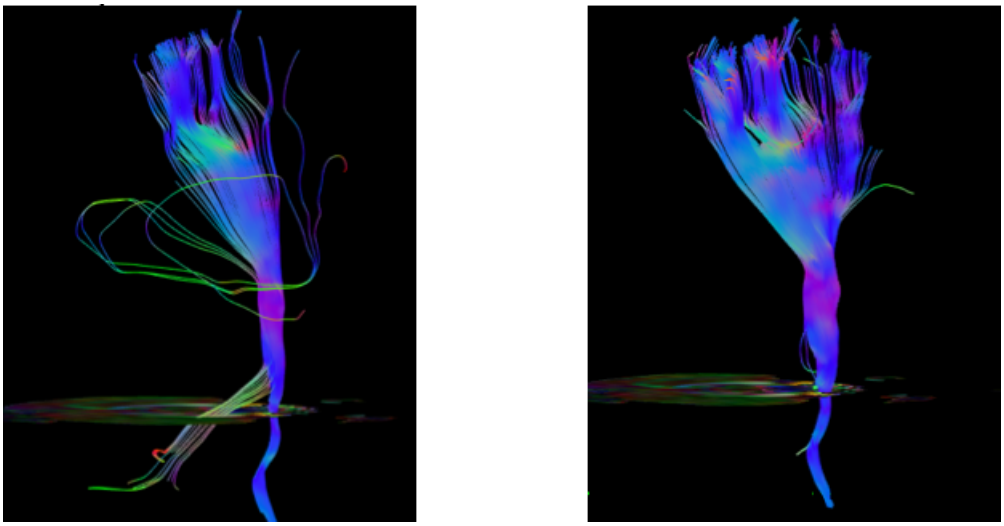

Fig. 4.12 – Comparison of tracking methods: DTI on the left and CSD on the right.

The result of the tracking with CSD method and the two ROI defined in the previous section is shown in Fig. 4.13.

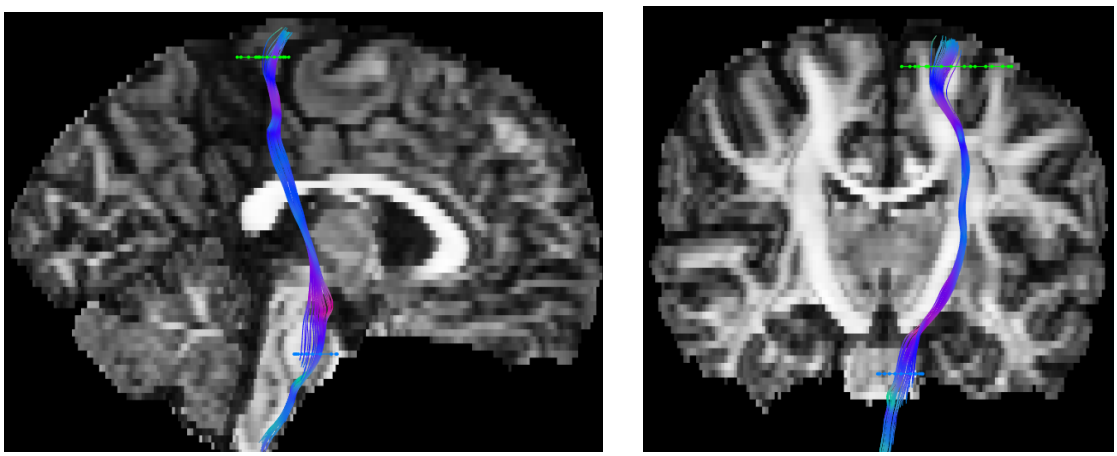

Fig. 4.13 – Tracking of CST with CSD method and two ROI on subject 8. The tract is displayed on the FA map.

4.3.3 Co-registration

To have a better view of the anatomical position of the CST, the tracts calculated with the CSD method were displayed on the anatomical MRI.

Firstly, the structural images include the skull and other tissues that do not belong to the brain. For this reason, it was necessary to extract the voxels related just to the brain from the initial anatomical images. In the images, a big portion of the neck is present: before performing the brain extraction, the images were manually cropped using `FSLeyes`.
After this first step, the `BET` function of FSL can be used to extract the brain. The results of these two steps is shown in Fig. 4.14.

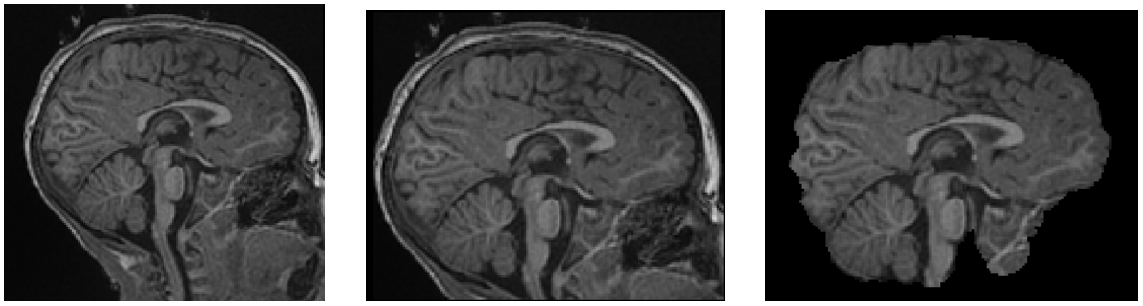

Fig. 4.14 – Brain extraction using FSL on subject 2. On the left, the initial anatomical MRI, in the middle, the anatomical MRI with cropped neck and on the right, the extracted brain.

Secondly, the registration between the anatomical image (high resolution) and the diffusion image (low resolution) was done with `FLIRT` function of FSL. This function gives the DTI on the anatomical space and the matrix of transformation that was applied to the initial DTI to reach the registered DTI with the anatomical image.

Thirdly, this transformation matrix was applied to the tract using the following command line of FSL:
`flirt -in` *Tract_mask.nii* `-ref` *ANAT.nii.gz* `-applyxfm -init` *matrix.mat* `-out` *Tract_mask_reg.nii*

With the tract in the anatomical space, the anatomical image and the tract can be displayed together on `FSLeyes` as shown in Fig. 4.15.

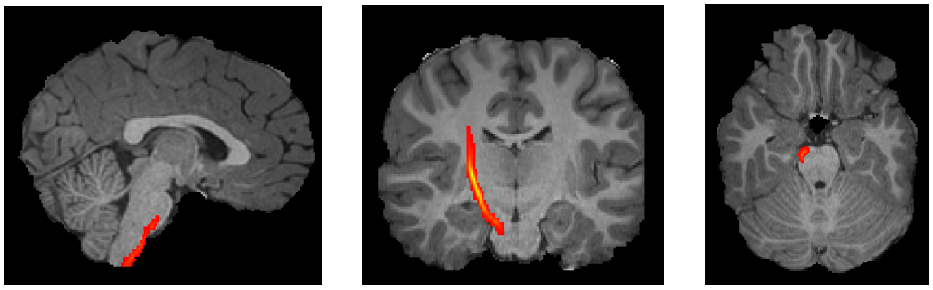

Fig. 4.15 – CST calculated with ExploreDTI plotted on the anatomical image on FSLeyes for the subject 8.

4.4 Statistical analysis

Once the CST isolated, the different DTI and NODDI metrics were analyzed only on this region. Afterwards, statistical analysis were performed with these metrics. Three main objectives were pursued by this analysis: first, to compare the control population and the CP population; afterwards, to compare the left and the right hemispheres for both populations; finally, to analyze the correlation between the microstructural metrics and the behavioural scores.

4.4.1 DTI metrics

Different programs are able to generate map of DTI metrics. As the CST was defined with ExploreDTI, this program has been chosen for the convenience of keeping the same software.

On the tract defined by CSD tracking, different metrics were calculated by ExploreDTI: FA, MD, length, L1, L2 and L3. For all these metrics different, statistical values were given: average, standard deviation, standard error, number of voxel, 95% interval, median and [25, 75] percentiles. A text file were extracted with all the information.
Among all this information, the mean and the standard deviation (SD) of FA and MD were kept. RD, AD (mean and SD) were calculated by **Matlab** (Appendix H) using the eigenvalue (cfr equation in Section 2.1.1).

4.4.2 NODDI metrics

To calculate the metrics derived from the NODDI model (ODI, ISOVF and ICVF), the software **Quantitative Imaging Toolkit (QIT)** [39] has been used.

A first pre-processing was done: transform the DTI to the Neurological view. To have the tensor correctly aligned, the neurological convention needed to be imposed. To achieve that, the following FSL command was used:
`fslorient -forceneurological` *nifti_neuro.nii*

To reduce the computation time, a brain mask was calculated with the FSL `BET` function (Fig. 4.16).

Fig. 4.16 – Mask creation using FSL on subject 2.

With the bvec, bval, the DTI in the neurological convention and the mask, the map of NODDI metrics were calculated with QIT and after were uploaded in **Python**. The CST mask created with CSD in Explore DTI was also uploaded in Python. The mean and the SD of each metric (ODI, ISOVF and ICVF) were calculated on the CST mask region. The Python code is shown in Appendix H.

4.4.3 Statistical tests

Two variables were compared with statistical tests: the mean and the SD. The comparisons were made between the two populations: control subjects and children with CP; and between the two hemispheres.
Afterwards, correlations were calculated between the microstructural metrics and the behavioural scores.

For the statistical analysis, the non-dominant hand of control subjects and the more affected hand of children with CP are named together as non-dominant (ND) hand; and the dominant hand of control and the less affected hand of CP are named as dominant(D) hand. The hemisphere in the opposite side of the dominant hand is called dominant hemisphere and vice versa for the non-dominant hemisphere.

The different analyses achieved are:

- parametric: the data is supposed to follow normal distributions;
- 2-sided test: the mean and variance are equals or different:
  H0: $1 = 2$ and Ha: $1 \neq 2$;
- non-paired for the comparison of the control population and population with CP and paired for the comparison of the two hemispheres;

Different analyzes were performed with **R** [40]:

- T-tests were performed to compare the means and the standard deviations:
  - between the two populations (control subjects and children with CP): non paired T-tests were performed using the following command line:
    `t.test`(*data_table_name*$*variable_to_compare*~Palsy_categorisation, `mu`=0, `alt`="two.sided", `paired`=F, `conf.level`=0.95)
  - between the two hemispheres (dominant and non-dominant): paired T-tests were performed for the two populations separately using the following command line:
    `t.test`(*data_CONTorCP*$*variable_D*, *data_CONTorCP*$*variable_ND*, `mu`=0, `alt`="two.sided", `paired`=T, `conf.level`=0.95)
- Correlations were also calculated:
  - between the behavioural data and each microstructure metric for the children with CP, using the following command line:
    `cor`(*data_CP*$*variable_microstructure*, *data_CP*$*variable_behaviour*)

Chapter 5

Results and discussions of statistical analysis

After measuring all the information from ExploreDTI and QIT, the different comparison tests explained in Section 4.4.3 were realized for the following metrics: FA, MD, AD, RD, ODI, ISOVF and ICVF. The results of these tests are explained in this section.
The objective of this thesis is to investigate the microstructural brain changes in the CST, due to CP with bilateral lesions. The comparison between the control subjects and the children with CP was performed to highlight these changes.
Afterward, the relation between the two hemispheres was analyzed. Even if the children with CP have bilateral lesions, one side of the body is more affected (Table 4.1). The comparison of hemispheres was investigated to find the link between this functional asymmetry and the CST structure.
Finally, the behavioural surveys results were evaluated to find a correlation between the microstructural metrics and the behavioural scores.

Each comparison started with a visual analysis with boxplots, first for the DTI metrics and afterwards for the NODDI metrics. These visual results were confirmed by performing t-tests.

5.1 Comparison between the two populations

The first analysis compared the control subjects to the children with CP, to understand the structural modifications of CST due to the pathology. The mean and the SD of the DTI and NODDI metrics were compared.

5.1.1 Mean

Comparison of the mean for all the DTI (Fig. 5.1) and NODDI (Fig. 5.2) metrics was performed between the healthy control subjects (HC) and the children with CP (CP). The results of the achieved t-tests are shown in Table 5.1. The mean comparison of the different parameters highlighted the metric modifications in the

CST of children with CP; these parameter variations being associated with biological structure modifications.

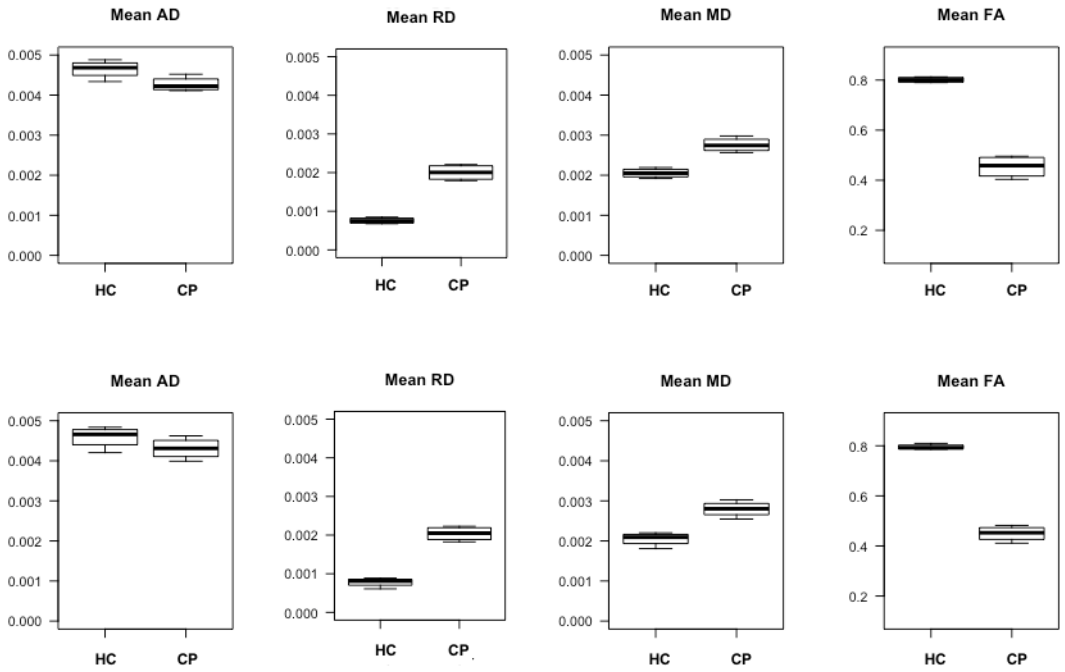

Fig. 5.1 – Boxplots comparing the different DTI metrics between healthy control subjects (HC) and children with CP (CP) for the dominant hemisphere (on the top) and non-dominant hemisphere (on the bottom).

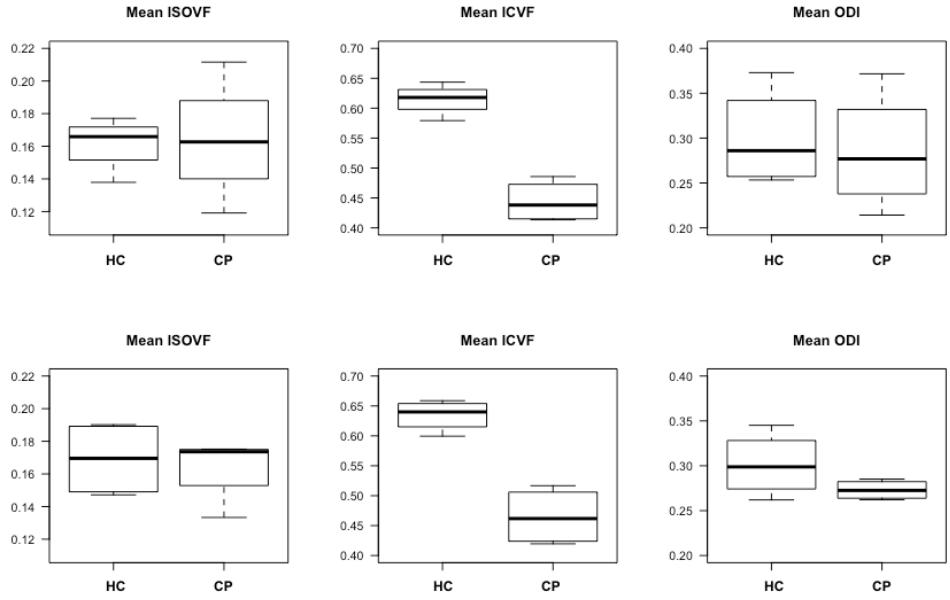

Fig. 5.2 – Boxplots comparing the different NODDI metrics between healthy control subjects (HC) and children with CP (CP) for the dominant hemisphere (on the top) and non-dominant hemisphere (on the bottom).

Table 5.1 – T-test results for the comparison of the different NODDI and DTI metrics between control subjects and children with CP, with the dominant hemisphere (D) on the top and the non-dominant hemisphere (ND) on the bottom. In green: the p-values inferior to 0.05 (significant level).

T-test Mean HC/CP D				
Mean_AD	t = 2.5797	df = 5.7262	p-value =	0.0436
Mean_RD	t = -11.334	df = 3.8446	p-value =	0.0004282
Mean_MD	t = -6.5109	df = 5.2073	p-value =	0.001094
Mean_FA	t = 15.166	df = 3.3728	p-value =	0.0003199
Mean_ISOVF	t = -0.11235	df = 4.1319	p-value =	0.9158
Mean_ICVF	t = 7.7759	df = 5.5917	p-value =	0.0003347
Mean_ODI	t = 0.34034	df = 5.8132	p-value =	0.7456

T-test Mean HC/CP ND				
Mean_AD	t = 1.4684	df = 5.9951	p-value =	0.1924
Mean_RD	t = -11.402	df = 5.1083	p-value =	7.934e-05
Mean_MD	t = -5.6805	df = 5.8689	p-value =	0.001383
Mean_FA	t = 21.277	df = 3.6909	p-value =	5.36e-05
Mean_ISOVF	t = 0.33472	df = 5.9042	p-value =	0.7494
Mean_ICVF	t = 6.1735	df = 4.6176	p-value =	0.00215
Mean_ODI	t = 1.5111	df = 3.569	p-value =	0.2136

In Fig. 5.1, high AD and low RD were observed. This result is coherent because the analyzed region is a white matter tract and is by consequence composed of fibers which have a principal diffusion direction along the axons. MD is composed of both diffusion directions and has, by consequence, a value between AD and RD.

High FA, which correspond to an ellipsoid model and to a high anisotropy, was observed for the control subjects. The decrease of this metric for the children with CP is analyzed in the next paragraph.

The observed results for the comparison between control subject and children with CP are coherent with the results of literature presented in Chapter 3 (Merhar et al, 2020; Papadelis et al, 2019; Nemanich et al, 2019).
A lower value of FA and a higher value of MD were observed in children with CP in comparison to the control subjects. This is explained by the absence of the maturation process in the CST for both hemispheres compared with normal development where the maturation continues to CST development during childhood [2].

Significantly higher RD in children with CP reflects the increased freedom of diffusion in the white matter perpendicularly to the main fibers direction and may reflect a degree of demyelination [41].

The ICVF metric was lower in children with CP which could be attributed to lower density of fiber tracts. No difference in ISOVF was observed, which is coherent with the non-decrease of CSF in CP. The fiber density decrease is therefore due to a decreased volume fraction of the axons and not due to a difference in CSF. But the ISOVF variation between the subjects is important, this result must be interpreted with caution.

In the ODI boxplots, a small decrease in CP was observed, but this difference is not significant as it was not validated by the t-test, due to the high variation between the subjects. No conclusion can therefore be drawn on the ODI metrics.

A decrease in AD was observed for the subjects with CP in the boxplots. The axial diffusivity values being reduced at the beginning of the demyelination process [34], it could explain the observed decrease. This result was confirmed by the t-test only for the dominant hemisphere.
As explained in Chapter 3, the results for AD are quite diverse in the literature and the same diversity was observed in this analysis.

In conclusion, lower values of FA and ICVF, and higher values of MD and RD in children with CP indicate that the CST is composed of a lower axonal density and a lack of myelin.

5.1.2 Standard Deviation

Comparisons of the SD for all the DTI (Fig. 5.3) and NODDI (Fig. 5.4) metrics were performed between the control population and the population with CP. The results of the realized t-tests are shown in Table 5.2.

The analysis of SD was realized to investigate the variation of the different parameters within the CST.

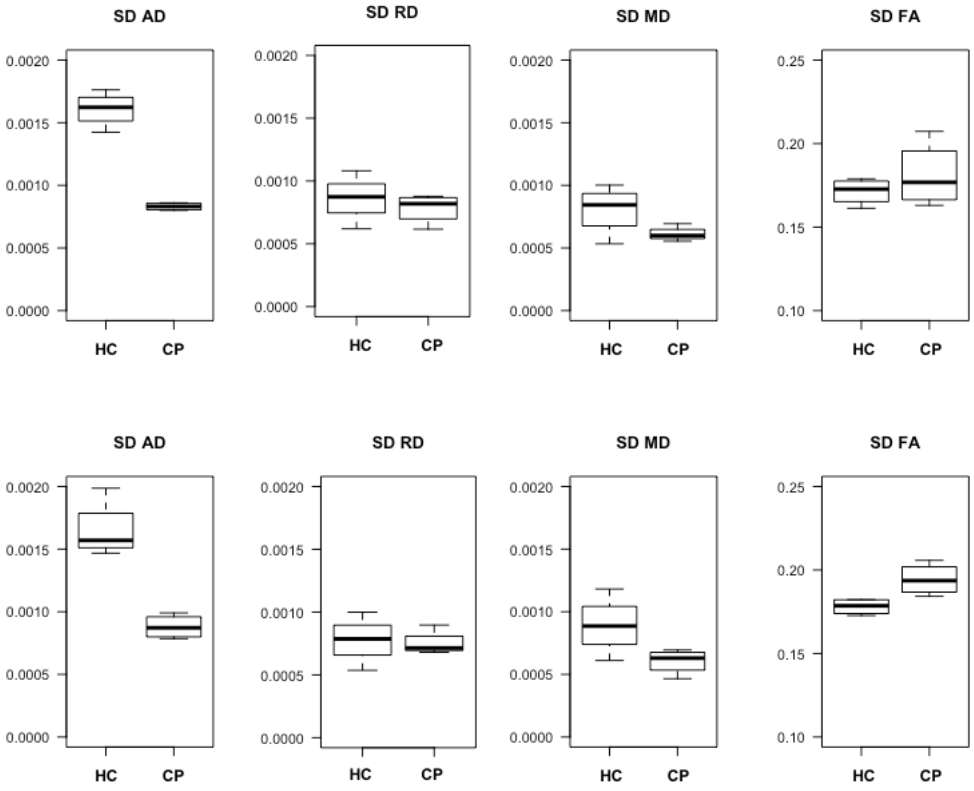

Fig. 5.3 – Boxplots comparing SD of the different DTI metrics between healthy control subjects (HC) and children with CP (CP) for the dominant hemisphere (on the top) and non-dominant hemisphere (on the bottom).

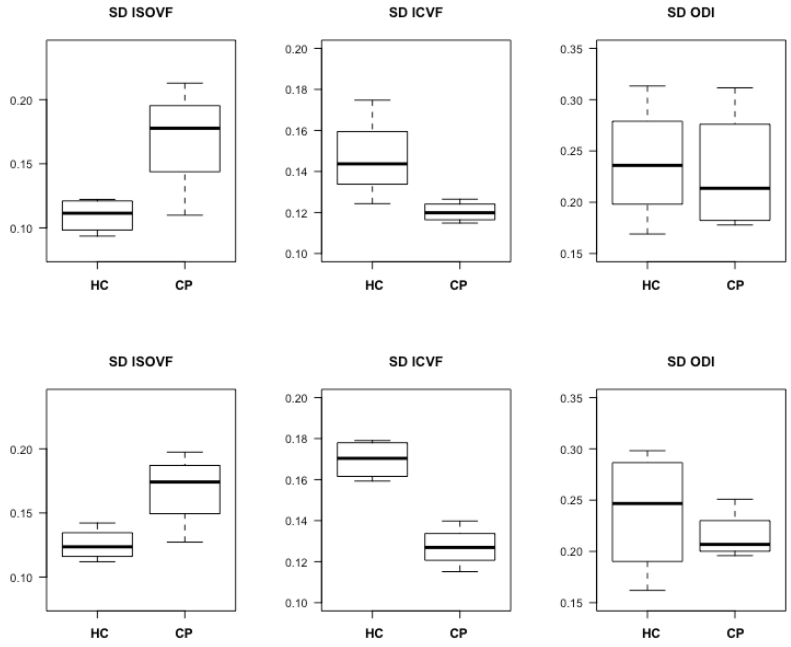

Fig. 5.4 – Boxplots comparing SD of the different NODDI metrics between healthy control subjects (HC) and children with CP (CP) for the dominant hemisphere (on the top) and non-dominant hemisphere (on the bottom).

Table 5.2 – T-test results for the comparison of the standard deviation of the different NODDI and DTI metrics between healthy control (HC) subjects and children with CP (CP), with the dominant hemisphere (D) on the top and the non-dominant hemisphere (ND) on the bottom. In green: the p-values inferior to 0.05 (significant level).

T-test SD HC/CP D				
SD_AD	t = 10.858	df = 3.2708	p-value=	0.001122
SD_RD	t = 0.2411	df = 4.5122	p-value=	0.82
SD_MD	t = 1.8849	df = 3.533	p-value=	0.1419
SD_FA	t = -0.90725	df = 3.9501	p-value=	0.4162
SD_ISOVF	t = -2.6488	df = 3.6005	p-value=	0.06364
SD_ICVF	t = 2.4546	df = 3.3437	p-value=	0.08256
SD_ODI	t = 0.21977	df = 5.9927	p-value=	0.8333

T-test SD HC/CP ND				
SD_AD	t = 6.1476	df = 4.0216	p-value=	0.003489
SD_RD	t = 0.70709	df = 5.0523	p-value=	0.5108
SD_MD	t = 2.2497	df = 4.0706	p-value=	0.08651
SD_FA	t = -3.0446	df = 4.4724	p-value=	0.03305
SD_ISOVF	t = -2.6668	df = 4.0866	p-value=	0.05476
SD_ICVF	t = 6.0823	df = 5.9906	p-value=	0.0009031
SD_ODI	t = 0.70929	df = 3.9426	p-value=	0.5178

The differences observed in the boxplots were not validated by the t-test except for AD. The t-test results for ICVF and FA also have a p-value inferior to 0.05, but these results were only observed in one hemisphere and by consequence further analysis could be done to confirm it.

A significant difference of AD SD was observed in both hemispheres, with a lower AD SD in children with CP than in the control subjects. This means that the AD is more constant in the CST of children with CP. The results of AD mean are quite diverse in the literature and no complementary conclusion were draw in the previous section analysing the mean comparison between the two populations. By consequence, the SD AD result must be interpreted with caution.

In conclusion, no significant variation within the CST between the two populations were found.

5.2 Comparison between the two hemispheres

After the comparison of the two populations, the analysis of the two hemispheres was investigated. Indeed, as the children have lesions in both hemispheres, the relation between the two may be affected. The comparison is made for the control subjects and children with CP for the DTI (Fig. 5.5) and NODDI (Fig. 5.7) metrics. The difference for the DTI metrics are difficult to observe in Fig. 5.5 due to the fixed scale, therefore boxplots with adapted scales to each metric are shown in Fig. 5.6. The results of the realized t-tests are shown in Table 5.3.

The comparison between the two hemispheres, should not give any significant difference for the control subjects. This comparison was achieved as comparison reference for the children with CP. Even if these children have bilateral lesions, their mobility is more affected in one side which is defined in Table 4.1. The comparison of hemispheres is investigated to find the link between this functional asymmetry and the CST structure.

Bearing in mind that some brain functions are lateralized, the side of the affected hemisphere influences the modification of the CST. The comparison between the two hemispheres should be analyzed separately for the left and right affected hemispheres. Unfortunately, due to the low number of subjects (four for each population), they were analyzed together.

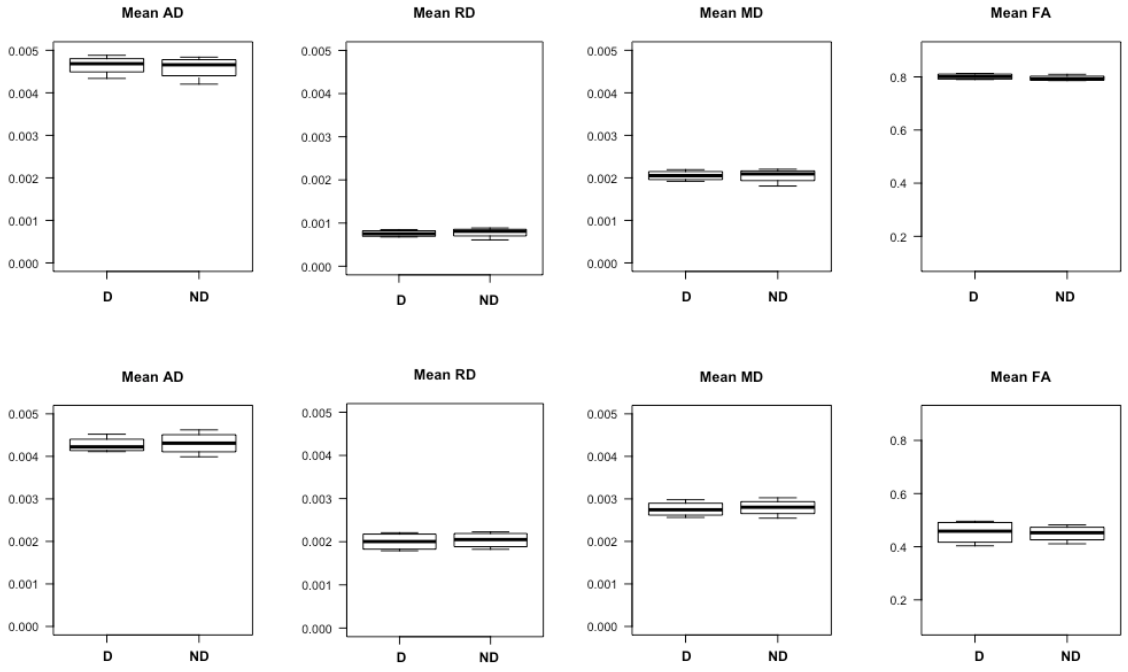

Fig. 5.5 – Boxplots comparing the mean of the different DTI metrics between the two hemispheres (dominant (D) vs non-dominant (ND)) for control subjects (on the top) and children with CP (on the bottom).

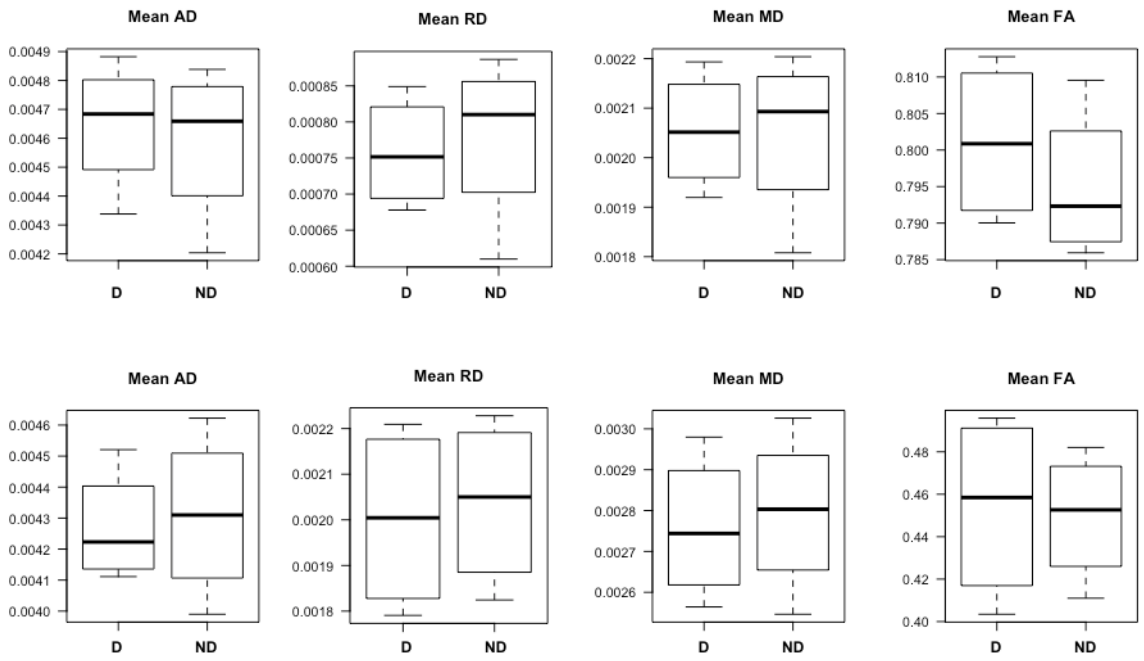

Fig. 5.6 – Boxplots comparing the mean of the different DTI metrics between the two hemispheres (dominant (D) vs non-dominant (ND)) for control subjects (on the top) and children with CP (on the bottom), with adapted scales to each boxplot.

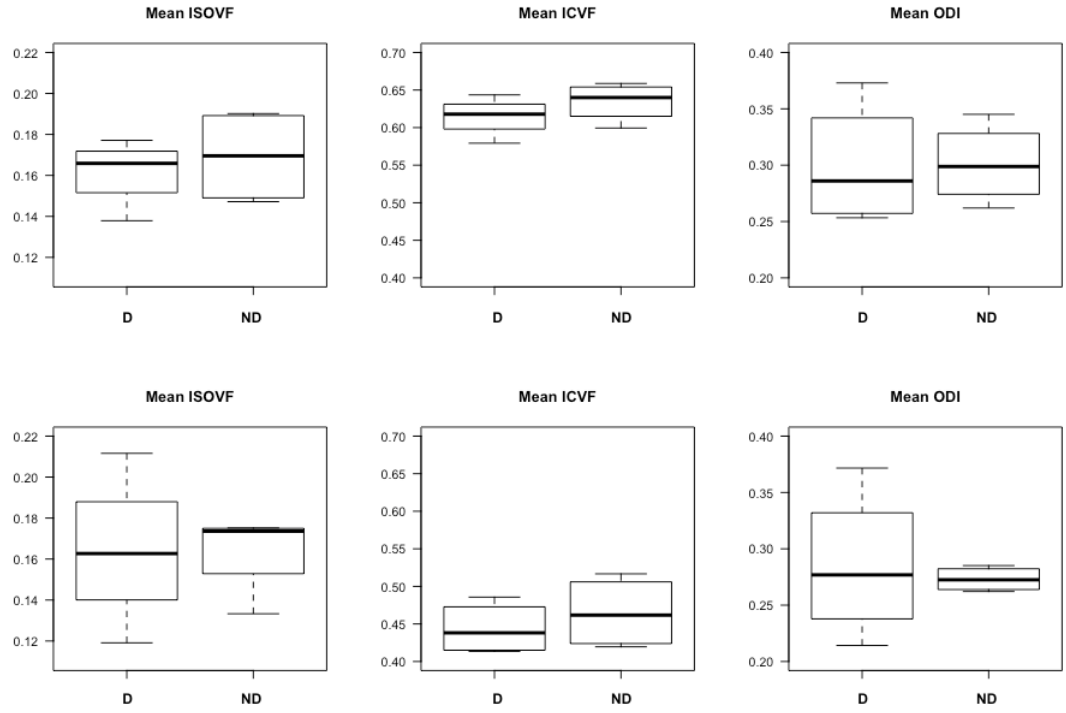

Fig. 5.7 – Boxplots comparing the mean of the different NODDI metrics between the two hemispheres (dominant (D) vs non-dominant (ND)) for control subjects (on the top) and children with CP (on the bottom).

Table 5.3 – T-test results for the comparison of the different NODDI and DTI metrics between dominant hemisphere (D) and the non-dominant hemisphere (ND), for the healthy control subjects (HC) on the top and the children with CP (CP) on the bottom.

T-test D/ND HC				
Mean_AD	t = 0.34304	df = 3	p-value=	0.7542
Mean_RD	t = -0.51952	df = 3	p-value=	0.6393
Mean_MD	t = 0.044755	df = 3	p-value=	0.9671
Mean_FA	t = 1.0064	df = 3	p-value=	0.3884
Mean_ISOVF	t = -0.83093	df = 3	p-value=	0.467
Mean_ICVF	t = -2.5263	df = 3	p-value=	0.0857
Mean_ODI	t = -0.08798	df = 3	p-value=	0.9354

T-test D/ND CP				
Mean_AD	t = -0.70866	df = 3	p-value=	0.5296
Mean_RD	t = -0.67762	df = 3	p-value=	0.5466
Mean_MD	t = -1.6355	df = 3	p-value=	0.2005
Mean_FA	t = 0.55743	df = 3	p-value=	0.6161
Mean_ISOVF	t = 0.006447	df = 3	p-value=	0.9953
Mean_ICVF	t = -2.8172	df = 3	p-value=	0.06689
Mean_ODI	t = 0.42287	df = 3	p-value=	0.7009

In the boxplots in Fig. 5.6, a decrease in FA and an increase in RD and MD was observed in the non-dominant hemisphere compared to the dominant hemisphere. These variations correspond to the one observed between the control subjects and the children with CP. By consequence, the same conclusions can be draw: the parameters variation reflects a lower axonal density and a lower quantity of myelin in the non-dominant hemisphere.

The variation of AD was different between the control population and the population with CP. As explained before, no consensus has been found in the literature for the AD metric and no significant result was found in this thesis neither.

As expected these changes were not significant (Table 5.3) for the control subjects. The same conclusion was observed for the children with CP for which a difference between the two hemispheres would be expected, since the children have functional asymmetries (Table 4.1).

In conclusion, no difference was found between the two hemispheres either for the control subjects or for the children with CP.

5.3 Behavioural analysis

A correlation was calculated between each behavioural score (PEDI daily life and mobility, ACTILIM in logit and percent) and the mean of each NODDI and DTI metric for both dominant (D) and non-dominant (ND) hemispheres. The behavioural surveys were only asked to the parents of children with CP. By consequence, the following results only concern this population. The results are shown in Table5.4.

Table 5.4 – Table with the correlation values between behavioural scores and the microstructure metrics. PEDI_DA=PEDI-CAT for daily activities domain, PEDI_M=PEDI-CAT for mobility domain, AL_L= ACTIVLIM in [Logit] and AL_P= ACTIVLIM in [%]. In green: the correlation superior to 0.9; in red: the correlations inferior to -0.9.

Behaviour	PEDI_DA	PEDI_M	AL_L	AL_P
Mean_AD_D	0.02297324	-0.2571795	0.5007839	-0.6055746
Mean_AD_ND	0.05498725	0.2667631	0.6388655	-0.6602385
Mean_RD_D	0.7891882	0.4604506	-0.06291252	0.1204012
Mean_RD_ND	0.7143081	0.368175	0.06365557	0.001309447
Mean_MD_D	0.6071127	0.3937686	0.1215745	-0.1133598
Mean_MD_ND	0.46972	0.4399191	0.3261927	-0.2953026
Mean_FA_D	-0.9688221	0.2478522	0.3925562	-0.5053238
Mean_FA_ND	-0.9933299	-0.4762364	0.5579113	-0.6795349
Mean_ISOVF_D	-0.3409	-0.4864601	0.9149172	-0.7647279
Mean_ISOVF_ND	0.314153	-0.7835052	0.5618309	-0.4042475
Mean_ICVF_D	-0.9585663	-0.2571795	0.5202685	-0.5501121
Mean_ICVF_ND	-0.9114546	-0.7164668	0.3824766	-0.406093
Mean_ODI_D	-0.4879337	0.1847041	-0.3404662	0.2828399
Mean_ODI_ND	-0.7589529	-0.4065071	0.00202659	-0.06806572

Significant negative correlation for both hemispheres was found between the PEDI-CAT score and the FA and secondly between the PEDI-CAT score and the ICVF. These correlations are highlighted in red in Table 5.4. The PEDI-CAT measures the mobility of the child in his daily activity. A higher PEDI-CAT score is related to a higher mobility. These negative correlations are by consequence unexpected. The FA and ICVF are higher in control subjects than in children with CP. A higher FA and ICVF should be therefore correlated positively with a higher behavioural score.

A significant positive correlation was found between the ACTILIM (in logit) and the ISOVF only for the dominant hemisphere. This result is also unexpected. In the comparison between the two populations no difference was found, showing that there is no different in CSF between the two populations.

To better understand the reason of these unexpected correlations, scatter-plot were drawn and are represented in Fig. 5.8.

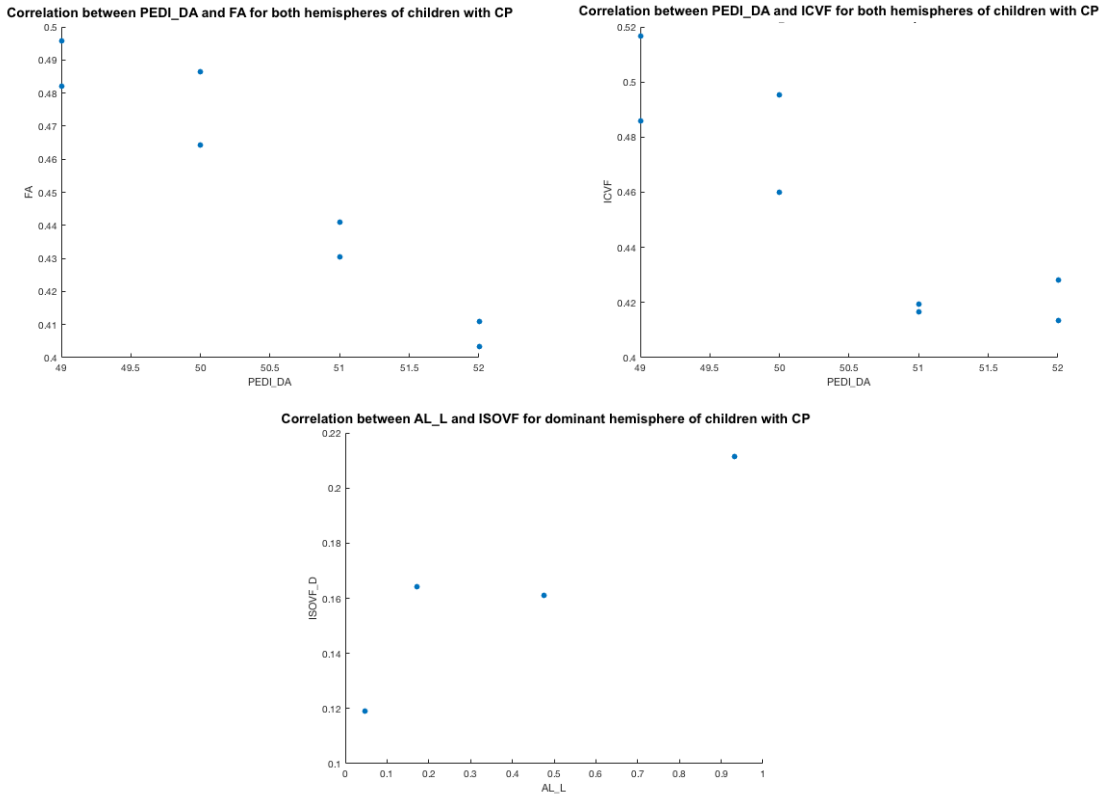

Fig. 5.8 – Graph of significant correlations between behavioural scores and microstructure metrics.

The values in these graphs are spread out and highlight clearly the correlation, which can be represented by a straight line across the different points. By consequence, the graphs do not help to understand the causes of the unexpected correlations.

In conclusion, the small size of the population (4 subjects) with CP does not allow to give coherent and significant correlation between the microstructure parameters and the behavioural scores.

Chapter 6

Improvements and future perspectives

In this chapter, further improvement to the analysis is suggested. First, more detailed and precise results could have been found by improving certain elements of the analysis. This chapter will make several propositions for improvement. Afterwards, additional analysis methods performed on the subjects would have allowed to gather a more complete data set. Finally, deeper analysis of the existing data set would have allowed to improve the comparison between the two populations and to select a more efficient software for each analysis step.

6.1 Propositions for improvement

During the analysis, more detailed and precise results could have been found by improving certain elements of the analysis:

- To improve the sensitivity of detecting differences in DWI metrics which occur in a portion of the CST, the tract could be divided into three tract segments (inferior, middle and superior) [24].
- The FA threshold was defined arbitrarily at 0.2 for the tracking. Instead of using an arbitrary value the FA threshold could have been determined by the FA average value of white matter.
- The tracking of the children with CP and the control subjects was based on different measurements. The control subjects tracking was based on DKI and the children with CP tracking was based on a reduced DTI (only one shell considered). The reduction to one shell for the control subjects DTI was not calculated due to the time constraints, but should be done to be more rigorous.
- To have more reliable results, the number of subjects should have been increased. The two populations should have more similar characteristics, by reducing the age difference between the control subjects and the children with CP.
  Another option could have been to compare two time points of the same subject: before and after motor skill training.

- The results of volume (number of voxels) and length of the CST could not be analyzed: the difference between the brain volumes of the different subjects, and more specifically between the control subjects and the children with CP. These metrics could be useful to compare the CST volume of the same subject, before and after a motor skill training. Indeed, possible modifications in the number of voxels of CST can be observed after a training. The CST structure might be restored by intensive motor skill training [2].
- Each program is defined by different conventions (neurological or radiological views), to facilitate the transfer from one to the other, a vitamin pill could be placed on one side during acquisition.

6.2 Methods to gather additional data

The following methods could be performed in order to gather additional information about the brain structure:

- Functional MRI (fMRI) could be performed to highlight the sensorimotor network. This approach can show asymmetries following focal brain injury in the corticospinal tract. A resting state analysis could also be conducted, this can show a disruption in connectivity of somato-motor and frontoparietal executive networks predicted motor impairment[5]. fMRI can also be used to perform fMRI-guided tractography.
- A second technique that could be added is the Transcranial Magnetic Stimulation (TMS). It can measure the resting motor threshold, which reflects motor cortex excitability and the development stage of corticospinal tract myelination, as well as the membrane characteristics and synaptic efficacy of the cortical and spinal motor neurons[5].
- Both fMRI and TMS can demonstrate the impact of motor skill training.
- The DKI is calculated to have better MD map. By consequence, DKI metrics could easily be extracted from ExploreDTI and be analyzed to have more metrics to compare the two populations.

6.3 Deeper analysis on existing data set

Deeper analysis could be carried out on the existing data set to obtain more precise and additional information.

- The analysis of somatosensory tract as explained in Chapter 3 could be performed. The optical projection tracts could also be analyzed. Indeed, cerebral visual impairment is a very common dysfunction in children with CP. The microstructural analysis of these tracts could offer additional information.

- Different software applications were briefly tried to create the DTI maps and the tracking (Appendix E). The DTI metrics between the different software applications could be compared. For example, the FA maps are different between ExploreDTI and FSL, as shown in Fig. 6.1. StarTrack [42] could have been used to estimate the tracking based on Richardson-Lucy Spherical Deconvolution, another estimation model.

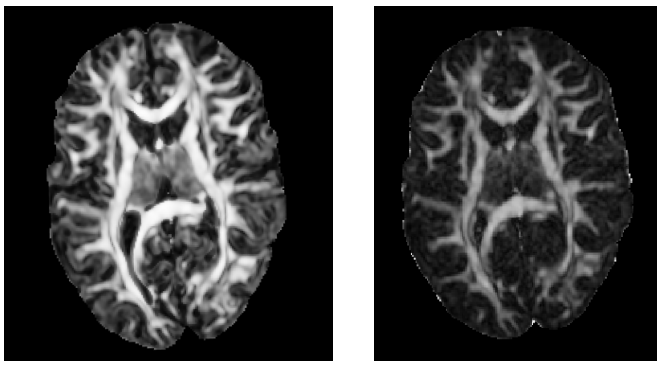

Fig. 6.1 – Comparison of FA maps between ExploreDTI (on the left) and FSL (on the right) software.

- The motion correction programs could also be compared. In the motion correction used for this thesis, only one b0 was used. This showed the limitation of this motion correction. Indeed, multiple b0 values are acquired during the sequences. Since the different shells are acquired at relatively long interval times, the use of the different b0s acquired between these shells could improve the motion correction.
  In Appendix C, graphs of the motion during the acquisition are shown for ExploreDTI correction. This kind of graphs could also be obtained by means of ecclog output file of FSL motion correction. These graphs could be a relevant indicator to compare the different motion correction software applications.

- With a higher number of subjects, the comparison of the lesions in white matter and gray matter might be an interesting analysis.

- The gain per supplementary shell might also be investigated. In the sequence of the children with CP, the last shell with a b-value of 5000 was not acquired. This decision was taken to reduce the sequence duration. The loss of information generated by this decision needs to be accurately quantified.

- Finally, more complex models exist to describe the microstructure. In these models, different fiber populations can be tacked into account. This allows to resolve the cross fibers problem. One of this model is the Distribution of Anisotropic Microstructural Environments in Diffusion-Compartment Imaging (DIAMOND). This model was analyzed in collaboration with Nicolas Delinte, and the analysis is shown in Appendix F.

Conclusion

Children with Cerebral Palsy (CP) have a completely transformed brain structure. This thesis investigates these structural changes by applying different microstructural models: Diffusion Tensor Imaging (DTI), Neurite Orientation and Dispersion Density Imaging (NODDI) and DIstribution of Anisotropic MicrOstructural eNvironments with DTI (DIAMOND). The results of the DIAMOND model were presented in Appendix F and were analyzed in collaboration with Nicolas Delinte. The metrics of these models were compared between a control population and one with CP. This analysis was focused only on Corticospinal Tract (CST) which is the most important tract for fine motor skills [3]. By consequence, a major step was to isolate this tract and to chose a suitable program to support this approach. ExploreDTI was chosen for its visual aspect which was important to draw the regions of interest (ROI) that were used to isolate the CST. This thesis defined a concrete semi-automated pipeline to isolate the CST in severely-deformed infant brains.

Until now, there is only a limited amount of literature focused on microstructure models applied on children with CP, only one paper has been found on NODDI and none on DIAMOND. Moreover, the analysis of bilateral lesions is uncommon. This thesis attempted to initiate research on the analysis of microstructure models calculated for children with bilateral lesions.

On the CST, the DTI metrics were calculated. A decrease of diffusion metrics (Mean Diffusivity (MD) and Radial Diffusivity (RD)) was observed which reflects the increased freedom of diffusion in the white matter and may reflect a degree of demyelination in children with CP. Moreover, an increase of Fractional Anisotropy (FA) highlights the lower fiber density in these children. This result was confirmed by the ICVF, a metric of NODDI.
By consequence, the DTI and NODDI metrics highlight the lower axonal density and the lack of myelin in the CST of children with CP.

The main advantage of the DIAMOND model is that it can manage different populations in each voxel: two anisotropic compartments and one isotropic compartment. The application of this model confirmed the results obtained by DTI and completed the information of the two other models by showing the heterogeneity of the tract and therefore the non-parallel structure of fibers in the CST.
By defining a framework to extract all these parameters from the CST, this thesis allowed the analysis of the CST modification due to CP, in an objective and quantitative way.

However, some metrics did not give any significant information. First, the AD metric needs future investigations. No consensus has been found in the literature, and the results for the DTI and the DIAMOND models did not find any significant results. Moreover, in the NODDI model, the ODI metric and in the DIAMOND model, the FD metric varied too much between the subjects to be analyzed. Finally, the behavioural analysis and the comparison of the two hemispheres, unfortunately did not lead to any significant result.

This thesis initiates the analysis of children with bilateral lesions. It confirms some results found in the literature for children with unilateral lesions, on children with bilateral lesions, and adds information by using the DIAMOND model.

To go further in the analysis, more subjects should be included to confirm the statistical trend observed and to analyze the metrics which were not significant in this thesis. Moreover, the comparison of subjects before and after motor training could be investigated to analyze its effect on the CST. Finally, more complex models which estimate the biological structure in a more direct way, could be investigated. For example, Microstructure Fingerprinting [43] estimates physically interpretable microstructural parameters such as indices of axon diameter and density, both in single and in crossing fascicles of axons, with no restriction on the data acquisition protocol. This kind of model should be calculated to have a higher number and more relevant metrics for the analysis and to continue the comprehension of the brain structure of children with bilateral lesions.

Bibliography

[1] Peter Rosenbaum, Nigel Paneth, Alan Leviton, Murray Goldstein, Martin Bax, Diane Damiano, Bernard Dan, Bo Jacobsson, et al. A report: the definition and classification of cerebral palsy april 2006. *Dev Med Child Neurol Suppl*, 109(suppl 109):8–14, 2007.

[2] Yannick Bleyenheuft, Laurence Dricot, Daniela Ebner-Karestinos, Julie Paradis, Geoffroy Saussez, Anne Renders, Anne De Volder, Rodrigo Araneda, Andrew M Gordon, and Kathleen M Friel. Motor skill training may restore impaired corticospinal tract fibers in children with cerebral palsy. *Neurorehabilitation and Neural Repair*, page 1545968320918841, 2020.

[3] Christos Papadelis, Harper Kaye, Benjamin Shore, Brian Snyder, Patricia Ellen Grant, and Alexander Rotenberg. Maturation of corticospinal tracts in children with hemiplegic cerebral palsy assessed by diffusion tensor imaging and transcranial magnetic stimulation. *Frontiers in human neuroscience*, 13:254, 2019.

[4] Benoit Scherrer, Armin Schwartzman, Maxime Taquet, Mustafa Sahin, Sanjay P Prabhu, and Simon K Warfield. Characterizing brain tissue by assessment of the distribution of anisotropic microstructural environments in diffusion-compartment imaging (diamond). *Magnetic resonance in medicine*, 76(3):963–977, 2016.

[5] Stephanie L Merhar, Elveda Gozdas, Jean A Tkach, Nehal A Parikh, Beth M Kline-Fath, Lili He, Weihong Yuan, Mekibib Altaye, James L Leach, and Scott K Holland. Neonatal functional and structural connectivity are associated with cerebral palsy at two years of age. *American Journal of Perinatology*, 37(02):137–145, 2020.

[6] I L Pykett, J H Newhouse, F S Buonanno, T J Brady, M R Goldman, J P Kistler, and G M Pohost. Principles of nuclear magnetic resonance imaging. *Radiology*, 143(1):157–168, 1982. PMID: 7038763.

[7] B. Kastler. *Comprendre l'IRM: Manuel d'auto-apprentissage*. Elsevier Masson, 2011.

[8] Macq Benoît Bol Anne, Lee John and Peeters Frank. Course notes gbio2050 medical imaging 2017-2018. *Université Catholique de Louvain*.

[9] Alberto De Luca. *Moving beyond DTI: non-Gaussian diffusion in the brain and skeletal muscle*. PhD thesis, 02 2017.

[10] Rita G. Nunes Patrícia Figueiredo. Course notes neuroimaging 2019-2020. *Instituto Superior Tecnico*.

[11] Mri step-by-step, interactive course on magnetic resonance imaging. `https://www.imaios.com/en`, 2008. [Accessed: March 2020].

[12] Patric Hagmann, Lisa Jonasson, Philippe Maeder, Jean-Philippe Thiran, Van J Wedeen, and Reto Meuli. Understanding diffusion mr imaging techniques: from scalar diffusion-weighted imaging to diffusion tensor imaging and beyond. *Radiographics*, 26(suppl_1):S205–S223, 2006.

[13] José G Raya. Diffusion-weighted imaging and diffusion tensor imaging. *Current Radiology Reports*, 2(3):37, 2014.

[14] Lauren J O'Donnell and Carl-Fredrik Westin. An introduction to diffusion tensor image analysis. *Neurosurgery Clinics*, 22(2):185–196, 2011.

[15] Do Tromp and DTI Scalars. How do they relate to brain structure. *The Winnower*, 3:e146119, 2016.

[16] Mark Jenkinson, Christian F Beckmann, Timothy EJ Behrens, Mark W Woolrich, and Stephen M Smith. Fsl. *Neuroimage*, 62(2):782–790, 2012.

[17] Ben Jeurissen, Alexander Leemans, Jacques-Donald Tournier, Derek K Jones, and Jan Sijbers. Investigating the prevalence of complex fiber configurations in white matter tissue with diffusion magnetic resonance imaging. *Human brain mapping*, 34(11):2747–2766, 2013.

[18] Jelle Veraart, Dirk HJ Poot, Wim Van Hecke, Ines Blockx, Annemie Van der Linden, Marleen Verhoye, and Jan Sijbers. More accurate estimation of diffusion tensor parameters using diffusion kurtosis imaging. *Magnetic resonance in medicine*, 65(1):138–145, 2011.

[19] Chantal MW Tax, Willem M Otte, Max A Viergever, Rick M Dijkhuizen, and Alexander Leemans. Rekindle: robust extraction of kurtosis indices with linear estimation. *Magnetic Resonance in Medicine*, 73(2):794–808, 2015.

[20] Ben Jeurissen, Jacques-Donald Tournier, Thijs Dhollander, Alan Connelly, and Jan Sijbers. Multi-tissue constrained spherical deconvolution for improved analysis of multi-shell diffusion mri data. *NeuroImage*, 103:411–426, 2014.

[21] Flavio Dell'Acqua and J.-Donald Tournier. Modelling white matter with spherical deconvolution: How and why? *NMR in Biomedicine*, 32(4):e3945, 2017.

[22] Hui Zhang, Torben Schneider, Claudia A. Wheeler-Kingshott, and Daniel C. Alexander. Noddi: Practical in vivo neurite orientation dispersion and density imaging of the human brain. *NeuroImage*, 61(4):1000 – 1016, 2012.

[23] Maira Tariq, Torben Schneider, Daniel C. Alexander, Claudia A. Gandini Wheeler-Kingshott, and Hui Zhang. Bingham–noddi: Mapping anisotropic orientation dispersion of neurites using diffusion mri. *NeuroImage*, 133:207 – 223, 2016.

[24] Samuel T. Nemanich, Bryon A. Mueller, and Bernadette T. Gillick. Neurite orientation dispersion and density imaging quantifies corticospinal tract microstructural organization in children with unilateral cerebral palsy. *Human Brain Mapping*, 40(17):4888–4900, 2019.

[25] Chitra Sankar and Nandini Mundkur. Cerebral palsy-definition, classification, etiology and early diagnosis. *The Indian Journal of Pediatrics*, 72(10):865–868, 2005.

[26] ARC physical therapy. basal ganglia anatomy, March 2019.

[27] Loic Botrel. Brain-computer interfaces (bcis) based on sensorimotor rhythms-evaluating practical interventions to improve their performance and reduce bci inefficiency. 2018.

[28] Marco Catani and Michel Thiebaut De Schotten. A diffusion tensor imaging tractography atlas for virtual in vivo dissections. *cortex*, 44(8):1105–1132, 2008.

[29] Disha Gupta, Alexandre Barachant, Andrew M Gordon, Claudio Ferre, Hsing-Ching Kuo, Jason B Carmel, and Kathleen M Friel. Effect of sensory and motor connectivity on hand function in pediatric hemiplegia. *Annals of neurology*, 82(5):766–780, 2017.

[30] F Lennartsson, L Holmström, A-C Eliasson, O Flodmark, H Forssberg, J-D Tournier, and B Vollmer. Advanced fiber tracking in early acquired brain injury causing cerebral palsy. *American Journal of Neuroradiology*, 36(1):181–187, 2015.

[31] Anatomy Note. Anatomy note. `https://www.anatomynote.com`. [Accessed: April 2020].

[32] AnatomyQA. Anatomy made simple. `https://anatomyqa.com`. [Accessed: May 2020].

[33] Jane Case-Smith and Helen Alexander. The bayley-iii motor scale. In *Bayley-III clinical use and interpretation*, pages 77–146. Elsevier, 2010.

[34] Pawel J Winklewski, Agnieszka Sabisz, Patrycja Naumczyk, Krzysztof Jodzio, Edyta Szurowska, and Arkadiusz Szarmach. Understanding the physiopathology behind axial and radial diffusivity changes—what do we know? *Frontiers in neurology*, 9:92, 2018.

[35] Ganesh Adluru, Yaniv Gur, Jeffrey S Anderson, Lorie G Richards, Nagesh Adluru, and Edward VR DiBella. Assessment of white matter microstructure in stroke patients using noddi. In *2014 36th Annual International Conference of*

the IEEE Engineering in Medicine and Biology Society, pages 742–745. IEEE, 2014.

[36] Benjamin J Shore, Benjamin G Allar, Patricia E Miller, Travis H Matheney, Brian D Snyder, and Maria Fragala-Pinkham. Measuring the reliability and construct validity of the pediatric evaluation of disability inventory–computer adaptive test (pedi-cat) in children with cerebral palsy. *Archives of physical medicine and rehabilitation*, 100(1):45–51, 2019.

[37] Yannick Bleyenheuft, Julie Paradis, Anne Renders, Jean-Louis Thonnard, and Carlyne Arnould. Activlim-cp a new rasch-built measure of global activity performance for children with cerebral palsy. *Research in developmental disabilities*, 60:285–294, 2017.

[38] A. Leemans, B. Jeurissen, J. Sijbers, and D.K. Jones. Exploredti: a graphical toolbox for processing, analyzing, and visualizing diffusion mr data. In *Proc Intl Soc Mag Reson Med*, volume 17, page 3537, 2009.

[39] Laidlaw-D. H. Cabeen, R. P. and A. W. Toga. Quantitative imaging toolkit: Software for interactive 3d visualization. In *Data Exploration, and Computational Analysis of Neuroimaging Datasets. Proceedings of the International Society for Magnetic Resonance in Medicine (ISMRM)*, page 2854, 2018.

[40] R Core Team. *R: A Language and Environment for Statistical Computing*. R Foundation for Statistical Computing, Vienna, Austria, 2017.

[41] Sheng-Kwei Song, Shu-Wei Sun, Michael J Ramsbottom, Chen Chang, John Russell, and Anne H Cross. Dysmyelination revealed through mri as increased radial (but unchanged axial) diffusion of water. *Neuroimage*, 17(3):1429–1436, 2002.

[42] Flavio Dell'Acqua. *StarTrack : Spherical Deconvolution Tractography Tools*. NATBRAINLAB, Vienna, Austria, 2011-2019.

[43] Gaëtan Olivier D Rensonnet. In vivo diffusion magnetic resonance imaging of the white matter microstructure from dictionaries generated by monte carlo simulations: development and validation. Technical report, EPFL, 2019.

[44] R Goebel. Brainvoyager. *Brain Innovation, Maastricht, The Netherlands: Brain Innovation BV*, 2000.

[45] Flavio Dell'Acqua, Paola Scifo, Giovanna Rizzo, Marco Catani, Andrew Simmons, Giuseppe Scotti, and Ferruccio Fazio. A modified damped richardson–lucy algorithm to reduce isotropic background effects in spherical deconvolution. *Neuroimage*, 49(2):1446–1458, 2010.

[46] Chris Rorden. Mricron. *Retrieved from*, 2007.

[47] Zach Eaton-Rosen, Benoit Scherrer, Andrew Melbourne, Sebastien Ourselin, Jeffrey J Neil, and Simon K Warfield. Investigating the maturation of microstructure and radial orientation in the preterm human cortex with diffusion mri. *NeuroImage*, 162:65–72, 2017.

Appendix A

Program scheme

Pursuing the objectives to give a global view, all the different steps across the different programs and their inputs/outputs are mapped.

A.1 FSL and ExploreDTI

The first scheme explains the motion correction by FSL, the tracking by ExploreDTI and the extraction of the DTI metrics.

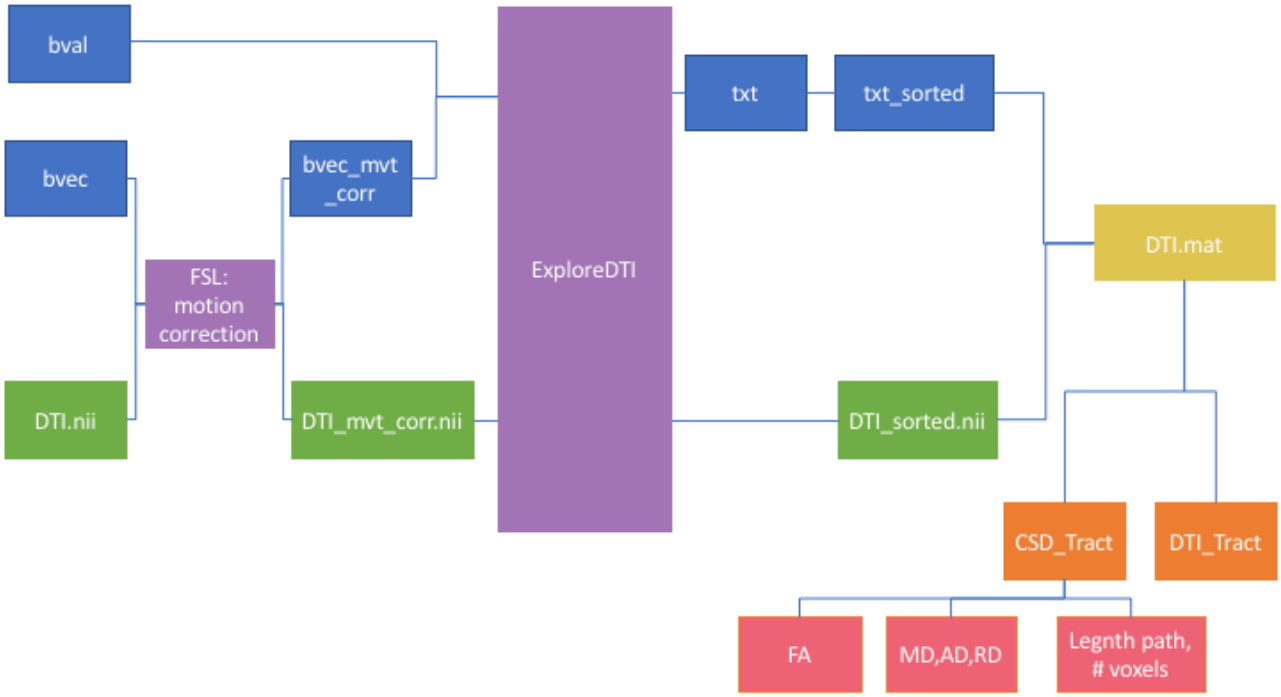

Fig. A.1 – Scheme for the motion correction, the tracking and the extraction of tensor metrics.

A.2 QIT and Python

This second scheme explains the extraction of the NODDI metrics.

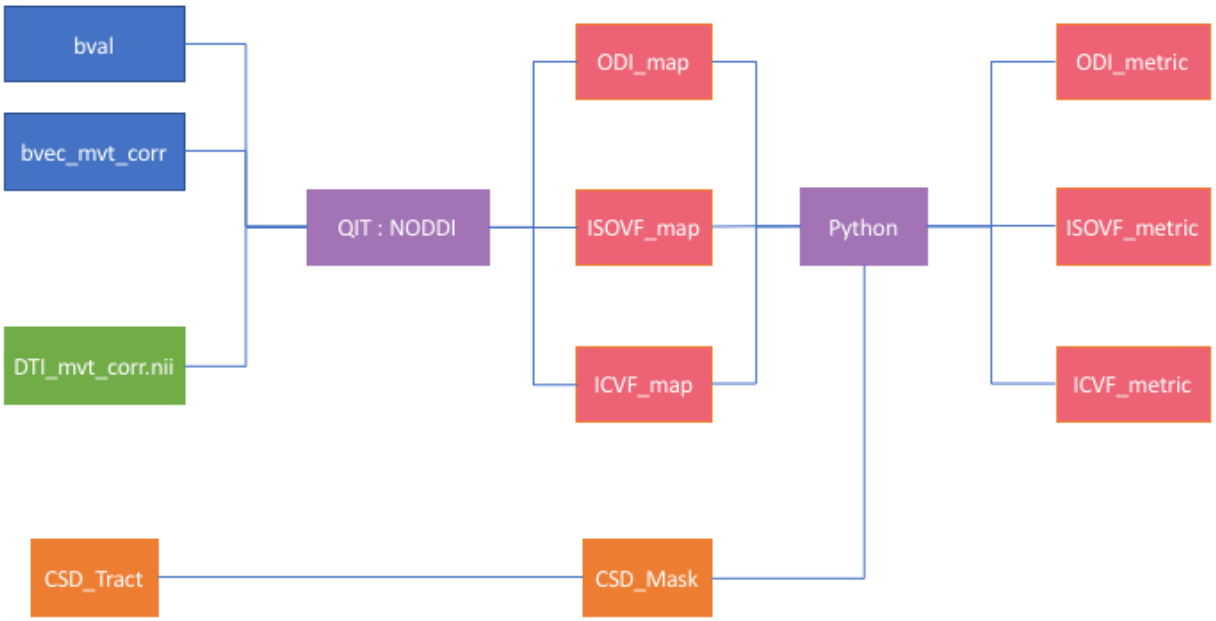

Fig. A.2 – Scheme for the calculation of NODDI maps and metrics.

Appendix B

Acquisition parameters

A typical acquisition is described by three parameters: G, δ and Δ as shown in Fig.B.1. The deltas can be decomposed in more detailed timing as shown in Fig.B.2. All the values of these parameters for the two types of sequences (control and children with CP) are shown in Fig.B.3.

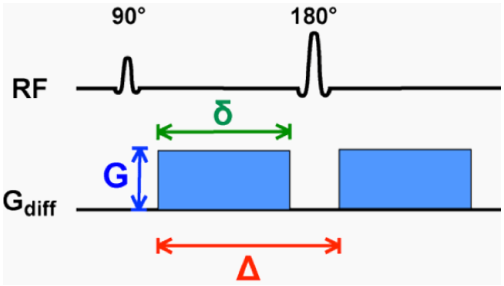

Fig. B.1 – Description of DTI sequence.

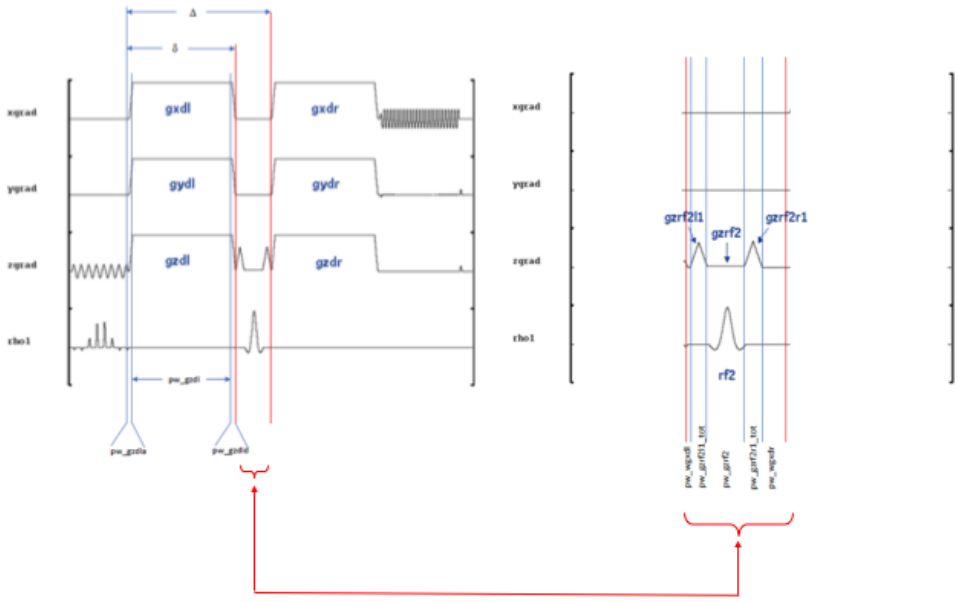

Fig. B.2 – Zoom details of DTI sequence described in Fig.B.1.

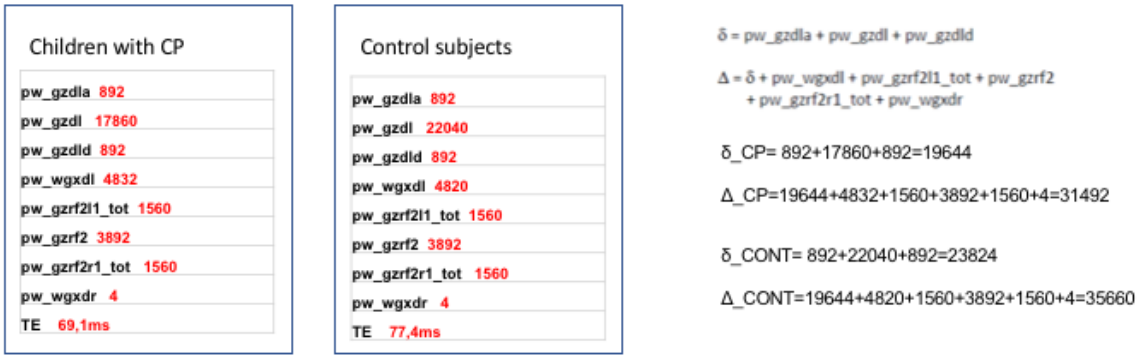

Fig. B.3 – Parameters values described in Fig. B.2 in microseconds.

Appendix C

Program for motion correction

Two programs were tried to correct the movement, **FSL** [16] and **ExploreDTI** [38]. The results of these two motion corrections are shown in Fig. C.1 and C.2.

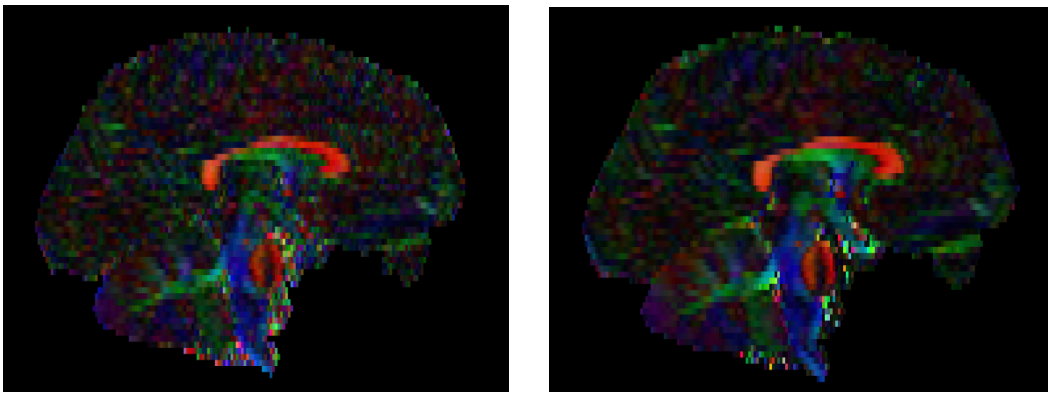

Fig. C.1 – Comparison of motion correction of the subject 2 with FSL (on the left) and with ExploreDTI (on the right) in the sagittal view.

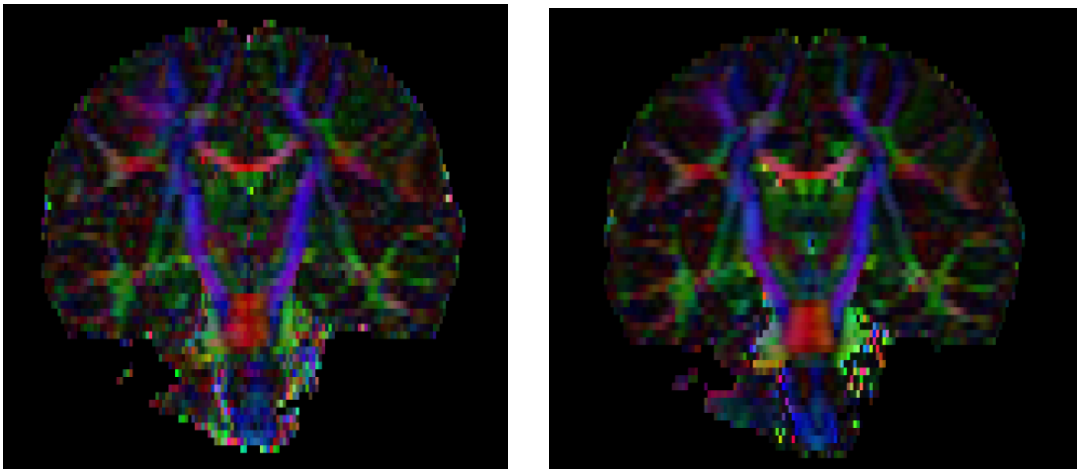

Fig. C.2 – Comparison of motion correction of the subject 2 with FSL (on the left) and with ExploreDTI (on the right) in the coronal view.

The results of the correction realized by ExploreDTI and FSL are quite similar, even if the Explore DTI ones seem a bit smoother.
The comparison of the DTI before and after the correction are shown in Fig. C.3. The modifications applied by the motion correction, three translations (in millimeters) and three rotations (in degrees), are represented on the graphs in the Fig. C.4 for the subject 2.

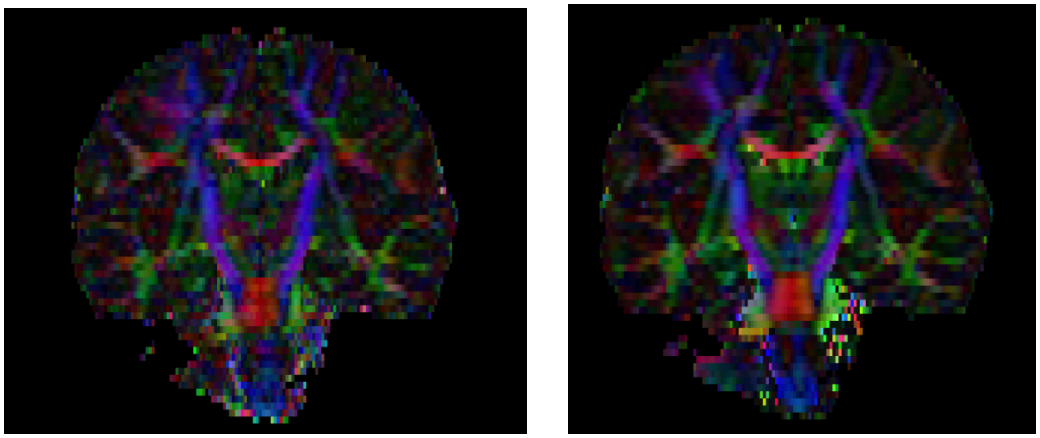

Fig. C.3 – Comparison before and after ExploreDTI motion correction (coronal view of subject 2).

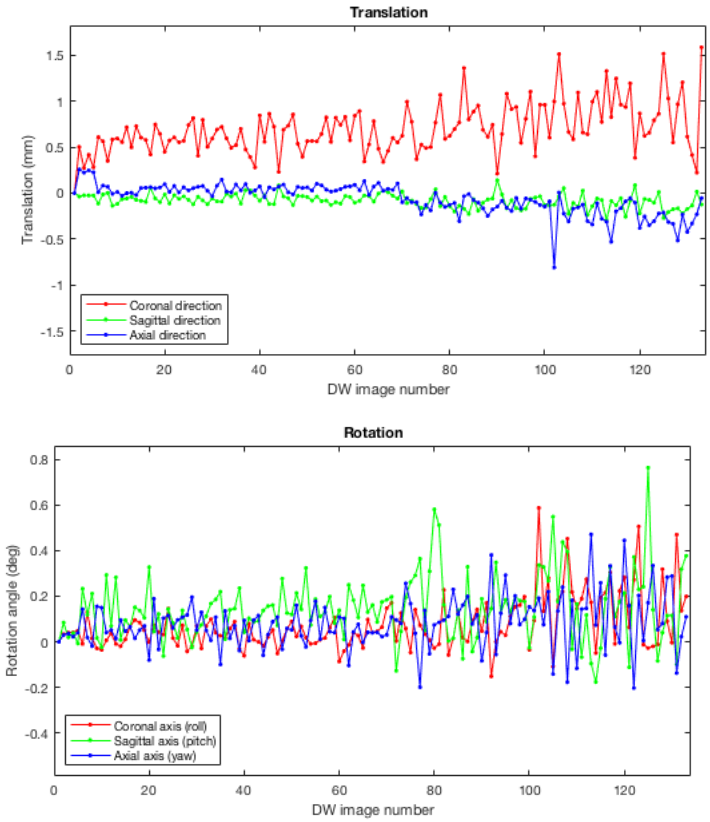

Fig. C.4 – Graph of the modifications done by the motion correction, 3 translations and 3 rotations, for the subject 2.

Even if ExploreDTI seemed to be a good and easier choice as the tracking will be realized with this program, a problem arisen at the extraction of the b-vectors and b-values after the motion correction.
The program was not able to modify the b-vector of the multi-shell sequences after the motion correction correctly. As the vectors were not normalized (with norm=1) for all the b-values, the program failed to extract the correct b-vector after motion correction. In the sequence used for this master thesis, the b-vectors were normalized at 1 for the highest b-value and smaller for the b-vectors corresponding to the other b-values. The sequences are shown in Appendix I.1 and the normalization is easy to see in the line highlighted in red. This format was chosen to minimize the warm-up of the gradient in the MRI.

To solve this issue, b-vectors were normalized but with this modification, the DTI was not correct as shown in Fig. C.5.

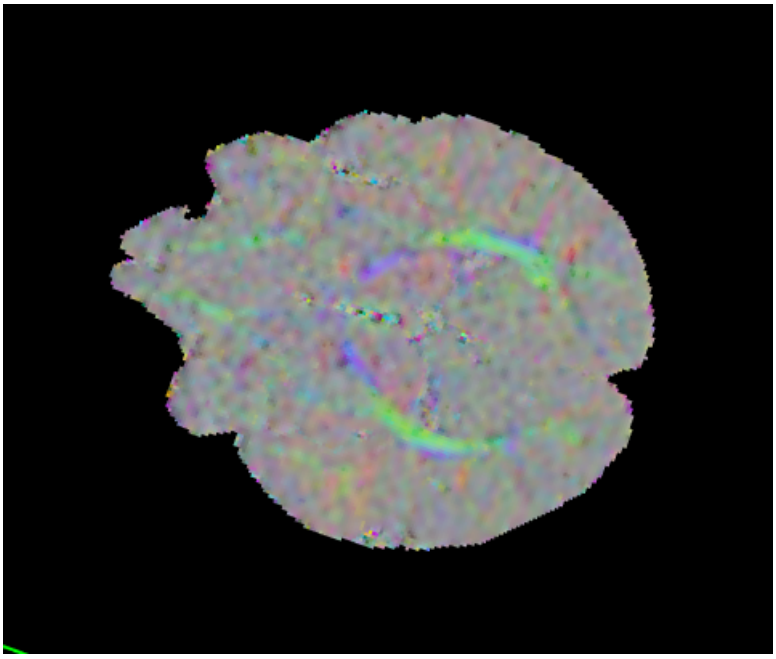

Fig. C.5 – DTI with b-vectors normalized at 1 for all shells.

To fix this issue, a deeper understanding of the program would be required by going out of the interface created by ExploreDTI and analyze the code on which it runs.

Due to the time constraint, this issue was not solved and FSL was finally chosen for the motion correction.

Appendix D

Movement results

D.1 Rejected subjects

Three of the seven subjects with CP were rejected because, even after motion correction, the DTI data was to noisy. By looking at the DTI results after motion correction, the cerebral structures were hardly identifiable. The three colors corresponding to the three principal directions were not as expected.
For the subject 4 (Fig. D.1), the CST was not identifiable, it was completely mixed. The corpus callosum was green for a major part, instead of being red as it goes from one hemisphere to the other.
On subject 6 (Fig. D.2), the CST was blurry, between blue and red color and the corpus callosum is not identifiable.
On subject 7 (Fig. D.3), the images were blurry with green CST.
To confirm this visual analysis, CST tracking was tried but no conclusive CST result stands out. The Fig. D.4 gives an example of the tracking for subject 4, no CST fibers were identifiable.

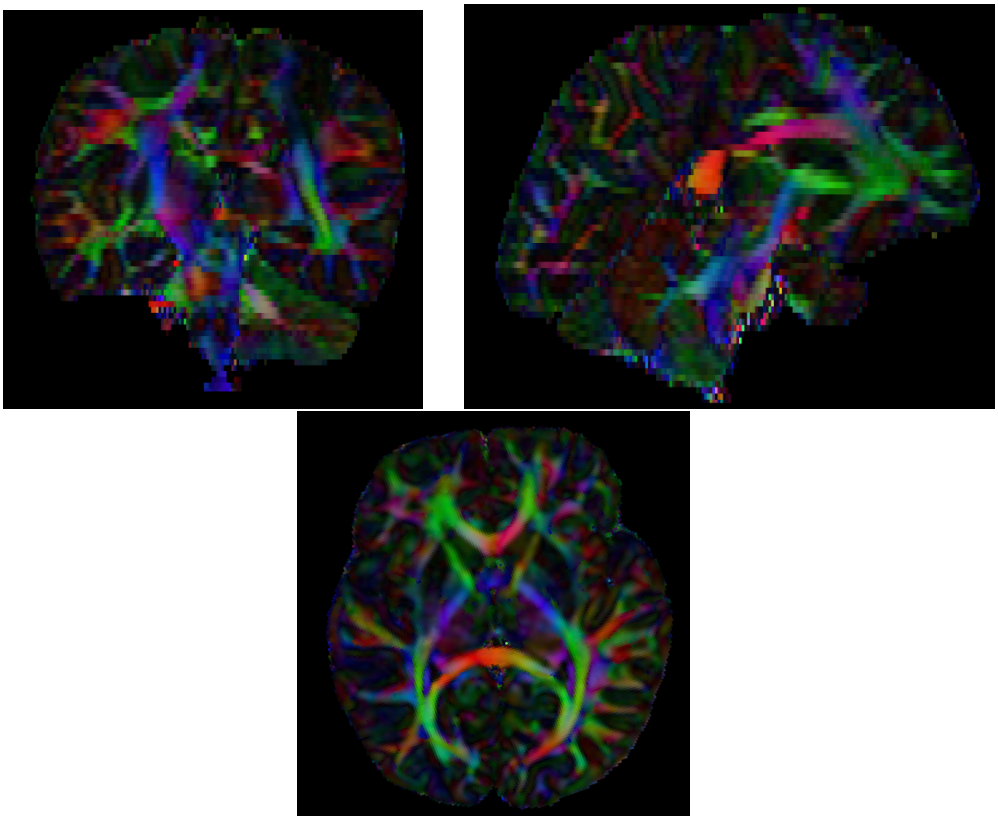

Fig. D.1 – DTI after motion correction of the subject 4.

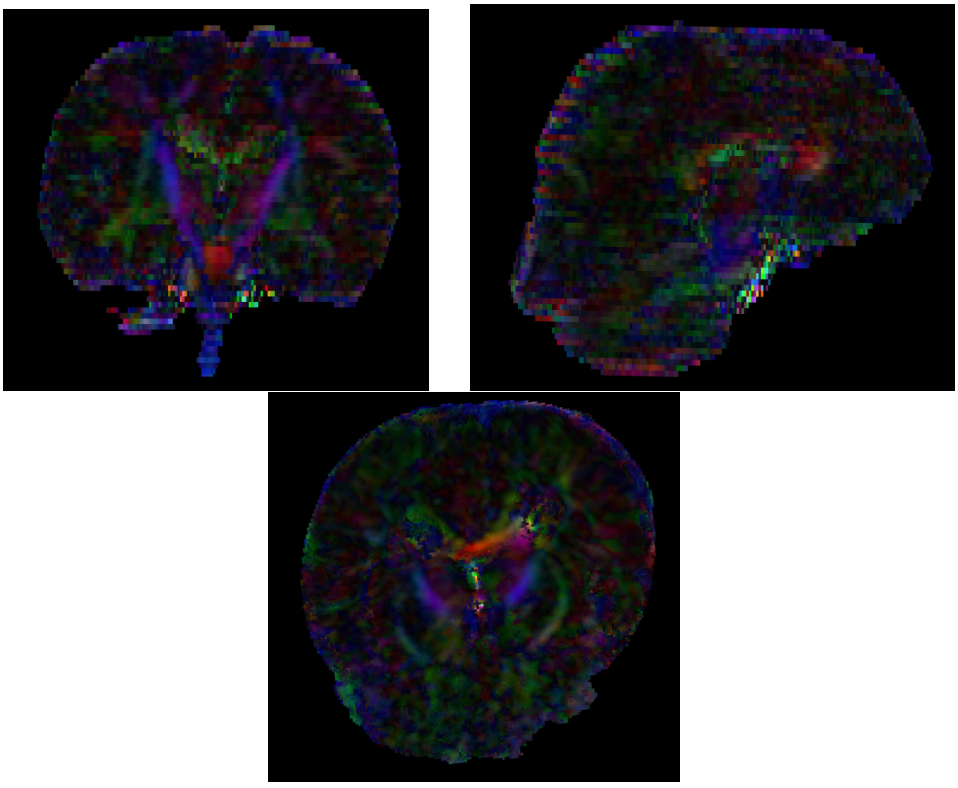

Fig. D.2 – DTI after motion correction of the subject 6.

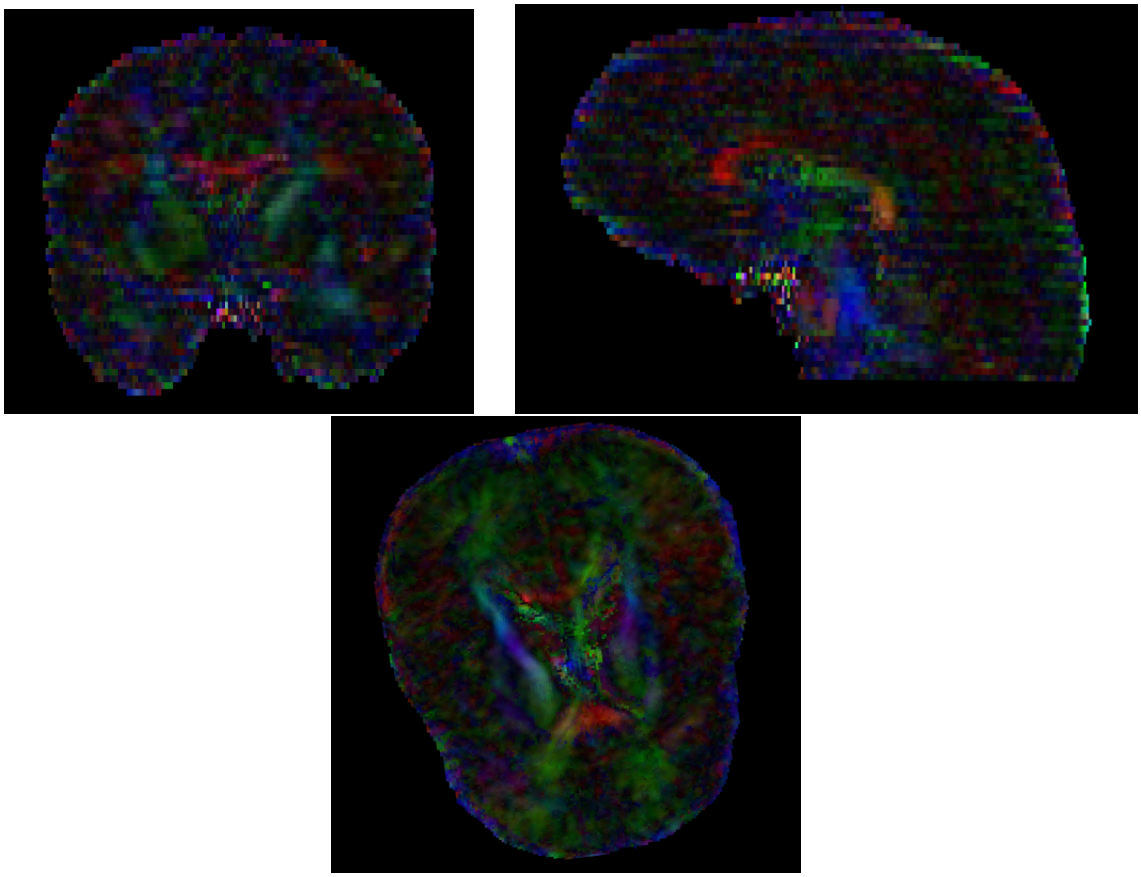

Fig. D.3 – DTI after motion correction of the subject 7.

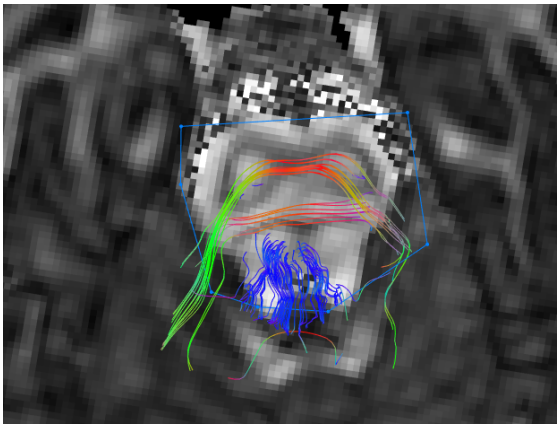

Fig. D.4 – CST tracking test on DTI after motion correction of the subject 4.

D.2 Motion correction graphs

As additional information, motion graphs are presented for three rejected subjects in Fig. D.5. The rotation angle is given in degrees and the translation in millimeters.

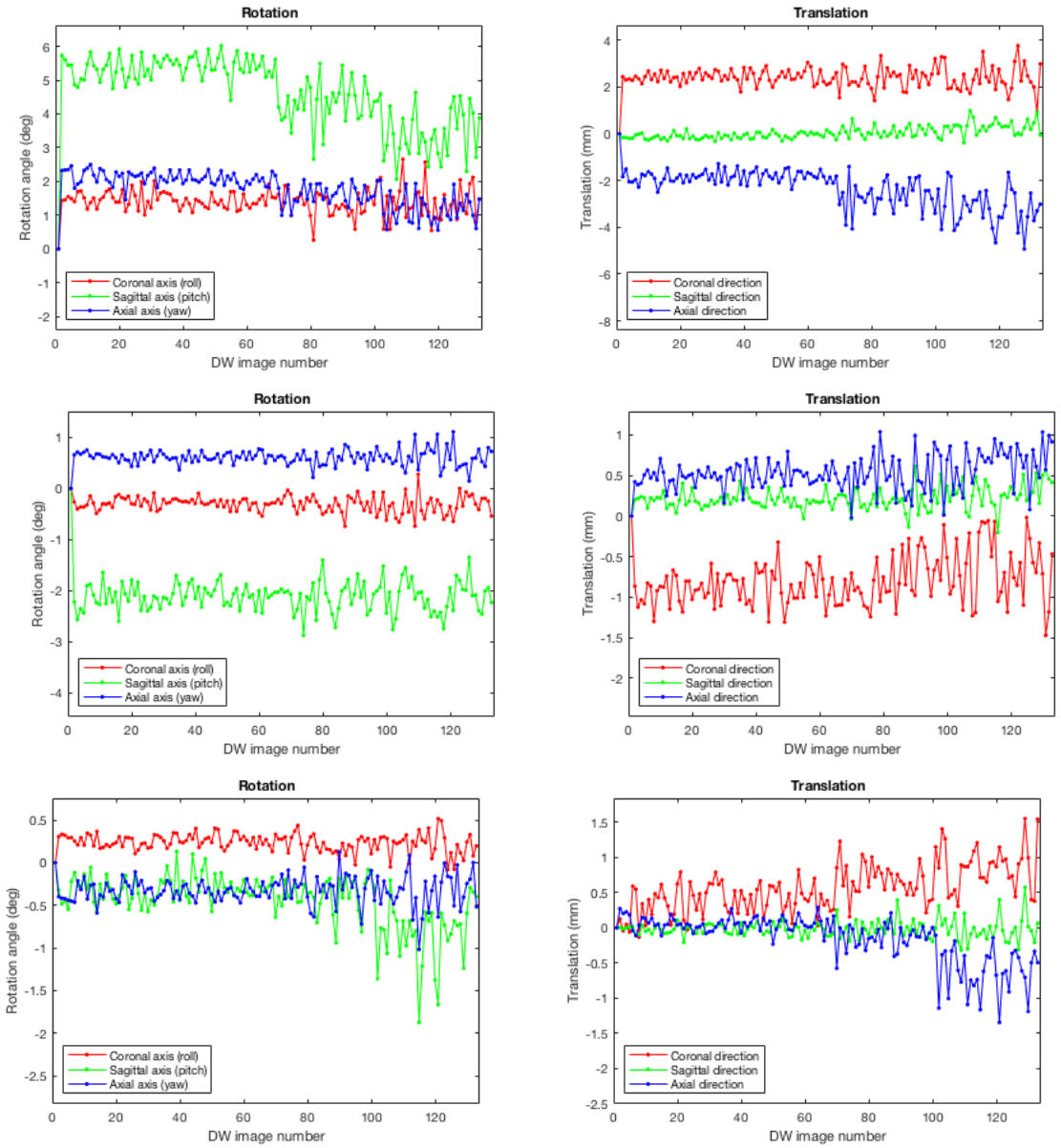

Fig. D.5 – Graph of the modifications done by the motion correction, three translations and 3 rotations, for the subject 1 (top), three (middle) and 5 (bottom).

Appendix E

Different programs testing

E.1 BrainVoyager

Different other programs than the final one chosen for this report were also tested. The first one was **BrainVoyager** (BV) [44]. The FA (Fig. E.1) and MD (Fig. E.2) maps were easily calculated.

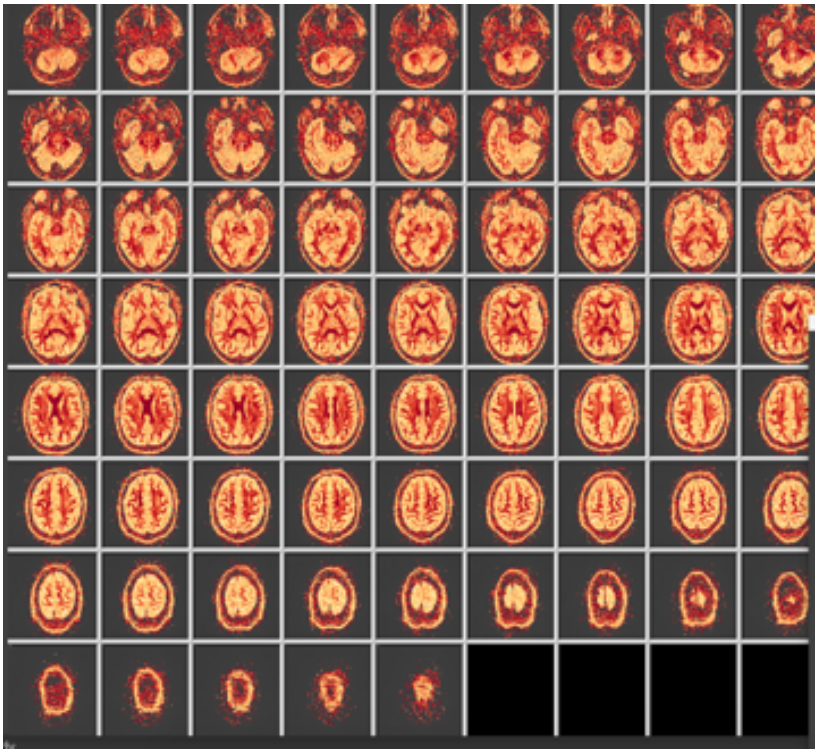

Fig. E.1 – FA for the different slices calculated by BV.

Fig. E.2 – MD for the different slices calculated by BV.

A real advantage of BV was the easy co-registration between the anatomical MRI and the DTI (Fig. E.3).

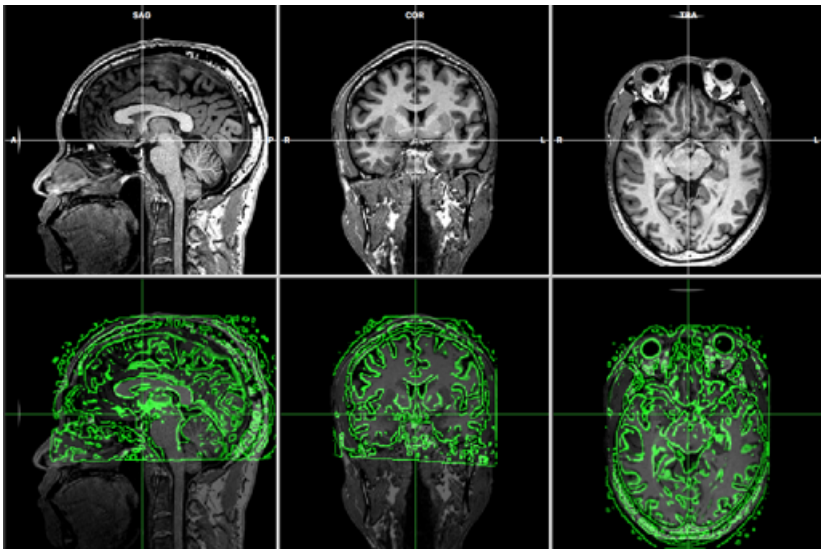

Fig. E.3 – Results of the co-registration between the anatomical MRI and the DTI of the same subject.

After this co-registration, the FA and the MD (Fig. E.6) were plotted on the anatomical image of the patient.

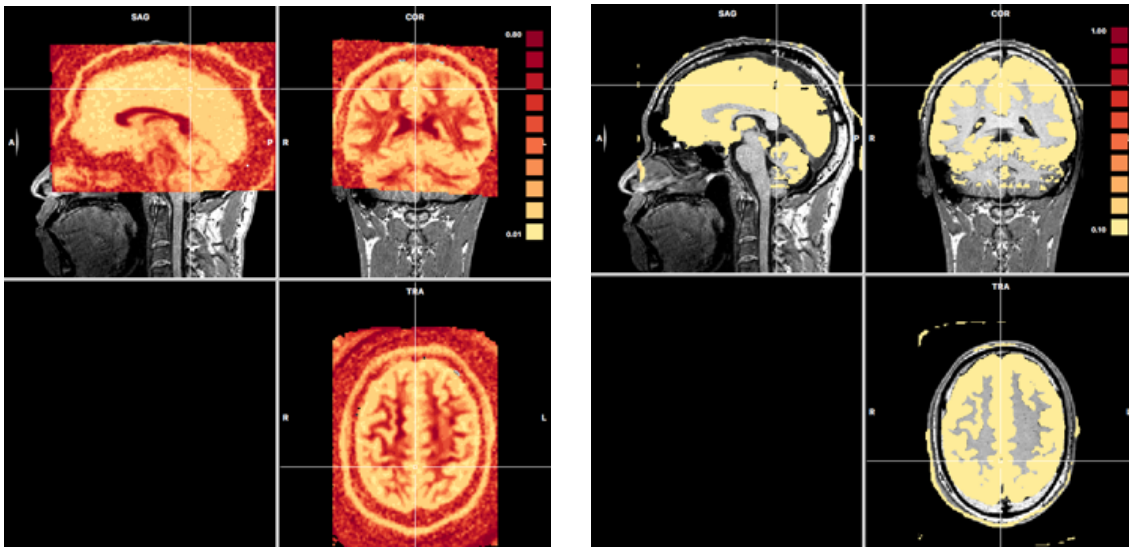

Fig. E.4 – FA (on the left) and MD (on the right) maps registered on the patient anatomical MRI.

Finally, the colored map with the different eigenvectors was obtained (Fig. E.5).

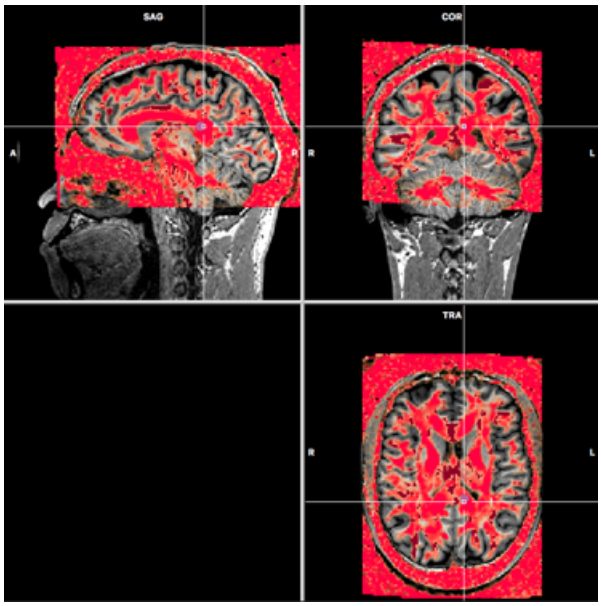

Fig. E.5 – Principal direction map registered on the patient anatomical MRI.

The problem was that only a test version of BV was available. Moreover, better feedbacks were received about the tracking with ExploreDTI than with BV.

E.2 FSL

The FA, MD and the colored maps were obtained with **FSL** (Fig. E.6).

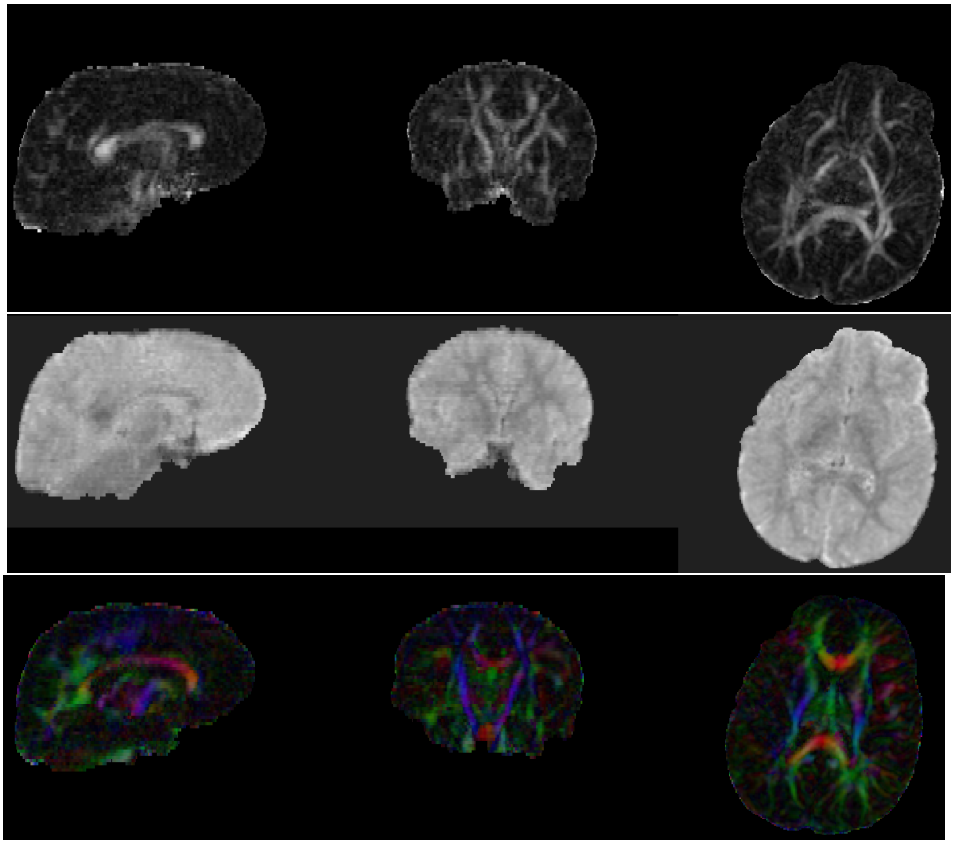

Fig. E.6 – FA, MD and colored maps calculated with FSL.

As with ExploreDTI, the MD with FSL was not correct. In this thesis, no further investigation was performed to understand the reasons of this issue. Moreover, the tracking with FSL was time consuming.

E.3 RL-SD: Richardson-Lucy Spherical Deconvolution

There are some other methods based on spherical deconvolution, the one explained here is the Richardson-Lucy (RL-SD)[21]. The advantage of this technique is its robustness to noise and to inaccuracies in the definition of the fibre response. The RL algorithm, that also tries to estimate the fODF, can be described by the following equation:

$$\left[f^{(k+1)}\right]_i = \left[f^{(k)}\right]_i \frac{\left[H^T s\right]_i}{\left[H^T H f^{(k)}\right]_i}$$

with:

- k is the k^{th} algorithm iteration;
- $[f]_i$ is the i^{th} element of the n $\times$ 1 vector f containing the fODF values calculated along a uniform set of directions;

- s is the m $\times$ 1 vector of DWI signals acquired along the HARDI sampling normalized to the b = 0 signal;
- H is the m $\times$ n circulant matrix describing the fibre response function, where every column represents the fibre response profile oriented along one of the n directions.

By definition, H and s are non-negative. The non-negativity of the solution is guaranteed with the initial condition the $\left[f^{(0)}\right]_i \geq 0$ [21]. Using this approach, the problem of non-physical negative fiber orientation shown in CSD is solved. Another advantage of this model is its low computational processing time.

The **damped Richardson Lucy algorithm (dRL-SD)**, is a modified version of this algorithm which is most largely used. The RL algorithm is modified with a damping procedure to reduce the effect of the isotropic partial volume. The damping occurs when differences between data and the recovered object are close to or lower than the noise level. For larger differences, the algorithm acts as the original RL form[45].

$$\left[f^{(k+1)}\right]_i = \left[f^{(k)}\right]_i \left(1 + \left[u^{(k)}\right]_i \frac{\left[H^T s - H^T H f^{(k)}\right]_i}{\left[H^T H f^{(k)}\right]_i}\right)$$

with:

- u, a vector (n $\times$ 1) performs a damping operation on each element of f.

In practice, the dRL-SD algorithm is very efficient to suppress spurious fODF lobes or to quasi-eliminate ringing effects in the presence of the partial volume effect [21].

This type of spherical deconvolution is used by StarTrack [42].

E.4 DIPY

Finally, tracking was tried with **DIPY** on Python (Fig. E.7). Python is not easily accessible to users non familiar with coding (as clinical users) and drawing ROI directly on DTI was not possible with DIPY. A solution could be to draw ROI in MRIcron [46] and use them for the tracking in DIPY.

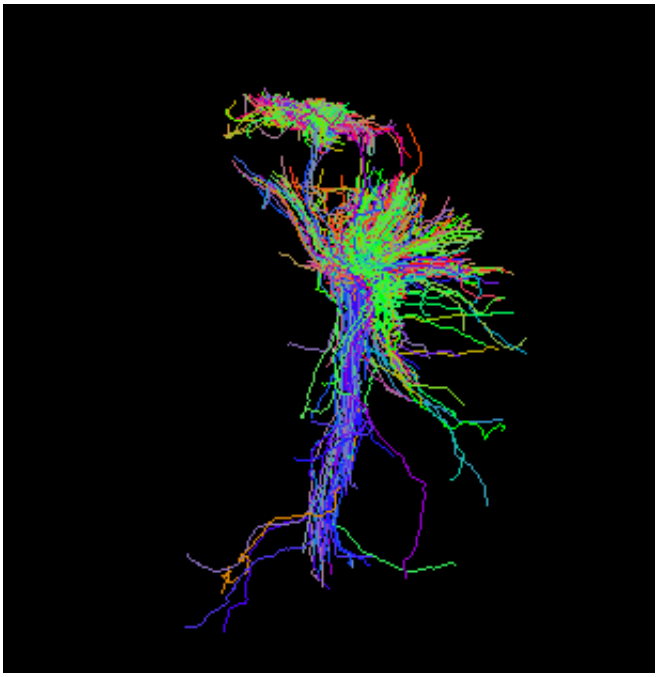

Fig. E.7 – Tract of corticospinal with DIPY.

Appendix F

Distribution of Anisotropic Microstructural Environments in Diffusion-Compartment Imaging (DIAMOND)

F.1 Model

In the DIAMOND model, different tissue compartments are defined, isotropic for the an extra-axonal compartment or anisotropic corresponding to a fiber population. In the case of this work, 3 compartments were defined: one for the extra-axonal restricted and two fiber population orientations .
The goal of this model is to describe, in each voxel, the tridimensional diffusion obtained from each tissue compartments. (The description of this model is based on the review Scherrer et al. [4])
In this model, the measurements are considered to be arising from the large number of 3D 'spin-packets'. Each homogeneous spin packet undergoes local anisotropic 3D diffusion represented by a diffusion tensor **D** (Fig.F.1a). The signal can be described by:

$$S_k = S_0 \int_D P(D) e^{-b_k g_k^T D g_k} dD \tag{F.1}$$

with :

- S_k, the obtained diffusion signal
- S_0, the signal without diffusion gradient
- $P(D)$, distribution matrix giving the spin packet fraction defined by a 3D diffusion tensor in a voxel

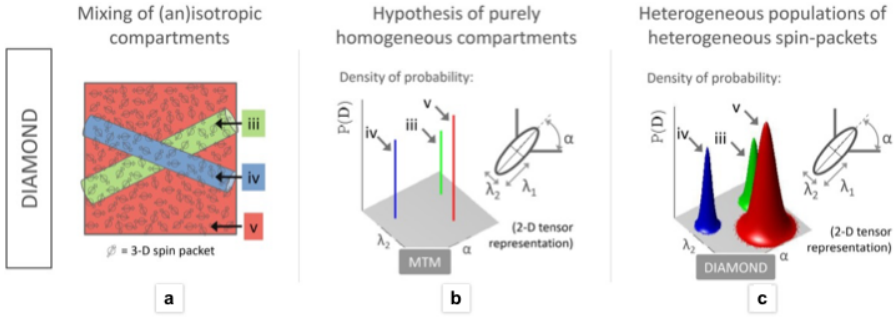

Fig. F.1 – Illustration of the microstructural environments in the DIAMOND model [4] (a) isotropic compartments (red) and anisotropic compartments (blue and green); (b) homogeneous compartments; (c) heterogeneous populations

If a voxel is considered as one homogeneous microstructural environment (i.e.,compartment) characterized by a diffusion tensor $\mathbf{D}^0$, then P(D) is a delta function such as: P(D) = δ(D - D^0). In this case, the model corresponds to a DTI model.
If it consists of several identifiable homogeneous microstructural environments, a mixture of delta functions would be used (Fig.F.1b).
In DIAMOND, a degree of heterogeneity is considered in each compartment, described by a population spin packets. Each microstructural environment is described with a peak-shaped matrix-variate Gamma (mv-Γ) distribution of spin packets (Fig.F.1c). The formal definition of the mv-Γ distribution is given by:

$$P_{\kappa,\Sigma}(D)\,\frac{|D|^{\kappa-(p+1)/2}}{|\Sigma|^{\kappa}\Gamma_p(\kappa)}e^{Tr(\Gamma^{-1}D)}$$

with :

- κ, the distribution shape parameter, the density becomes more concentrated around D_0 as κ increases. The more homogeneous the compartments, the higher the κ parameter;
- Σ, the scaling parameter;
- $\Gamma_p(\kappa) = \pi^{p(p-1)/4}\prod_{j=1}^{p}\Gamma\left(\kappa - \frac{j-1}{2}\right)$, the multi-variate gamma function.

Each voxel is modeled by a mathematical integration of each 3D packet contributions and each compartment is characterized by a statistical distribution of diffusivity.
A population with a narrow peak means that the population is homogeneous while a large peak represents a heterogeneous population. If N_p spin packets populations are considered and the composition of each population represented by a mv-Γ distribution written $P_{\kappa_j,\Sigma_j}(D)$, the voxel distribution is:

$$P(D) = \sum_{j=1}^{N_p} f_j P_{\kappa_j\Sigma_j}(D)$$

with:

- f_j, the occupation fraction and $\sum_{j=1}^{N_p} f_j = 1$

To summarise, the DIAMOND model is based on 3D spin packets modeled by the matrix-variate Gamma (mv-Γ) distribution. Compartments where the diffusion is either isotropic or anisotropic can be modeled thanks to the DIAMOND model. The existence of several compartments in a voxel is considered by taking into account the heterogeneities in each compartment. This model has limitations such as the fact that the number of spin packets (N_f) has to be known.

F.1.1 Metrics

Different maps are obtained with the DIAMOND model. In this work, the following metrics are considered:

- Free Water Diffusivity (FD), corresponding to the diffusivity in the extra-axonal restricted part;
- Model selection (Mose) map, a map with the number of fiber populations in each voxel;
- The fraction of each population within each voxel (Frac(Pi), i=0 and i=1 for the two anisotropic compartments and i=2 for the isotropic compartment);
- Fractional Anisotropy (FA), Axial Diffusivity (AD) and Radial Diffusivity (RD) are the same metrics than in the DTI model. As each of them does not make sense for the third population (corresponding to the extra-axonal population), the FA per voxel, called weighted FA (wFA), is normalized on the two anisotropic populations by:

  $$wFA = \frac{cFA(P0) \cdot Frac(P0) + cFA(P1) \cdot Frac(P1)}{Frac(P0) + Frac(P1)}$$

  cFA corresponds to the compartment FA. This formula is given for the wFA but similar calculations are done for the wAD and wRD.
- The heterogeneity of each population within each voxel (Hei(i)) . The heterogeneity metric Hei is linked to the concentration parameter κ by the formula :

  $$Hei = \frac{2}{\pi} \arctan\left(\frac{1}{\kappa}\right)$$

F.2 DIAMOND studies of Cerebral Palsy

No literature has been found on the model application on children with CP.

An introduction to DIAMOND applied on preterm infant brains was done by Eaton-Rosen et al, 2017 [47] : DIAMOND offers an explicit modelling of partial volume to deal with small brains and changing cortical convolution. The DIAMOND model offers improved sensitivity over the DTI model for the radiality index and fractional anisotropy.

Moreover, it is likely that the DIAMOND model is more accurate at accounting for the noise measurement than the tensor formulation, which is an advantage in the low signal-to-noise ratio (SNR) regime of the infant cortex [47].

This article motivates the application of the DIAMOND model to infants. However, due to the lack of literature, the following conclusions are hypothesis to be interpreted with caution.

F.3 Statistical analysis

Diffusion data of children with CP and control subjects were fitted with the DIAMOND model. The model estimation was run with Linux in C.
The mean and SD of each metric were computed on the cortico-spinal tract (CST) and statistical analyses were performed on these measurements. A visual comparison was done with boxplots and validated with t-tests (R command lines in Section 4.4.3).

The objective of this thesis is to investigate the microstructural brain changes in the CST, due to CP with bilateral lesions. The comparison between the control subjects and the children with CP were performed to highlight these changes.
Afterwards, the relation between the two hemispheres was analyzed. Even if the children with CP have bilateral lesions, one side of the body is more affected (see Table 4.1). The comparison of the two hemispheres was investigated to find the link between this functional asymmetry and the CST structure.
Since the AD, RD and FA parameters were computed by both DTI and the DIAMOND models, the metrics of these two models can be compared.
Finally, the behavioural surveys results were evaluated, to find a correlation between the DIAMOND metrics and the behavioural scores.

F.3.1 Comparison of the two populations

The first comparison was between the control subjects and the children with CP. In this section, first the mean and afterwards the standard deviation of the DIAMOND metrics were analyzed.

Mean

The first statistical parameter analyzed between the two populations and for all the DIAMOND metrics was the mean. The comparisons for both hemispheres for the free water diffusivity (FD) and the Mose metrics are shown in Fig.F.2; for the wFA, the wAD and the wRD metrics in Fig.F.3; for the fraction of the different compartments in Fig.F.4; and the heterogeneity of the compartment 0 and 1 in Fig.F.5.

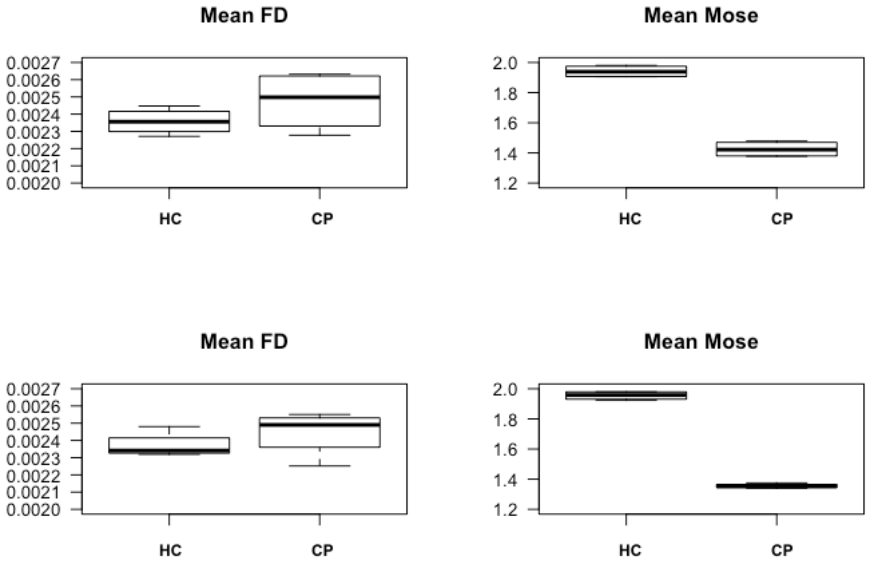

Fig. F.2 – Boxplots comparing the FD and the Mose metrics between healthy control subjects (HC) and children with CP (CP) for the dominant hemisphere (on the top) and non-dominant hemisphere (on the bottom).

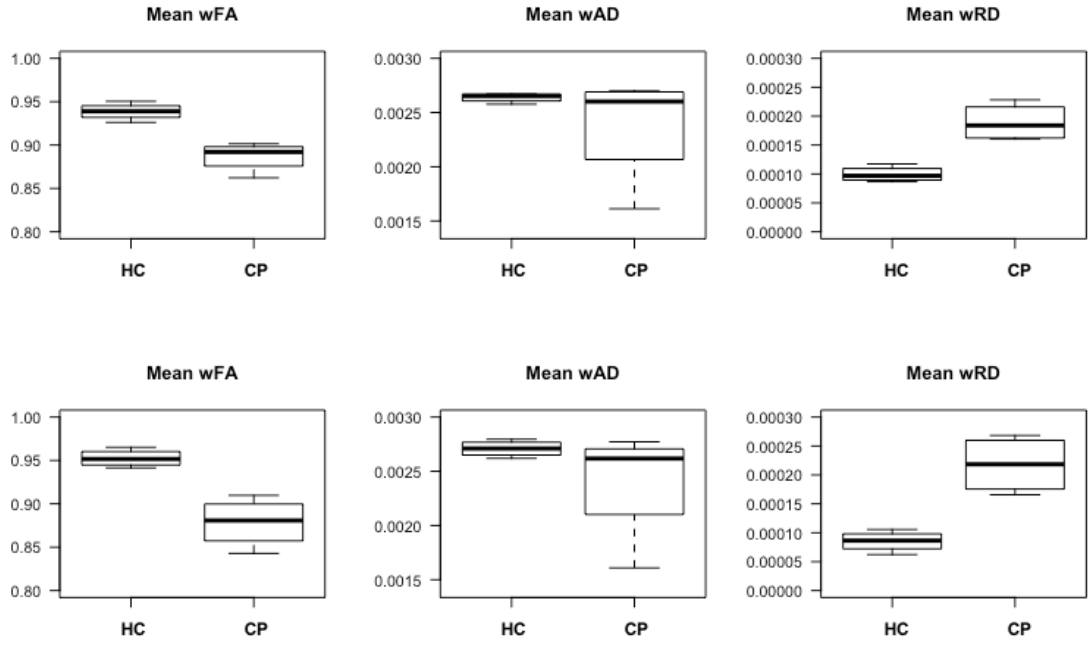

Fig. F.3 – Boxplots comparing the wFA, the wAD and the wRD metrics between healthy control subjects (HC) and children with CP (CP) for the dominant hemisphere (on the top) and non-dominant hemisphere (on the bottom).

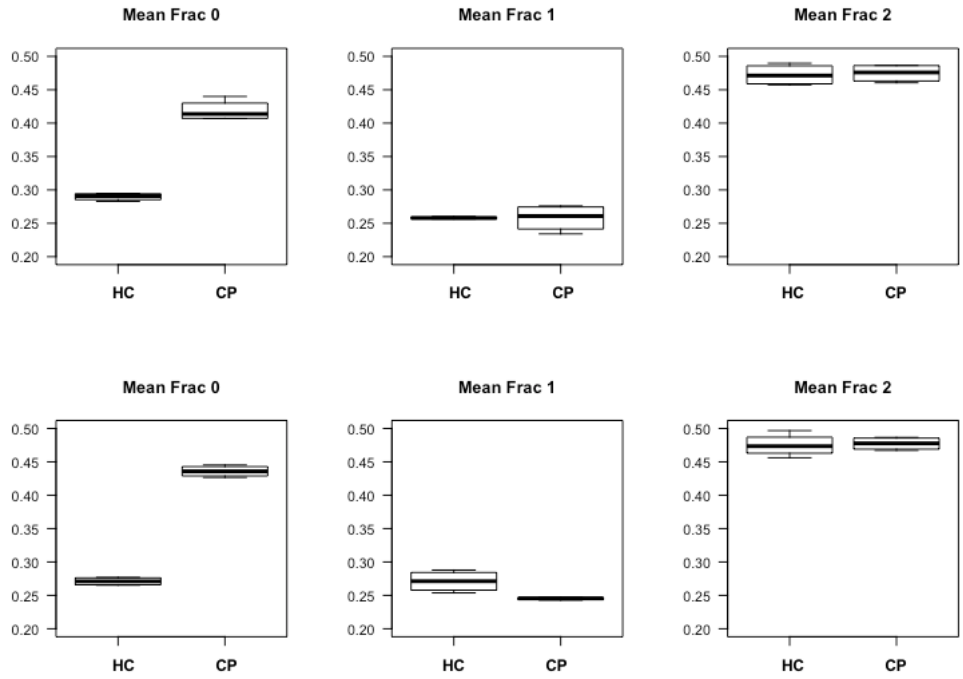

Fig. F.4 – Boxplots comparing the fraction of the different compartments between healthy control subjects (HC) and children with CP (CP) for the dominant hemisphere (on the top) and non-dominant hemisphere (on the bottom). 0 corresponding to the main fiber population, 1 to the second fiber population and 2 to the isotropic compartment.

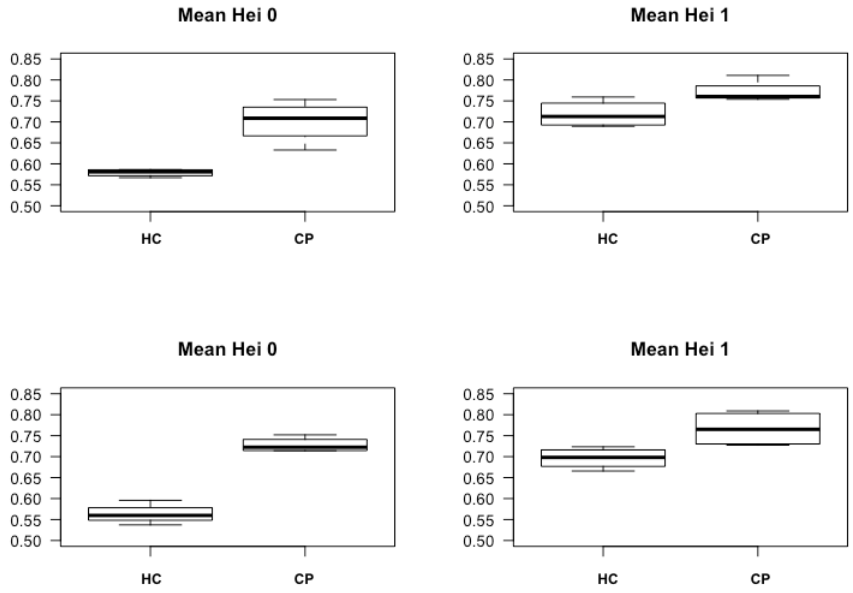

Fig. F.5 – Boxplots comparing the heterogeneity of the compartment 0 (the main fiber population) and 1 (the second fiber population) between healthy control subjects (HC) and children with CP (CP) for the dominant hemisphere (on the top) and non-dominant hemisphere (on the bottom).

Table F.1 – T-test results for the comparison of the mean of the different DIAMOND metrics between healthy control subjects (HC) and children with CP (CP), with the dominant (D) hemisphere on the top and the non-dominant (ND) hemisphere on the bottom. In green: the p-values inferior to 0.05 (significant level).

T-test Mean HC/CP D				
Mean_FD	t = -0.98568	df = 4.6896	p-value =	0.3724
Mean_Mose	t = 37.154	df = 4.4839	p-value =	9.35E-07
Mean_wFA	t = 4.9041	df = 3.7573	p-value =	0.009399
Mean_wAD	t = 1.1267	df = 3.1215	p-value =	0.339
Mean_wRD	t = -5.0002	df = 3.7788	p-value =	0.008681
Mean_frac_0	t = -31.539	df = 5.3992	p-value =	2.48E-07
Mean_hei_0	t = -10.951	df = 5.5065	p-value =	6.04E-05
Mean_frac_1	t = 3.2279	df = 3.0731	p-value =	0.04668
Mean_hei_1	t = -2.8502	df = 4.8814	p-value =	0.03681
Mean_frac_2	t = -0.23515	df = 4.7759	p-value =	0.8238

T-test Mean HC/CP ND				
Mean_FD	t = -1.255	df = 4.1031	p-value=	0.2762
Mean_Mose	t = 15.694	df = 5.5773	p-value =	7.91E-06
Mean_wFA	t = 5.1956	df = 4.8144	p-value =	0.003883
Mean_wAD	t = 0.99958	df = 3.0427	p-value =	0.390234304
Mean_wRD	t = -5.0708	df = 3.991	p-value =	0.007169
Mean_frac_0	t = -15.628	df = 3.7567	p-value =	0.000148448
Mean_hei_0	t = -4.7725	df = 3.1924	p-value =	0.01515
Mean_frac_1	t = 0.0096604	df = 3.043	p-value =	0.992955
Mean_hei_1	t = -2.5187	df = 5.7651	p-value =	0.0469664
Mean_frac_2	t = -0.22046	df = 5.8372	p-value =	0.8334755

The increase of Free Water Diffusivity in children with CP that can be observed in the boxplots (Fig.F.2) was not confirmed by the t-tests due to its high variance between the different subjects.

wFA and wRD have the same behavior than FA and RD in the DTI analysis: a lower value of the wFA and a higher value of wRD was observed in children with CP compared to control subjects. This is explained by the absence of the maturation process in the CST for both hemispheres compared to a normal development where the maturation continues to CST development during childhood [2].

The wAD mean computed by this model did not change between the children with CP and the control population. AD reportedly does not decrease during prolonged demyelination, in which axonal atrophy is evident [34]. As explained before, the AD modifications need to be interpreted with caution as no consensus has been found in the literature.

The major difference between DIAMOND and the other models is that the different compartments and their heterogeneity are taken into account. The model selection map (Mose map) corresponds to the number of population in each voxel. The visual result for a complete slice is shown in Fig.F.6. On the CP map, the voxels in the CST were mainly composed of one population (in gray) compared to the control map, where the majority of voxels have been modeled by two fiber populations (in black). This visual result was confirmed by the boxplots and the t-test.

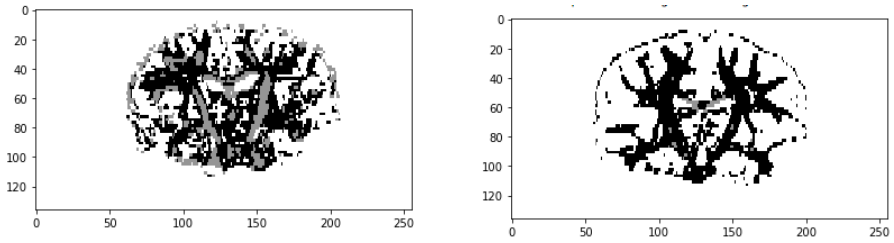

Fig. F.6 – Mose map for children with CP on the left and control population on the right. White: 0 population of fibers, Gray: 1 population of fibers and Black: 2 populations of fibers

An equivalent way to see that is with the fraction of each population (Frac(Pi)). The fraction of compartment 0, corresponding to the first anisotropic population was higher in the population with CP. The comparison of the fraction attributed to compartment 1 and 2 was not relevant due to the high variation between the subjects.

The last analyzed parameter is the heterogeneity, which was higher for the two anisotropic compartments in children with CP than in the control subjects.
In children with CP, a higher fraction of fiber population 1, a lower the fraction of fiber population 2 and a higher heterogeneity were observed. These parameters highlight the non-alignment of the CST fibers in children with CP.
Moreover, since the proportion of voxels modeled with a single fiber population is higher with CP patients, it is to be expected that the heterogeneity increases, as this single fiber population models all the orientation variations that are modeled with two fiber populations in the control patients.

Standard deviation

The second statistical parameter analyzed between the two populations and for all of the DIAMOND metrics is the Standard Deviation (SD). The comparison for both hemispheres for the FD and the Mose parameters is shown in Fig.F.7; for wFA, wAD and wRD in Fig.F.8; for the fraction of the different compartments in Fig.F.9; and the heterogeneity of the compartment 0 and 1 in Fig.F.10.

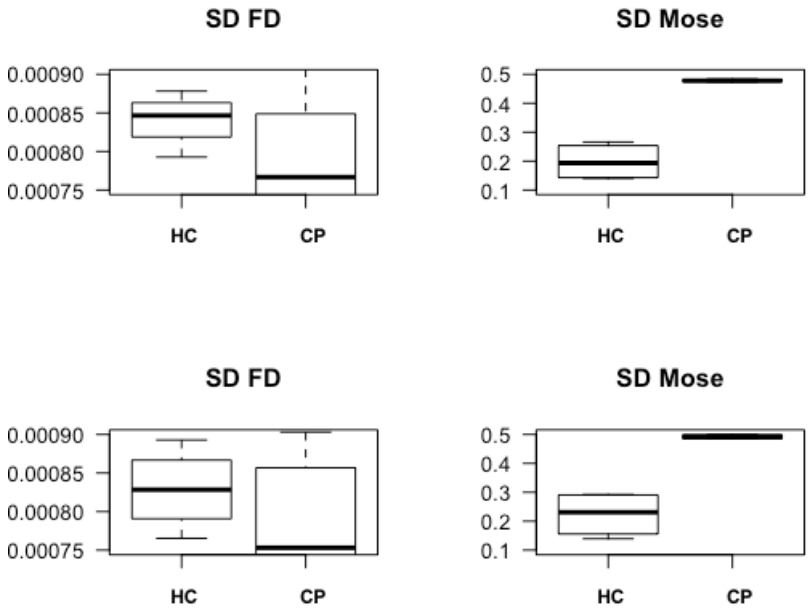

Fig. F.7 – Boxplots comparing the SD of the FD and the Mose metrics between healthy control subjects (HC) and children with CP (CP) for the dominant hemisphere (on the top) and non-dominant hemisphere (on the bottom).

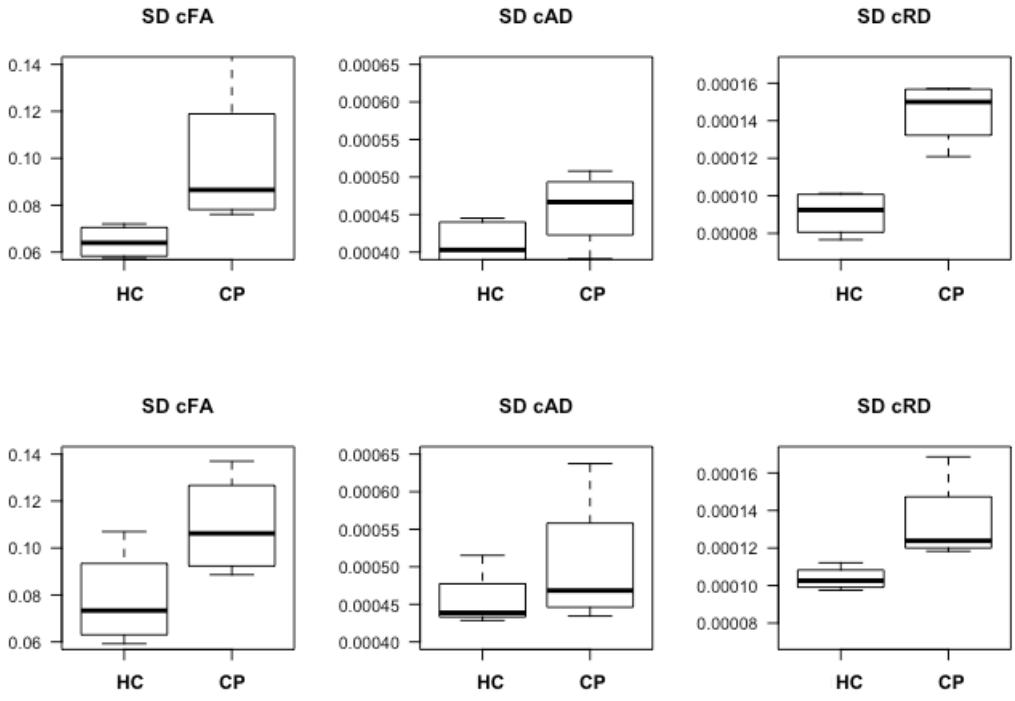

Fig. F.8 – Boxplots comparing the SD of the wFA, the wAD and the wRD metrics between healthy control subjects (HC) and children with CP (CP) for the dominant hemisphere (on the top) and non-dominant hemisphere (on the bottom).

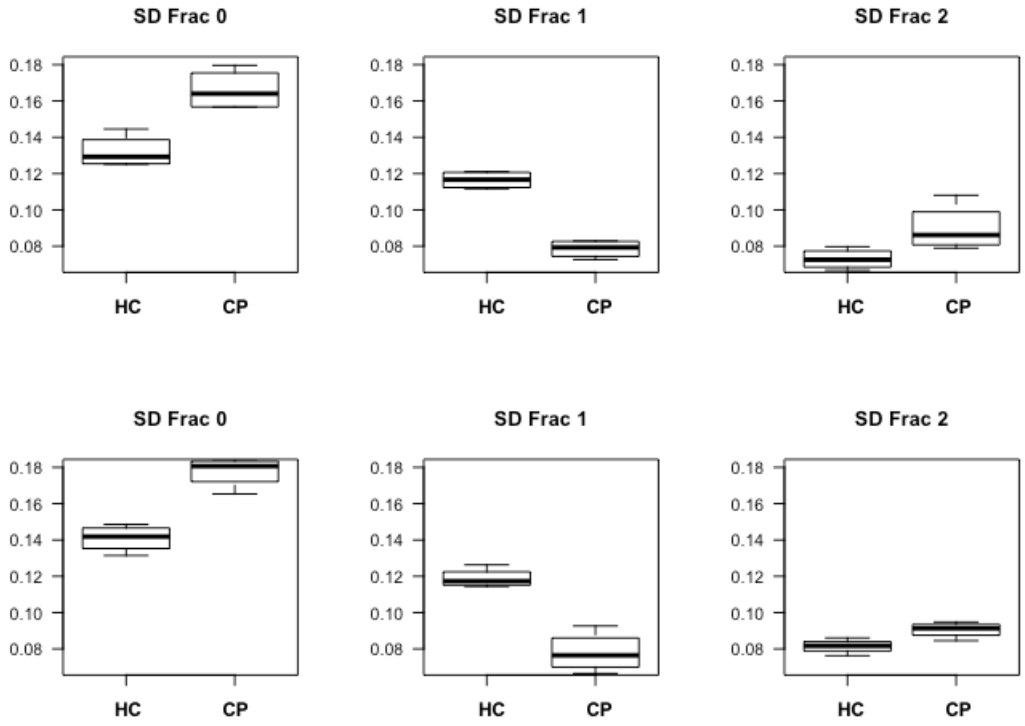

Fig. F.9 – Boxplots comparing the SD of the fraction of the different compartments between healthy control subjects (HC) and children with CP (CP) for the dominant hemisphere (on the top) and non-dominant hemisphere (on the bottom). 0 corresponding to the main fiber population, 1 to the second fiber population and 2 to the isotropic compartment.

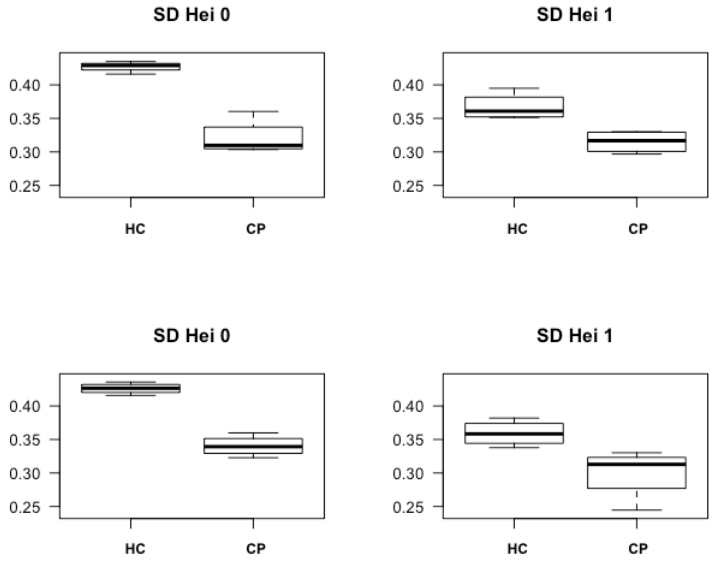

Fig. F.10 – Boxplots comparing the SD of the heterogeneity of the compartment 0 (the main fiber population) and 1 (the second fiber population) between healthy control subjects (HC) and children with CP (CP) for the dominant hemisphere (on the top) and non-dominant hemisphere (on the bottom).

Table F.2 – T-test results for the comparison of the Standard Deviation of the different DIAMOND metrics between control subjects and children with CP, with the dominant hemisphere on the top and the non-dominant hemisphere on the bottom. In green: the p-values inferior to 0.05 (significant level).

T-test SD CP/C D				
SD_FD	t = 1.0603	df = 4.2033	p-value =	0.3461
SD_Mose	t = -8.6102	df = 3.0269	p-value =	3.18E-03
SD_wFA	t = -2.0944	df = 3.3051	p-value =	0.1188
SD_wAD	t = -1.6778	df = 5.8935	p-value =	0.1453
SD_wRD	t = -5.1724	df = 5.4287	p-value =	0.00279
SD_frac_0	t = -4.699	df = 5.7171	p-value =	0.003779
SD_hei_0	t = 7.6355	df = 3.521	p-value =	0.002602
SD_frac_1	t = 10.904	df = 5.9968	p-value =	3.54E-05
SD_hei_1	t = 3.9479	df = 5.8199	p-value =	0.008032
SD_frac_2	t = -2.3911	df = 4.1091	p-value =	0.07337

T-test SD CP/C ND				
SD_FD	t = 1.0052	df = 4.2776	p-value =	0.3682
SD_Mose	t = -6.7613	df = 3.0602	p-value =	6.21E-03
SD_wFA	t = -2.0706	df = 5.9923	p-value =	0.08388
SD_wAD	t = -0.93259	df = 4.1092	p-value =	0.4025
SD_wRD	t = -2.4614	df = 3.4285	p-value =	0.08014
SD_frac_0	t = -6.4804	df = 5.8741	p-value =	6.98E-04
SD_hei_0	t = 9.7673	df = 4.5969	p-value =	3.02E-04
SD_frac_1	t = 6.6454	df = 4.2957	p-value =	0.002059
SD_hei_1	t = 2.771	df = 4.4227	p-value =	0.04497
SD_frac_2	t = -3.0675	df = 5.9591	p-value =	0.02221

Contrarily to the DTI and the NODDI models, in the DIAMOND model, some t-tests were relevant for the SD comparison in both hemispheres, the SD of Mose was higher in subjects with CP than in control patients. The SD of the fraction of compartment 0 was higher in children with CP and the SD of the fraction of compartment 1 was lower.
This is coherent with the comparison of the means. Indeed, in children with CP the fraction of compartment 0 was higher, the variation of this metric is by consequence more susceptible to change, and to have a higher SD. Reciprocally, in the control population, the fraction of compartment 1 was higher so the SD of fraction 1 was higher as well.
The SD of the heterogeneity of both populations was lower in the population with CP. The mean of the heterogeneity was higher is children with CP, with a low SD. This means that the heterogeneity is high and constant across all the CST.

F.3.2 Comparison between the two hemispheres

After comparing the two populations, the analysis of the two hemispheres was investigated. Even if children with CP have bilateral lesions, they have functional asymmetry. The aim of this section is to investigate if this asymmetry is present in the brain structure. The comparison for the control subjects and children with CP for FD and Mose is shown in Fig.F.11; for wFA, wAD and wRD in Fig.F.12; for the fraction of the different compartments in Fig.F.13; and the heterogeneity of the compartment 0 and 1 in Fig.F.14.

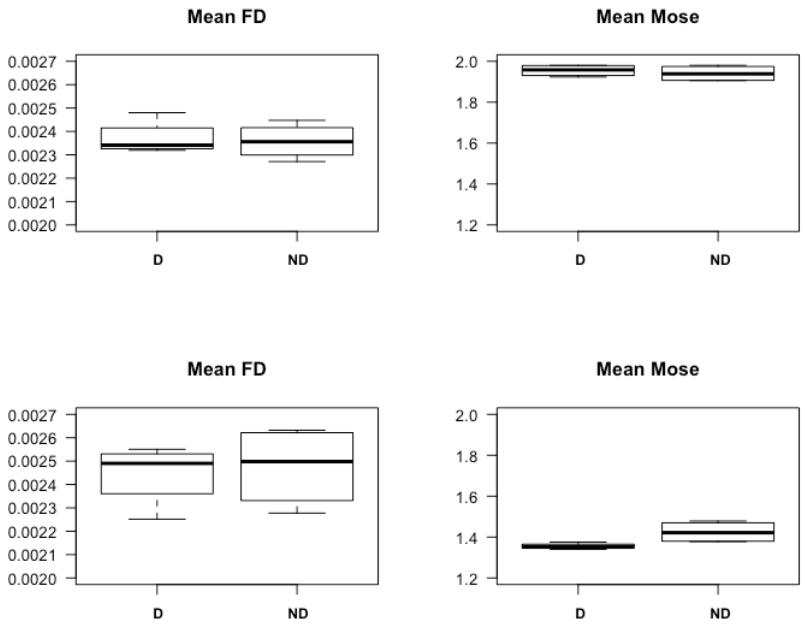

Fig. F.11 – Boxplots comparing two hemispheres of the FD and the Mose metrics for the control subjects (on the top) and the children with CP (on the bottom).

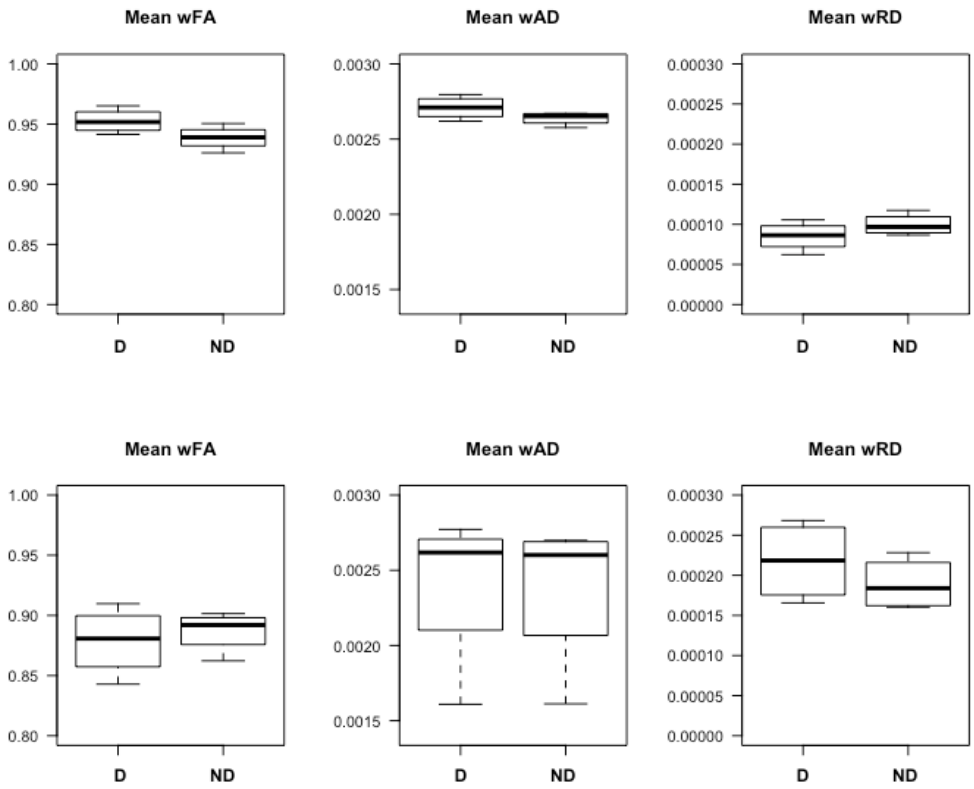

Fig. F.12 – Boxplots comparing two hemispheres of the wFA, the wAD and the wRD metrics for the control subjects (on the top) and the children with CP (on the bottom).

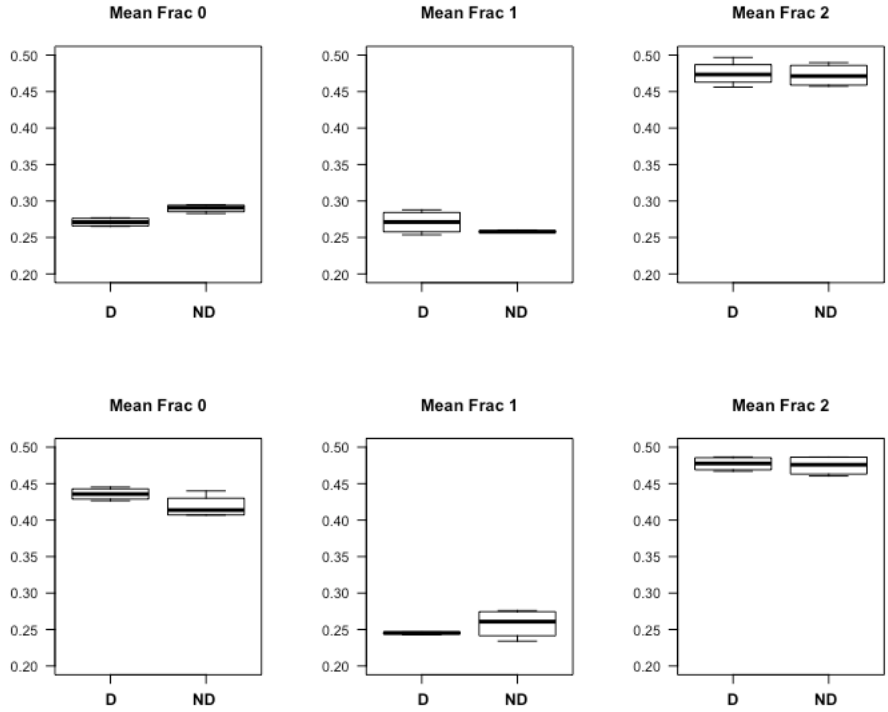

Fig. F.13 – Boxplots comparing two hemispheres for the fraction of the different compartments for the control subjects (on the top) and the children with CP (on the bottom). 0 corresponding to the main fiber population, 1 to the second fiber population and 2 to the isotropic compartment.

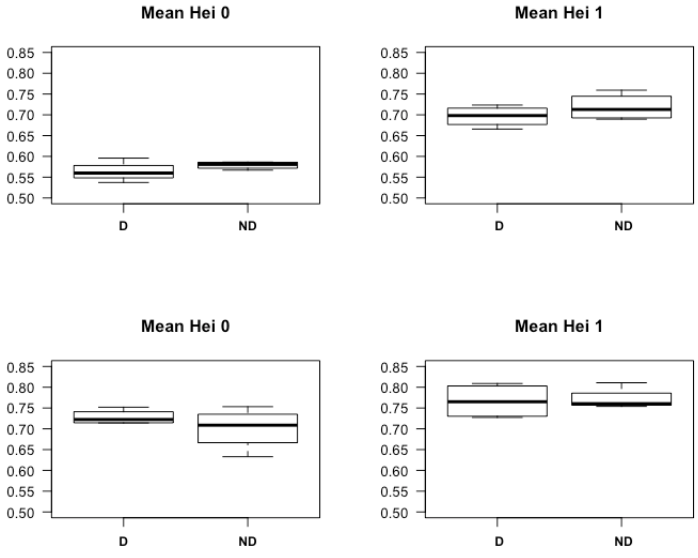

Fig. F.14 – Boxplots comparing two hemispheres for the heterogeneity of the compartment 0 (the main fiber population) and 1 (the second fiber population) for the control subjects (on the top) and the children with CP (on the bottom).

Table F.3 – T-test results for the comparison of the different DIAMOND metrics between dominant hemisphere and the non-dominant hemisphere, for the control (HC) population on the top and the population with CP (CP) on the bottom. In green: the p-values inferior to 0.05 (significant level).

T-test Mean D/ND HC				
Mean_FD	t = -0.42568	df = 3	p-value =	0.699
Mean_Mose	t = -2.1156	df = 3	p-value =	1.25E-01
Mean_wFA	t = -6.6662	df = 3	p-value =	0.006882
Mean_wAD	t = -2.7154	df = 3	p-value =	0.07283
Mean_wRD	t = 2.8596	df = 3	p-value =	0.0646
Mean_frac_0	t = 4.2638	df = 3	p-value =	0.02367
Mean_hei_0	t = 1.0708	df = 3	p-value =	0.3627
Mean_frac_1	t = -1.7761	df = 3	p-value =	1.74E-01
Mean_hei_1	t = 0.8383	df = 3	p-value =	0.4634
Mean_frac_2	t = -0.36176	df = 3	p-value =	0.7415

T-test Mean D/ND CP				
Mean_FD	t = 0.43021	df = 3	p-value =	0.6961
Mean_Mose	t = 2.2159	df = 3	p-value =	1.14E-01
Mean_wFA	t = 1.3102	df = 3	p-value =	0.2814
Mean_wAD	t = -0.90594	df = 3	p-value =	0.4318
Mean_wRD	t = -3.0071	df = 3	p-value =	0.05734
Mean_frac_0	t = -2.1754	df = 3	p-value =	1.18E-01
Mean_hei_0	t = -1.1191	df = 3	p-value =	3.45E-01
Mean_frac_1	t = 1.3726	df = 3	p-value =	0.2635
Mean_hei_1	t = 0.31995	df = 3	p-value =	0.77
Mean_frac_2	t = -0.93618	df = 3	p-value =	0.4182

As for the other models, the t-tests did not highlight any significant differences between the two hemispheres for the different metrics neither for the control subjects nor for the children with CP (see Table F.3).

F.3.3 Models comparison

The FA, SD and RD are estimated by the DTI and DIAMOND models. The estimation of these metrics by the two models were compared (Fig.F.15).

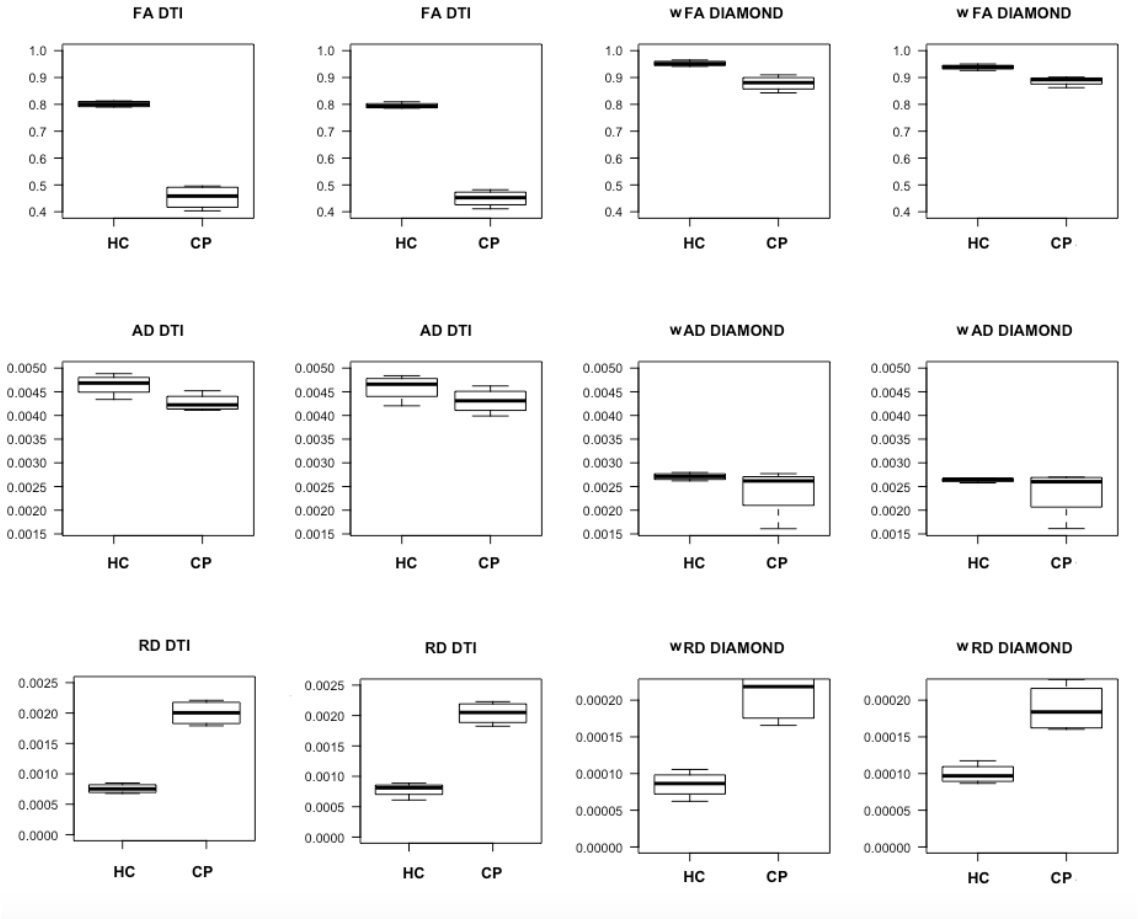

Fig. F.15 – Comparison between FA, AD and RD for DTI and DIAMOND models, for non dominant (column 1 and 3) and dominant (column 2 and 4) hemispheres, with both models on the same scale.

In DIAMOND, the wFA computed from the compartment-specific cFAs (see Section F.1.1 for the formula used) does not take into account the isotropic diffusion compartment but only the FA due to the two fiber populations. By consequence, it is logical that the values found were higher than those found with DTI. For example, considering a voxel filled only with two perpendicular fiber populations (Fig.F.16), the resulting FA found by DTI will be close to 0 (since both fiber populations "cancel" each other's anisotropy by being considered as a single population), whereas DIAMOND will output a FA close to 1 for both fiber populations.

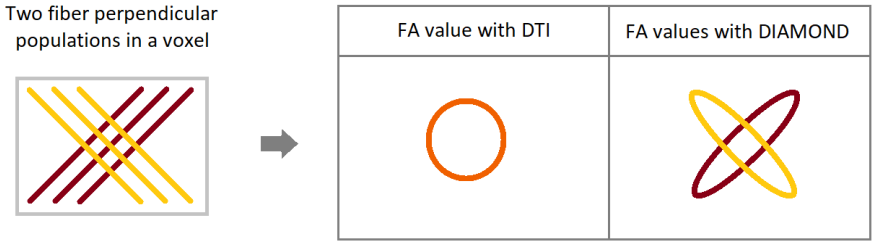

Fig. F.16 – Schematic representation of the FA estimation of a voxel filled with only two perpendicular fiber populations by DTI and DIAMOND. DTI: isotropic diffusion (represented by a sphere) and a FA close to 0. DIAMOND: anisotropic diffusion (represented by two ellipses) and a FA tending to 1.

For both models, the difference of AD was not significant. Comparing this value between the two models is by consequence not relevant.
For the RD, since there is more anisotropy considered by DIAMOND, there is less radial diffusivity. The opposite conclusion for FA can be therefore drawn.

F.3.4 Behavioural analysis

A correlation was calculated between each behavioural score (PEDI daily life and mobility, ACTILIM in logit and percent) and the mean of each DIAMOND metric for both dominant (D) and non-dominant (ND) hemispheres. The behavioural surveys were only asked to the parents of children with CP. By consequence, the following results only concern this population.

Since the number of children with CP is low (4 subjetcs), this analysis did not give any coherent and significant results is only given for information. The results are given for information in Table F.4.

Table F.4 – Table with the correlation values between behavioural scores and the DIAMOND metrics. PEDI_DA=PEDI-CAT for daily activities domain, PEDI_M=PEDI-CAT for mobility domain, AL_L= ACTIVLIM in [Logit] and AL_P= ACTIVLIM in [%]. In green: the correlation superior to 0.9; in red: the correlations inferior to -0.9.

Behaviour	PEDI_DA	PEDI_M	AL_L	AL_P
FD_D	-0,5930768	-0,9593203	0,2569482	-0,4470477
FD_ND	0,2628806	0,3587003	-0,5256319	-0,4779515
Mose_D	-0,5272538	-0,07501634	-0,7846641	0,7583355
Mose_ND	0,9796921	-0,4544248	-0,8826397	0,1826865
wFA_D	-0,3044933	-0,03034966	-0,5690246	-0,4658101
wFA_ND	0,9414448	0,8118169	-0,8575947	-0,6843213
wAD_D	0,3147016	0,3914059	-0,1772841	-0,1631328
wAD_ND	0,5613578	0,4931146	-0,4317119	-0,3449729
wRD_D	0,8662232	0,9327195	0,3406126	0,3477304
wRD_ND	-0,1326759	-0,2853849	0,2559374	0,4297196
Frac_0_D	-0,7048697	-0,5020835	-0,4116669	-0,9818231
Frac_0_ND	-0,05261491	0,7702062	0,005166984	-0,5896415
Hei_0_D	-0,9279194	-0,1808571	-0,8391393	-0,2662525
Hei_0_ND	0,6681192	-0,4613549	-0,6514726	0,5211347
Frac_1_D	-0,9560269	-0,7361319	-0,337107	-0,5747963
Frac_1_ND	0,3944276	0,07852191	-0,5526786	-0,08171727
Hei_1_D	0,5511919	0,8300625	0,2745103	0,09235229
Hei_1_ND	-0,8750166	-0,4929165	0,9604015	0,7059805
Frac_2_D	0,9006242	0,8353643	0,6766274	0,3975386
Frac_2_ND	-0,3576174	-0,09654622	0,3799105	0,1900398

Conclusion

In conclusion, the DIAMOND model highlights the same conclusion for the FA and RD than the DTI model. Moreover, it shows the non-parallel fiber structure in children with CP, with the heterogeneity and the fraction population parameters.

Appendix G

Technical notes on the use of the ExploreDTI software

- To be able to correct the motion by using ExploreDTI the sequence need to be normalized (norm=1) for all the b-vectors.
- ExploreDTI requires that the DTI without diffusion (b0) be at the beginning. This is the reason why the DTI and b-vector need to be sorted (can be done with a plugin of the software)
- After transforming the text and nifti files in matlab, the glyph objects need to be checked. In the case of this thesis, different modifications have to be applied to have a correct orientation of the glyph objects: permute gradient components: x y z and flip sign of gradient components: x y -z.
- In a way to improve the DTI maps, the DKI algorithm is used. To realize that, the b-value to NaN in the files transformation to matlab file. If the MD is not correct, the CSD tracking is impossible.
- For some data even with DKI, the MD was not correct. To solve this problem only one shell of the DTI acquisition was used.

Appendix H

Codes

H.1 Matlab code

Matlab code to select the needed information from ExploreDTI output the text files

```
%@author: Ysaline Leman
L1=load('/Users/ysaline/Desktop/result_stat/1_L.txt');
R1=load('/Users/ysaline/Desktop/result_stat/1_R.txt');
L2=load('/Users/ysaline/Desktop/result_stat/2_L.txt');
R2=load('/Users/ysaline/Desktop/result_stat/2_R.txt');
L3=load('/Users/ysaline/Desktop/result_stat/3_L.txt');
R3=load('/Users/ysaline/Desktop/result_stat/3_R.txt');
L5=load('/Users/ysaline/Desktop/result_stat/5_L.txt');
R5=load('/Users/ysaline/Desktop/result_stat/5_R.txt');
L21=load('/Users/ysaline/Desktop/result_stat/21_L.txt');
R21=load('/Users/ysaline/Desktop/result_stat/21_R.txt');
L27=load('/Users/ysaline/Desktop/result_stat/27_L.txt');
R27=load('/Users/ysaline/Desktop/result_stat/27_R.txt');
L34=load('/Users/ysaline/Desktop/result_stat/34_L.txt');
R34=load('/Users/ysaline/Desktop/result_stat/34_R.txt');
L38=load('/Users/ysaline/Desktop/result_stat/38_L.txt');
R38=load('/Users/ysaline/Desktop/result_stat/38_R.txt');

tab= zeros(8,20);

for i= 1:8
    sujet=[1 2 3 5 21 27 34 38];
    my_field_L = eval(strcat('L',num2str(sujet(i))));
    my_field_R = eval(strcat('R',num2str(sujet(i))));
    %left
    tab(i,1)= my_field_L(4,1);
    tab(i,2)= my_field_L(4,2);
    tab(i,3)= my_field_L(1,1);
    tab(i,4)= my_field_L(1,2);
    tab(i,5)= my_field_L(2,1);
```

```
    tab(i,6)= my_field_L(2,2);
    tab(i,7)= (my_field_L(6,1)*my_field_L(7,1))/2;
    tab(i,8)= (my_field_L(6,2)*my_field_L(7,2))/2;
    tab(i,9)= my_field_L(5,1);
    tab(i,10)= my_field_L(5,2);
   %right
    tab(i,11)= my_field_R(4,1);
    tab(i,12)= my_field_R(4,2);
    tab(i,13)= my_field_R(1,1);
    tab(i,14)= my_field_R(1,2);
    tab(i,15)= my_field_R(2,1);
    tab(i,16)= my_field_R(2,2);
    tab(i,17)= (my_field_R(6,1)*my_field_R(7,1))/2;
    tab(i,18)= (my_field_R(6,2)*my_field_R(7,2))/2;
    tab(i,19)= my_field_R(5,1);
    tab(i,20)= my_field_R(5,2);
end
```

H.2 Python codes

Python code used to calculate the NODDI metrics on the CST

```
#!/usr/bin/env python3
# -*- coding: utf-8 -*-
"""
@author: Ysaline Leman
"""
import os
import numpy as np
from dipy.io.image import load_nifti_data
os.chdir('/Users/ysaline/Desktop/NODDI/1_mvt.noddi')
iso=load_nifti_data('noddi_fiso.nii.gz')
icvf=load_nifti_data('noddi_ficvf.nii.gz')
odi=load_nifti_data('noddi_odi.nii.gz')

tract=load_nifti_data('Tract_mask_1_G.nii')
mask=tract.copy()
mask[mask>0]=1

iso_m=iso*mask
icvf_m=icvf*mask
odi_m=odi*mask

mean_iso = (np.mean(iso_m[iso_m>0]))
sd_iso=(np.std(iso_m[iso_m>0]))
mean_icvf = (np.mean(icvf_m[icvf_m>0]))
```

```
sd_icvf=(np.std(icvf_m[icvf_m>0]))
mean_odi = (np.mean(odi_m[odi_m>0]))
sd_odi=(np.std(odi_m[odi_m>0]))

NODDI=[mean_iso, sd_iso, mean_icvf, sd_icvf, mean_odi , sd_odi]
print(NODDI)
```

Python code used to calculate the DIAMOND metrics on the CST

```
# -*- coding: utf-8 -*-
"""
@author: Nicolas Delinte
"""

Patient='1_mvt_neuro'
Region='Tract_mask_31_G'
NewMetricMethod=2       # Possible values: 1 or 2

import os
import numpy as np
import matplotlib.pyplot as plt
from dipy.io.image import load_nifti, load_nifti_data

os.chdir('/Users/ysaline/Desktop/output_diam')

mask=load_nifti_data(Region+'.nii')
mask[mask>0]=1

dti=load_nifti_data(Patient+'_diamond_dti.nii')
frac=load_nifti_data(Patient+'_diamond_fractions.nii')
fd=load_nifti_data(Patient+'_diamond_freewater_diffusivity.nii')
hei=load_nifti_data(Patient+'_diamond_hei.nii')
kap=load_nifti_data(Patient+'_diamond_kappa.nii')
lkap=load_nifti_data(Patient+'_diamond_logKappa.nii')
mose=load_nifti_data(Patient+'_diamond_mosemap.nii')
t0=load_nifti_data(Patient+'_diamond_t0.nii')
t1=load_nifti_data(Patient+'_diamond_t1.nii')
t0_FA=load_nifti_data(Patient+'_diamond_t0_FA.nii')
t1_FA=load_nifti_data(Patient+'_diamond_t1_FA.nii')
t0_AD=load_nifti_data(Patient+'_diamond_t0_AD.nii')
t1_AD=load_nifti_data(Patient+'_diamond_t1_AD.nii')
t0_RD=load_nifti_data(Patient+'_diamond_t0_RD.nii')
t1_RD=load_nifti_data(Patient+'_diamond_t1_RD.nii')

if NewMetricMethod==1:      # mean over all 3 compartments
    cFA=t0_FA*frac[:,:,:,0,0]+t1_FA*frac[:,:,:,0,1]
    cAD=t0_AD*frac[:,:,:,0,0]+t1_AD*frac[:,:,:,0,1]
```

```
    cRD=t0_RD*frac[:,:,:,0,0]+t1_RD*frac[:,:,:,0,1]
else:                          # mean over the two fiber populations
    cFA=(t0_FA*frac[:,:,:,0,0]+t1_FA*frac[:,:,:,0,1])/(frac[:,:,:,0,0]+frac[:,:,:,0
    cAD=(t0_AD*frac[:,:,:,0,0]+t1_AD*frac[:,:,:,0,1])/(frac[:,:,:,0,0]+frac[:,:,:,0
    cRD=(t0_RD*frac[:,:,:,0,0]+t1_RD*frac[:,:,:,0,1])/(frac[:,:,:,0,0]+frac[:,:,:,0

# Sanity check -------------------------

plt.imshow(mose[:,:,40],cmap='Greys')
plt.imshow(np.repeat(np.rot90(mose[:,115,:],1),2, axis=0),cmap='Greys')

# Mean and std output ------------------

fd_m=fd*mask
mose_m=mose*mask
cFA_m=cFA*mask
cAD_m=cAD*mask
cRD_m=cRD*mask


print('DIAMOND')
print(np.mean(fd_m[fd_m>0]))
print(np.std(fd_m[fd_m>0]))
print(np.mean(mose_m[mose_m>0]))
print(np.std(mose_m[mose_m>0]))
print(np.mean(cFA_m[cFA_m>0]))
print(np.std(cFA_m[cFA_m>0]))
print(np.mean(cAD_m[cAD_m>0]))
print(np.std(cAD_m[cAD_m>0]))
print(np.mean(cRD_m[cRD_m>0]))
print(np.std(cRD_m[cRD_m>0]))

diamond=[np.mean(fd_m[fd_m>0]), np.std(fd_m[fd_m>0]), np.mean(mose_m[mose_m>0]), np
print(diamond)

for i in range(3):

    mosefiber=np.zeros(shape=mose.shape)
    if i==1:  #2 fibers per voxel zone
        mosefiber[mose>1]=1
    else:
        mosefiber[mose>=1]=1
    mosefiber=mosefiber*mask

    frac_m=frac[:,:,:,0,i]*mosefiber
    hei_m=hei[:,:,:,0,i]*mosefiber
```

```
kap_m=kap[:,:,:,0,i]*mosefiber
lkap_m=lkap[:,:,:,0,i]*mosefiber

print('Compartment:',i)
print(np.mean(frac_m[frac_m>0]))
print(np.std(frac_m[frac_m>0]))
print(np.mean(hei_m[hei_m>0]))
print(np.std(hei_m[hei_m>0]))
#print(np.mean(kap_m[kap_m>0]))
#print(np.std(kap_m[kap_m>0]))
#print(np.mean(lkap_m[lkap_m>0]))
#print(np.std(lkap_m[lkap_m>0]))
```

Appendix I

Sequences

Control sequence (167 directions)					CP sequence (133 directions)			
bvec-x	**bvec-y**	**bvec-z**	**b-val**		**bvec-x**	**bvec-y**	**bvec-z**	**b-val**
0.000000	0.000000	0.000000	1000		0.000000	0.000000	0.000000	1000
0.447214	0.000000	0.000000	1000		0.577350	0.000000	0.000000	1000
0.000894	0.447214	0.000000	1000		0.001155	0.577350	0.000000	1000
-0.011628	0.290242	0.339882	1000		-0.015011	0.374700	0.438786	1000
0.264303	-0.342566	0.112698	1000		0.341214	-0.442250	0.145492	1000
-0.105542	-0.234340	0.365821	1000		-0.136255	-0.302532	0.472273	1000
-0.399362	-0.115828	0.164575	1000		-0.515574	-0.149534	0.212465	1000
0.355982	0.057691	0.264303	1000		0.459571	0.074478	0.341214	1000
0.104648	0.415909	0.127009	1000		0.135100	0.536936	0.163967	1000
0.418592	0.062610	0.144897	1000		0.540400	0.080829	0.187061	1000
0.226290	-0.377895	-0.078262	1000		0.292139	-0.487861	-0.101036	1000
0.154736	-0.378790	-0.179780	1000		0.199763	-0.489016	-0.232095	1000
0.204377	-0.282192	-0.280403	1000		0.263849	-0.364308	-0.361999	1000
-0.217793	-0.173966	0.349721	1000		-0.281170	-0.224589	0.451488	1000
-0.276378	0.300975	0.182016	1000		-0.356802	0.388557	0.234982	1000
0.258042	-0.046957	-0.362243	1000		-0.333131	-0.060622	-0.467654	1000
-0.369846	-0.232998	0.095256	1000		-0.477469	-0.300799	0.122976	1000
0.399809	-0.017889	-0.199904	1000		0.516151	-0.023094	-0.258076	1000
0.129692	-0.241943	-0.352852	1000		0.167432	-0.312346	-0.455529	1000
0.051877	-0.430667	-0.109567	1000		0.066973	-0.555988	-0.141451	1000
-0.357771	0.180227	-0.198563	1000		-0.461880	0.232672	-0.256344	1000
0.229868	0.375659	0.077815	1000		0.296758	0.484974	0.100459	1000
-0.352852	0.068424	-0.266539	1000		-0.455529	0.088335	-0.344101	1000
0.424406	-0.104201	0.094362	1000		0.547905	-0.134523	0.121821	1000
0.104201	0.350168	0.258042	1000		0.134523	0.452065	0.333131	1000
0.009391	-0.084076	-0.439164	1000		-0.012124	-0.108542	-0.566958	1000
0.097045	-0.427536	0.088996	1000		0.125285	-0.551947	0.114893	1000
0.346143	-0.270117	0.084971	1000		0.446869	-0.348720	0.109697	1000
-0.072001	0.159208	0.411884	1000		-0.092953	0.205537	0.531740	1000
-0.065740	0.326913	-0.297844	1000		-0.084870	0.422043	-0.384515	1000

0.397126	0.186488	0.086312	1000		0.512687	0.240755	0.111429	1000
-0.251334	0.103754	-0.355088	1000		-0.324471	0.133945	-0.458416	1000
-0.170388	0.063952	0.408753	1000		-0.219970	0.082561	0.527698	1000
0.136847	-0.088996	-0.416356	1000		-0.176669	-0.114893	-0.537513	1000
-0.148475	-0.058138	0.417697	1000		-0.191680	-0.075056	0.539245	1000
-0.430667	-0.118512	0.019677	1000		-0.555988	-0.152998	0.025403	1000
-0.428878	0.091679	0.086312	1000		-0.553679	0.118357	0.111429	1000
0.202588	-0.397573	0.030411	1000		0.261540	-0.513264	0.039260	1000
-0.345696	0.280850	0.039355	1000		-0.446292	0.362576	0.050807	1000
0.317074	0.182463	0.257148	1000		0.409341	0.235559	0.331976	1000
-0.309919	0.010733	0.322441	1000		-0.400104	0.013856	0.416270	1000
0.305000	0.236576	-0.226290	1000		0.393753	0.305418	-0.292139	1000
-0.063504	-0.324230	0.301422	1000		-0.081984	-0.418579	0.389134	1000
-0.330938	0.173519	0.245520	1000		-0.427239	0.224012	0.316965	1000
-0.046063	0.367610	0.250440	1000		-0.059467	0.474582	0.323316	1000
0.261173	-0.266539	0.246415	1000		0.337173	-0.344101	0.318120	1000
-0.039355	-0.149817	0.419486	1000		-0.050807	-0.193412	0.541555	1000
-0.246862	-0.354193	0.115828	1000		-0.318697	-0.457261	0.149534	1000
0.374765	-0.204824	-0.132375	1000		0.483820	-0.264426	-0.170896	1000
0.162339	-0.250887	0.332727	1000		0.209578	-0.323894	0.429549	1000
-0.082287	0.175308	-0.402939	1000		-0.106232	0.226321	-0.520193	1000
-0.322441	-0.309919	0.004025	1000		-0.416270	-0.400104	0.005196	1000
0.193643	0.305000	-0.263409	1000		0.249993	0.393753	-0.340059	1000
0.224501	0.308577	0.232998	1000		0.289830	0.398372	0.300799	1000
0.076474	-0.227632	-0.377448	1000		-0.098727	-0.293871	-0.487284	1000
0.207060	0.189171	0.348379	1000		0.267313	0.244219	0.449756	1000
0.172177	-0.361796	0.198563	1000		0.222280	-0.467076	0.256344	1000
-0.318863	-0.110462	0.293372	1000		-0.411651	-0.142606	0.378742	1000
0.116276	0.395784	-0.173072	1000		0.150111	0.510955	-0.223435	1000
0.000447	0.034435	-0.445872	1000		0.000577	0.044456	-0.575618	1000
0.016547	-0.403387	0.192302	1000		0.021362	-0.520770	0.248261	1000
0.254912	-0.135506	-0.341224	1000		0.329090	-0.174937	-0.440518	1000
-0.126114	0.064846	-0.423958	1000		-0.162813	0.083716	-0.547328	1000
0.322441	0.271906	0.148475	1000		0.416270	0.351029	0.191680	1000
0.119406	0.429325	-0.038013	1000		0.154153	0.554256	-0.049075	1000
0.000000	0.000000	0.000000	0		0.000000	0.000000	0.000000	0
0.632456	0.000000	0.000000	2000		0.816497	0.000000	0.000000	2000
0.312433	0.549604	0.000000	2000		0.403349	0.709536	0.000000	2000
-0.075895	0.405404	0.479401	2000		-0.097980	0.523374	0.618904	2000
0.581227	-0.209343	-0.135345	2000		0.750360	-0.270260	-0.174730	2000
-0.070835	-0.399079	0.485726	2000		-0.091448	-0.515209	0.627069	2000
-0.578064	-0.149260	0.208078	2000		-0.746278	-0.192693	0.268627	2000
0.430702	0.191634	0.421848	2000		0.556034	0.247398	0.544603	2000
0.042375	0.631191	-0.008222	2000		0.054705	0.814864	-0.010614	2000

0.580594	0.096766	0.232111	2000		0.749544	0.124924	0.299654	2000
0.280178	-0.562885	0.065143	2000		0.361708	-0.726682	0.084099	2000
0.136610	-0.586286	-0.194164	2000		0.176363	-0.756892	-0.250664	2000
0.303579	-0.424378	-0.357337	2000		0.391918	-0.547869	-0.461321	2000
-0.347851	-0.302314	0.433232	2000		-0.449073	-0.390285	0.559300	2000
-0.443351	0.438292	0.108150	2000		-0.572364	0.565832	0.139621	2000
0.271323	-0.004427	-0.571107	2000		-0.350277	-0.005715	-0.737296	2000
-0.442086	-0.404772	0.202386	2000		-0.570731	-0.522558	0.261279	2000
0.000000	0.000000	0.000000	0		0.000000	0.000000	0.000000	0
0.459163	0.057553	-0.431335	2000		0.592777	0.074301	-0.556851	2000
0.246658	-0.157481	-0.560988	2000		0.318434	-0.203308	-0.724232	2000
0.108782	-0.557193	-0.278280	2000		-0.140437	-0.719333	-0.359258	2000
-0.385798	0.405404	-0.295357	2000		-0.498063	0.523374	-0.381304	2000
0.378841	0.435762	0.258674	2000		0.489081	0.562566	0.333947	2000
-0.460428	0.140405	-0.410464	2000		-0.594410	0.181262	-0.529906	2000
0.558458	-0.251717	0.157481	2000		0.720966	-0.324966	0.203308	2000
0.202386	0.346586	0.488256	2000		0.261279	0.447440	0.630335	2000
0.027828	-0.169498	-0.608422	2000		-0.035926	-0.218821	-0.785470	2000
0.119534	-0.554664	0.280178	2000		0.154318	-0.716068	0.361708	2000
0.462957	-0.210608	-0.375679	2000		0.597675	-0.271893	-0.484999	2000
0.195429	-0.347851	0.490785	2000		0.252297	-0.449073	0.633601	2000
0.180882	0.542647	-0.270059	2000		0.233518	0.700554	-0.348644	2000
0.543279	0.318758	0.055656	2000		0.701371	0.411514	0.071852	2000
-0.067673	0.135978	-0.614114	2000		-0.087365	0.175547	-0.792818	2000
-0.188472	-0.112577	0.593243	2000		-0.243316	-0.145336	0.765874	2000
0.000000	0.000000	0.000000	0		0.000000	0.000000	0.000000	0
0.774597	0.000000	0.000000	3000		1.000000	0.000000	0.000000	3000
0.382651	0.673125	0.000000	3000		0.494000	0.869000	0.000000	3000
-0.092952	0.496516	0.587144	3000		-0.120000	0.641000	0.758000	3000
0.711854	-0.256391	-0.165764	3000		0.919000	-0.331000	-0.214000	3000
-0.086755	-0.488770	0.594890	3000		-0.112000	-0.631000	0.768000	3000
-0.707981	-0.182805	0.254842	3000		-0.914000	-0.236000	0.329000	3000
0.527500	0.234703	0.516656	3000		0.681000	0.303000	0.667000	3000
0.051898	0.773047	-0.010070	3000		0.067000	0.998000	-0.013000	3000
0.711080	0.118513	0.284277	3000		0.918000	0.153000	0.367000	3000
0.343146	-0.689391	0.079783	3000		0.443000	-0.890000	0.103000	3000
0.167313	-0.718051	-0.237801	3000		0.216000	-0.927000	-0.307000	3000
0.371806	-0.519754	-0.437647	3000		0.480000	-0.671000	-0.565000	3000
-0.426028	-0.370257	0.530599	3000		-0.550000	-0.478000	0.685000	3000
-0.542992	0.536795	0.132456	3000		-0.701000	0.693000	0.171000	3000
0.332302	-0.005422	-0.699461	3000		-0.429000	-0.007000	-0.903000	3000
-0.541443	-0.495742	0.247871	3000		-0.699000	-0.640000	0.320000	3000
0.000000	0.000000	0.000000	0		0.000000	0.000000	0.000000	0
0.562357	0.070488	-0.528275	3000		0.726000	0.091000	-0.682000	3000

0.302093	-0.192875	-0.687067	3000		0.390000	-0.249000	-0.887000	3000
0.133231	-0.682420	-0.340823	3000		-0.172000	-0.881000	-0.440000	3000
-0.472504	0.496516	-0.361737	3000		-0.610000	0.641000	-0.467000	3000
0.463983	0.533697	0.316810	3000		0.599000	0.689000	0.409000	3000
-0.563906	0.171960	-0.502713	3000		-0.728000	0.222000	-0.649000	3000
0.683969	-0.308289	0.192875	3000		0.883000	-0.398000	0.249000	3000
0.247871	0.424479	0.597989	3000		0.320000	0.548000	0.772000	3000
0.034082	-0.207592	-0.745162	3000		-0.044000	-0.268000	-0.962000	3000
0.146399	-0.679321	0.343146	3000		0.189000	-0.877000	0.443000	3000
0.567005	-0.257941	-0.460110	3000		0.732000	-0.333000	-0.594000	3000
0.239350	-0.426028	0.601087	3000		0.309000	-0.550000	0.776000	3000
0.221535	0.664604	-0.330753	3000		0.286000	0.858000	-0.427000	3000
0.665379	0.390397	0.068165	3000		0.859000	0.504000	0.088000	3000
-0.082882	0.166538	-0.752133	3000		-0.107000	0.215000	-0.971000	3000
-0.230830	-0.137878	0.726572	3000		-0.298000	-0.178000	0.938000	3000
0.000000	0.000000	0.000000	0					
1.000000	0.000000	0.000000	5000					
0.494000	0.869000	0.000000	5000					
-0.120000	0.641000	0.758000	5000					
0.919000	-0.331000	-0.214000	5000					
-0.112000	-0.631000	0.768000	5000					
-0.914000	-0.236000	0.329000	5000					
0.681000	0.303000	0.667000	5000					
0.067000	0.998000	-0.013000	5000					
0.918000	0.153000	0.367000	5000					
0.443000	-0.890000	0.103000	5000					
0.216000	-0.927000	-0.307000	5000					
0.480000	-0.671000	-0.565000	5000					
-0.550000	-0.478000	0.685000	5000					
-0.701000	0.693000	0.171000	5000					
0.429000	-0.007000	-0.903000	5000					
-0.699000	-0.640000	0.320000	5000					
0.000000	0.000000	0.000000	0					
0.726000	0.091000	-0.682000	5000					
0.390000	-0.249000	-0.887000	5000					
0.172000	-0.881000	-0.440000	5000					
-0.610000	0.641000	-0.467000	5000					
0.599000	0.689000	0.409000	5000					
-0.728000	0.222000	-0.649000	5000					
0.883000	-0.398000	0.249000	5000					
0.320000	0.548000	0.772000	5000					
0.044000	-0.268000	-0.962000	5000					
0.189000	-0.877000	0.443000	5000					
0.732000	-0.333000	-0.594000	5000					

0.309000	-0.550000	0.776000	5000					
0.286000	0.858000	-0.427000	5000					
0.859000	0.504000	0.088000	5000					
-0.107000	0.215000	-0.971000	5000					
-0.298000	-0.178000	0.938000	5000					

Table I.1 – Acquisition sequences(3 b-vectors in x, y and z directions and 1 column of b-values) for the control subjects on the left, and the children with CP on the right. The red color allows to highlight the normalization.

UNIVERSITÉ CATHOLIQUE DE LOUVAIN
École polytechnique de Louvain
Rue Archimède, 1 bte L6.11.01, 1348 Louvain-la-Neuve, Belgique | **www.uclouvain.be/epl**